Towards a Cenozoic History of Atmospheric CO_2

The Cenozoic CO_2 Proxy Integration Project ($CenCO_2PIP$) Consortium

Abstract: The geological record encodes the relationship between climate and atmospheric carbon dioxide (CO_2) over long and short timescales, as well as potential drivers of evolutionary transitions. However, reconstructing CO_2 beyond direct measurements requires the use of paleo-proxies and herein lies the challenge, as proxies differ in their assumptions, degree of understanding, and even reconstructed values. Here we critically evaluate, categorize, and integrate available proxies to create a high-fidelity and transparently constructed atmospheric CO_2 record spanning the past 66 million years. This provides clearer evidence for higher Earth System Sensitivity in the past and for the role of CO_2 thresholds in biological and cryosphere evolution.

The contribution of atmospheric CO_2 to Earth's greenhouse effect and the potential for variations in the global carbon cycle to cause climate change has been known for more than a century (*1*), but it was only in 1958 that direct measurements of the concentration of CO_2 in the atmosphere (or molar mixing ratio - the mole fraction of a gas in one mole of air) were systematically collected. Alongside reconstructions of the historical rise in Earth's surface temperature (*2*), this record has become one of the most influential and scientifically valuable environmental time-series, documenting the continuous rise in annual mean CO_2 from 315 parts per million (ppm) in 1958 to 419 ppm in 2022 (*3*). Projecting beyond these records to estimate how Earth's climate will respond to further increases in CO_2 requires global climate models (*4*). However, while successful in explaining observed historical climate change (*2*), models leave doubt as to whether global mean temperature will rise linearly as a function of future doubling of CO_2 (i.e., an invariant 'climate sensitivity') or whether climate feedbacks will lead to an increasing (or 'state-dependent') sensitivity of climate to CO_2 in the future (*5, 6*).

We can turn to the geological record to help constrain models and improve our understanding of non-linearities in the climate system (e.g., *7*), as it documents a variety of global climate changes and critically, climate states warmer than today. Leveraging this record, however, requires the paired quantification of both past atmospheric CO_2 and temperature. In parallel with recent efforts to compile and vet paleo-temperature estimates (*8*), here we focus on paleo-CO_2 estimates. Samples of ancient air can be extracted and analyzed from bubbles preserved in ancient polar ice (*9, 10*), but continuous ice core records currently only extend our knowledge of CO_2 back about 800 thousand years (kyr) (for a compilation, see *11*), with isolated time slices extending to ~2 Ma (million years ago) (*12, 13*). Importantly, at no point during the Pleistocene (2.58 Ma to 11,700 years ago) did CO_2 come close to present-day values (419 ppm, year 2022), with 300 ppm being the highest value measured to date (*14*). In contrast, depending on the extent of future human emissions, atmospheric CO_2 could reach 600–1000 ppm by the year 2100 (*2*). Feedbacks between changing climate and the carbon cycle may also amplify or diminish emissions from surficial carbon reservoirs (e.g., thawing permafrost, adjustments in size and composition of the terrestrial biosphere and marine carbon pool), creating additional uncertainty in future CO_2 projections (*15, 16*). Past changes in CO_2 inherently include the role of these feedbacks, and their study could help reduce uncertainty in Earth system models (*17*).

A solid understanding of atmospheric CO_2 variation through geological time is also essential to deciphering and learning from other features of Earth's history. Changes in atmospheric CO_2 and climate are suspected to have caused mass extinctions (e.g., *18, 19*) as well as evolutionary innovations (*20, 21*). During the Cenozoic, long-term declines in CO_2 and associated climate cooling have been proposed as the drivers of changing plant physiology (e.g., carbon-concentrating mechanisms), species competition and dominance, and associated with this, mammalian evolution. A more refined understanding of past trends in CO_2 is therefore central to understanding how modern species and ecosystems arose and may fare in the future.

Extending the CO_2 record beyond the temporally restricted availability of polar ice requires the use of 'proxies'. In essence, a CO_2 proxy could be any biological and/or geochemical property of a fossil or mineral that responds to the concentration of ambient CO_2 when it is formed. Unfortunately, unlike in the case of bubbles of ancient air trapped in polar ice, this response is invariably indirect. The connection between a proxy signal and atmospheric CO_2 is

often strongly mediated via biological 'vital effects' (e.g., concentration of or discrimination against certain molecules, elements or isotopes due to physiological processes such as biomineralization, photosynthesis, respiration), may be indirectly connected to the atmosphere via dissolution of carbon in seawater or lakes, may involve isotopic or other chemical fractionation steps, or a combination of these. When preserved in terrestrial or marine sediments, proxy substrates can also be impacted by post-depositional ('diagenetic') processes that must be accounted for. Relationships between proxies and CO_2 are typically calibrated using observations or laboratory experiments; in biological systems, these calibrations are often limited to modern systems (e.g., modern organisms or soils), and applications to the distant past focus on physiologically or physically similar systems preserved in the sediment and rock record (e.g., similar fossil organisms or fossil soils). Most CO_2 proxies also require estimation of one or more additional environmental parameters and hence depend on additional proxy records. The complexity of proxy-enabled paleoclimate reconstructions thus presents a major challenge for creating a self-consistent estimate of atmospheric CO_2 through geological time and requires careful validation.

One of the first paleo-CO_2 proxies to be devised was based on the observation that vascular plants typically optimize the density, size, and opening/closing behavior of stomatal pores on their leaf surfaces to ensure sufficient CO_2 uptake while minimizing water loss (e.g., *22*). A count of stomatal frequencies then provides a simple proxy for the CO_2 concentration experienced by the plant (*23*). Changes in ambient CO_2 can also drive a cascade of interrelated effects on photosynthesis, the flux of CO_2 into the leaf (largely determined by stomatal size and density), and the carbon isotopic fractionation during photosynthesis ($\Delta^{13}C$, *22, 23, 24*). While lacking functional stomata, non-vascular plants like liverworts also exhibit isotopic fractionation during photosynthesis, and their $\delta^{13}C$ values are thus similarly controlled by ambient CO_2. The list of terrestrial paleo-CO_2 proxies also includes inorganic carbonate nodules precipitated in ancient soils (i.e., paleosols) as well as sodium carbonate minerals precipitated in continental lacustrine evaporites. While the paleosol proxy uses the carbon isotope composition of carbonate nodules and deconvolves the mixture of atmospheric and soil-respired CO_2 in soil porewaters using models of soil CO_2 (*25, 26*), the nahcolite proxy is based on the CO_2 dependence of sodium carbonate mineral equilibria (*27, 28*). Analogous to non-vascular plants on land, phytoplankton fractionate carbon isotopes during photosynthesis in response to the concentration of dissolved CO_2 in seawater, creating an isotopic signal stored in organic biomolecules that can be retrieved from ocean sediments (*29*). Boron proxies recorded in fossil shells of marine calcifying organisms are related to seawater pH, which in turn can be related back to atmospheric CO_2 (*30, 31*). A detailed discussion of the analytical details, entrained assumptions, and inherent uncertainties of currently available CO_2 proxies, plus summaries of recent advances and opportunities for further validation, is presented in the Supplemental Material and in Table S1.

Although each of these proxies has been validated extensively, comparing reconstructions from different proxies often reveals discrepancies. Prior compilations of paleo-CO_2 and explorations of the CO_2-climate linkage already exist (*32-34*), however, those studies applied limited proxy vetting, include CO_2 estimates that predate major innovations in some methods, and use rather basic data interpolation to assess broad CO_2 trends. Earlier CO_2 reconstructions are also often insufficiently constrained by ancillary data (e.g., concomitant

100 temperature, isotopic composition of seawater or atmosphere) to be consistent with modern
101 proxy theory, have incomplete or missing uncertainty estimates for CO_2 and/or sample age, and
102 may exhibit fundamental disagreement with other proxies, leaving our current understanding of
103 past CO_2 incomplete.

104 In this study we present the results of a 7-year endeavor by an international consortium
105 of researchers whose collective expertise spans the reconstruction of paleo-CO_2 from all available
106 terrestrial and marine archives. We have jointly created a detailed, open-source database of
107 published paleo-CO_2 estimates including all raw and ancillary data together with associated
108 analytical and computational methods. Each record was vetted and categorized in view of the
109 most recent proxy understanding, with calculations adopting a common methodology including
110 full propagation of uncertainties. We focus our efforts here on the Cenozoic, when the spatial
111 distribution of continents and ocean basins, as well as the structure of marine and terrestrial
112 ecosystems, was similar to the modern, yet profound changes in CO_2 and climate occurred.
113 Identifying the most reliable Cenozoic CO_2 estimates published to date allows us to quantify
114 important physical (e.g., temperature, ice volume) and biological (i.e., physiological, ecosystem)
115 thresholds and tipping points.

116 We structure this investigation as follows: First we summarize the methodology by which
117 we assessed the CO_2 proxies and associated estimates. We then apply these methods to derive
118 a series of paleo CO_2 compilations comprised of data with different levels of quality or
119 confidence, and statistically integrate the 'top-tier' data to create a realization of the Cenozoic
120 variability in atmospheric CO_2. This is followed by a discussion of the climatic implications
121 (including climate sensitivity) of the paleo-CO_2 curve, and a presentation of an evolutionary
122 perspective. We finish with a roadmap for further advances in understanding past changes in
123 atmospheric CO_2.

124

125 **Critical assessment of atmospheric CO_2 proxies**

126 The basis of our synthesis is a set of comprehensive data templates documenting all types
127 of proxy data and their corresponding CO_2 estimates (a total of 6,247 data points). The completed
128 data sheets for each study can be accessed as the paleo-CO_2 'Archive' in NOAA's National Climatic
129 Data Center (NCDC). These 'Archive' sheets report all underlying data at face value from the
130 original publications, but their unprecedented level of detail is designed to facilitate critical
131 evaluation and recalculation of each CO_2 estimate.

132 From the 'Archive', published CO_2 estimates were evaluated by teams of experts who are
133 active in validating and applying these proxies, and often included the original authors of the
134 respective data. No new proxy data were collected as part of this effort, but estimates were
135 recalculated where needed and possible, and age models were revised where new evidence was
136 readily accessible. Additionally, CO_2 and age uncertainties were updated, as necessary, to
137 consistently reflect propagated 95% confidence intervals. The vetting criteria are summarized in
138 Supplementary Table S1 and detailed in paleo-CO_2 'Product' (note: link to be inserted after
139 acceptance of this manuscript for publication) sheets. These CO_2 estimates are categorized as
140 follows: 'Category 1' estimates (Fig. 1a, 1,673 data points or ~27% of the original total) are based

on data whose uncertainty is fully documented and quantifiable in view of current proxy understanding. 'Category 2' estimates (Fig. 1b, 1,813 data points) contain sources of uncertainty that are not yet fully constrained. These uncertainties vary between proxies and datasets, and include, e.g., insufficient replication, poorly constrained proxy sensitivity to parameters other than CO_2, or extrapolation of calibration curves. 'Category 3' estimates (the residual 2,761 data points or ~44% of the Cenozoic paleo-CO_2 estimates published to date) are either superseded by newer, independently published evaluations from the same raw data, are considered unreliable due to factors such as incomplete supporting datasets that prevent full quantification of uncertainties, or outdated sample preparation methods.

Although objective criteria are applied throughout, the vetting process was particularly challenging for the paleosol- and phytoplankton-based proxies because multiple approaches are currently in use for interpreting these proxy data (*35-41*). Given the lack of a universally agreed-upon method, we compare multiple approaches for treating the data of these two proxies whenever possible. For the paleosol proxy, the greatest source of uncertainty is in the estimation of paleo-soil CO_2 concentration derived from respiration. Two different approaches are commonly used to do this. The first method is based on proxy-estimated mean annual rainfall, while the second is based on soil order (i.e., the most general hierarchical level in soil taxonomy, comparable to kingdom in the classification of biological organisms). However, few records in the database allow for a direct comparison between the two approaches. An opportunity for comparison exists with two Eocene records (*37, 42*), where re-calculation using each of the two different methods leads to CO_2 estimates that do not overlap within 95% confidence intervals for most stratigraphic levels (Fig. S6). This implies that the uncertainty in estimating paleo-soil CO_2 concentration derived from respiration cannot be fully quantified with either of these approaches. Thus, most paleosol-based CO_2 estimates were designated as Category 2. For the phytoplankton proxy, routinely applied methods differ in how algal cell size and growth rate are accounted for, as well as the assumed sensitivity of algal $\delta^{13}C$ values to aqueous CO_2 concentration (see Supplementary Materials for details). Where data are available, we compare both newer and traditional methods, finding that although there are deviations between the resulting CO_2 estimates, they do agree within 95% confidence intervals. We hence assign many phytoplankton CO_2 estimates to Category 1 and present mean CO_2 and uncertainty values that reflect the range of results from the different methods.

Towards a Cenozoic history of atmospheric CO_2

Our composite Category 1 and 2 realizations of Cenozoic CO_2 (Figs. 1a and b) display much better agreement among proxies than does the 'raw', un-curated collection ('Archive', Fig. 1c). Encouragingly, objective criteria applied to the original data products automatically placed the earlier-reported estimates of 'negative' CO_2, as well as some unusually high values, into Category 3, and without subjective intervention to otherwise filter them. We note that the Category 1 composite is now largely dominated by marine proxy estimates, with some intervals (e.g., the middle Paleocene, ~63-57 Ma) very sparsely sampled. Furthermore, some intervals (e.g., Oligocene, Miocene) still exhibit significant differences between proxies; for instance, marine-based CO_2 estimates start high and decline during the Oligocene (~34-23 Ma), whereas plant-

based estimates suggest overall lower and constant CO_2 (Fig. 1a). Estimates of global temperature (Fig. 2b) during this time interval are largely invariant, which leaves us with the questions of whether CO_2 and climate were decoupled during this interval, or whether there is a systematic bias in the marine or plant-based CO_2 proxies and/or in the temperature proxies. All proxies become more uncertain further back in time as our knowledge of vital effects in biological proxy carriers, secular changes in the elemental and isotopic composition of ocean and atmosphere, as well as proxy sensitivity to environmental parameters that change along with CO_2 (e.g., temperature, rainfall, see Supplementary Materials for details) becomes less certain. In some cases, ancillary constraints and uncertainties are shared across multiple proxies (e.g., assumed atmospheric $\delta^{13}C$ is common to proxies based on land plant $\delta^{13}C$, leaf gas exchange, and paleosols), creating interdependence of estimates from seemingly independent proxies. More robust paleo-CO_2 reconstruction thus requires not only continued application of all proxies but also replication from different locations.

Although some uncertainties and proxy disagreements remain, the much-improved agreement within the vetted paleo-CO_2 compilation gives us confidence that a quantitative reconstruction of Cenozoic CO_2 based on the combined Category 1 data is possible. To do so, we statistically model mean CO_2 values at half-million-year intervals, together with uncertainties in age and proxy CO_2 estimates (Fig. 2a, see Supplementary Materials for details). Our choice of a 500-kyr resolution interval reflects a compromise driven by the proxy data compilation. Although parts of the Cenozoic, particularly the Plio-Pleistocene, are sampled at higher temporal resolution, the density of records remains relatively sparse throughout much of the Paleogene (1 datum per 190 kyr on average). As a result, the data (and in some cases the underlying age models) are not suited to interpreting higher-frequency (e.g., Milankovitch-scale) variations in atmospheric composition, and we focus here on low-frequency (e.g., multi-million year) trends and transitions. Proxy sampling within some intervals may be biased toward conditions that deviate from the 500-kyr mean (most notably here, the Paleocene-Eocene Thermal Maximum, PETM). We do not attempt to remove this bias but recommend caution in interpreting any features expressed at sub-million-year timescales.

This curve (Fig. 2a) allows us to constrain Cenozoic paleo-CO_2 and its uncertainty with greater confidence than earlier efforts. The highest CO_2 values of the past 66 Myr appear during the Early Eocene Climatic Optimum (EECO, ~53-51 Ma), while the lowest values occur during the Pleistocene. In contrast to earlier compilations, which suggested early Cenozoic CO_2 concentrations <400 ppm (e.g., *33*), rigorous data vetting and newly published records place early Paleocene mean CO_2 in our reconstruction between 650 and 850 ppm. However, the Paleocene remains data poor, and uncertainty in the curve remains large. Although the Paleocene record is predominantly based on the boron isotope proxy (Fig. 1a), inclusion of other (non-marine) proxy data does influence and refine the reconstruction through this epoch, supporting the value of the multi-proxy approach (Fig. S10). Following the rapid CO_2 rise and fall associated with the PETM at 56 Ma, mean CO_2 steadily rose to peak values of ~1600 ppm around 51 Ma during the EECO. The middle and late Eocene recorded slightly lower values (800-1100 ppm). Mean CO_2 dropped to <600 ppm across the Eocene-Oligocene transition (EOT, 33.9 Ma) and reached values that generally fall between ~400 and 200 ppm during the Miocene through Pleistocene, except for a notable increase during the Middle Miocene (~17-15 Ma) to a mean of ~500 ppm.

Uncertainty in the mean CO_2 values drops substantially in the Plio-Pleistocene (see also Fig. S11), as expected given a dramatic increase in data density. Our analysis suggests that ~14.5-14 Ma was the last time 500-kyr-mean CO_2 value was as high as the present (Fig. S11), and that all Plio-Pleistocene peak interglacial CO_2 concentrations were exceptionally likely less than those of the modern atmosphere (Fig. S12). In contrast, prior to the Miocene, there is very little support (<2.5% probability) for Cenozoic 500-kyr-mean CO_2 values reaching or falling below pre-industrial levels.

Climatic implications of the revised CO_2 curve

Relationship with global temperature change and climate sensitivity

Our reconstructed Cenozoic CO_2 trends are broadly coherent with those for global temperature as inferred, e.g., from the oxygen isotopic composition ($\delta^{18}O$) of fossil benthic foraminifera shells (*43, 44*) and compilations of global surface temperature (*45*) (Fig. 2b). The Paleocene and Eocene epochs display overall higher temperatures and atmospheric CO_2 concentrations as compared to the later Oligocene, Miocene, and Pliocene - consistent with a predominantly greenhouse-gas regulated global energy budget. More specifically, the slow rise and subsequent fall of CO_2 over the course of the Paleocene and Eocene are mirrored by global temperatures, just as a transient Miocene CO_2 rise coincides with a period of warming at the Miocene Climatic Optimum (MCO). The EOT is identifiable in both the CO_2 and temperature records, despite the smoothing introduced by the curve fitting and 500-kyr binning interval.

Despite this overall agreement, rates and timing of CO_2 vs. temperature changes in the two records are not always synchronized (Fig. 2a,b). For example, CO_2 appears broadly static or even rising during the late Eocene (37-34 Ma) and late Miocene (11-5 Ma) despite global cooling (see also *46*) at these times. Conversely, decreasing CO_2 during the early Oligocene corresponds with relatively stable global temperatures (Fig. 2b, but see also *47, 48*) and ice volume (Fig. 2c) at that time. We note that the reconstructed Oligocene CO_2 decrease is driven by the contribution of marine proxies to the composite curve, whereas estimates from leaf gas exchange proxies are low and broadly static (Fig. 1c), a discrepancy that cannot be resolved without further experimentation and data collection. We caution that, even at the 500-kyr resolution of our study, the relative timing of CO_2 and temperature change might be unresolved in poorly sampled intervals (i.e., middle Paleocene), but should be well resolved during more recent, well sampled intervals (i.e., late Miocene through present, Fig. S8). Is the occasional divergence of temperature and CO_2 change evidence for occasional disconnects between CO_2 forcing and climate response? Although one might posit bias in the CO_2 reconstruction, the strength of our multiproxy approach is the reduced likelihood that multiple proxies exhibit common bias during particular periods of the Cenozoic. We suggest that some cases of divergence between temperature and CO_2 could reflect non-CO_2 effects on climate (e.g., changes in paleogeography affecting ocean circulation, albedo and heat transport, *49*), or the temperature reconstructions used herein could be biased by non-thermal influences (e.g., uncertain elemental and isotopic composition of paleo-seawater, physiological or pH effects on proxies, *48, 50*).

Our updated CO_2 curve, in conjunction with existing global temperature reconstructions, gives us the opportunity to reassess how climate sensitivity might have evolved through the Cenozoic. The most commonly reported form of climate sensitivity is equilibrium climate sensitivity (ECS), which focuses on fast feedback processes (e.g., clouds, lapse rate, snow, sea ice) and is therefore best suited for predicting present-day warming (~3°C for a doubling of CO_2 above the pre-industrial condition, *2*). Because the average temporal resolution of our CO_2 database is coarser than 1000 years, we cannot estimate ECS directly. Instead, our data are most appropriate for interpreting an Earth System Sensitivity ($ESS_{[CO2],}$ following the taxonomy of *51*) – the combination of short-term climate responses to doubling CO_2 plus the effects of slower, geological feedback loops such as the growth and decay of continental ice sheets. We compare our reconstructed 500-kyr-mean CO_2 values with two different estimates of global surface temperature. We apply the same Bayesian inversion model used in the CO_2 reconstruction to derive 500-kyr-mean surface temperatures from the benthic foraminiferal $\delta^{18}O$ compilation of Ref. (*43*), which we convert to temperatures using the methodology of Ref. (*44*) (Fig. 2b). In addition, we pair a set of multiproxy global surface temperature estimates for eight Cenozoic time intervals (Fig. 2b, *45*) with posterior CO_2 estimates from time bins corresponding to each interval. The two temperature reconstructions are broadly similar, although the benthic record suggests relatively higher temperatures during the hothouse climate of the Paleocene and Eocene, whereas the multiproxy reconstruction is elevated relative to the benthic record during the Oligocene and Neogene.

The co-evolution of atmospheric CO_2 and global mean surface temperature (GMST) over the Cenozoic is shown in Fig. 3. Because CO_2 is on a log scale, the slopes of lines connecting two adjacent points in time reflect the average intervening $ESS_{[CO2]}$. Benthic $\delta^{18}O$-derived temperatures suggest early Paleocene warming occurs with a very high $ESS_{[CO2]}$ (>8°C per CO_2 doubling), although CO_2 uncertainties are large during this time interval. $ESS_{[CO2]}$ steadily declines towards the peak of Cenozoic warmth ~50 Ma, then steepens again to ~8°C per CO_2 doubling for much of the cooling through to the EOT at ~34 Ma. In contrast, the multiproxy global temperature record suggests a lower $ESS_{[CO2]}$ of ~5°C between the early Eocene and earliest Oligocene. During the Oligocene and early part of the Miocene, both temperature records imply a near-zero $ESS_{[CO2]}$, i.e., CO_2 values appear to decline with no appreciable global cooling. $ESS_{[CO2]}$ implied by both temperature reconstructions steepens again from the middle Miocene (~16 Ma) to present, averaging 8°C per CO_2 doubling over the past 10 Myr.

An alternative perspective on early Cenozoic climate forcing was introduced by Ref. (*44*), who hypothesized that all pre-Oligocene climate change was the response of direct and indirect CO_2 radiative forcing plus long-term change in solar output (i.e., constant albedo). Given this, they converted Paleocene and Eocene benthic $\delta^{18}O$-derived GMST to estimates of CO_2 change required to explain the temperature record. Our reconstruction offers a direct test of this hypothesis, and although it compares well with the $\delta^{18}O$ approach of Ref. (*44*) throughout much of the early Cenozoic, our curve suggests that the late Eocene decline in CO_2 was less severe than expected under the constant albedo assumption (Fig. S13). This result is consistent with a growing contribution of glacier and sea ice albedo effects (e.g., *52, 53*) and the opening of Southern Ocean gateways (e.g., *54*) to climate cooling preceding the Eocene-Oligocene boundary.

In summary, the Cenozoic compilation confirms a strong link between CO_2 and GMST across timescales from 500 kyr to tens of Myr, with $ESS_{[CO2]}$ generally within the range of 5-8°C – patterns consistent with most prior work (*32-34, 45, 51, 55-60*), and considerably higher than the present-day ECS of ~3°C. Both temperature reconstructions imply relatively high $ESS_{[CO2]}$ values during the last 10 Myr of the Cenozoic, when global ice volumes were highest. This agrees with expectations of an amplified $ESS_{[CO2]}$ due to the ice-albedo feedback (*61*). However, even during times with little-to-no ice (Paleocene to early Eocene), we find elevated values of $ESS_{[CO2]}$ (approaching or exceeding 5°C per CO_2 doubling). This implies that fast, non-ice feedbacks, such as clouds or non-CO_2 greenhouse gases (*60, 62-65*) were probably stronger in the early Paleogene than they are in the present-day climate system (see also *5*). The Oligocene to early Miocene is the most enigmatic interval, with an apparent decrease in CO_2 despite relatively stable temperature, implying near zero $ESS_{[CO2]}$. It should be noted that this is one interval where different CO_2 proxies disagree on CO_2 change (Fig. 1a), with relatively stable values from plants but a decline in values from alkenones. More work is needed to confirm these CO_2 and temperature findings, but if these estimates are correct, this could partly reflect transition from a climate state too cold to support the strong fast feedbacks (e.g., clouds) of the early Eocene (*5*), but not cold enough to generate strong ice-albedo feedback. Tectonic changes in the arrangement of continents and the opening of critical ocean gateways may also be confounding derivation of $ESS_{[CO2]}$ at that time (e.g., *49, 54*).

Relationship with the evolution of the cryosphere

Our composite CO_2 record also enables reexamination of the evolution of Earth's cryosphere (Fig. 2c) in relation to CO_2 radiative forcing. We use the sea level estimation of Ref. (*66*) for this comparison because it covers the entire Cenozoic and is somewhat independent of the benthic $\delta^{18}O$ stack (*43*) used for the GMST derivation in Fig. 2b and also of the more recent sea level reconstruction of Ref. (*67*). Although there are significant differences between the two sea level estimates, the main features discussed herein are broadly consistent between them. The establishment of a permanent, continent-wide Antarctic ice shield at the EOT (~34 Ma) comes at the end of a ~10-Myr period of generally slowly decreasing CO_2. There is evidence for isolated, unstable Antarctic glaciers at various points over the 10-Myr interval prior to the EOT (*50, 53, 66, 68*), which is consistent with the increasing paleogeographic isolation of Antarctica and Southern Ocean cooling (*54*), and CO_2 may have been sufficiently low to enable the repeated crossing of a glaciation threshold by periodic orbital forcing. Tectonic cooling of Antarctica would have progressively raised the CO_2 glaciation threshold, which has been modeled to be within 560-920 ppm (*69, 70*). Our composite CO_2 record allows us to further assess this glaciation threshold but requires determining the point during glacial inception when strong positive feedbacks (e.g., ice-albedo and ice sheet elevation) commenced and ice sheet growth accelerated (*71*). Using the sea level curve of Ref. (*66*), we determine this point as 33.75 ±0.25 Ma, where our composite CO_2 record suggests 719 $\frac{+180}{-152}$ ppm (95% CIs). Once established, the land-based Antarctic ice sheet likely persisted for the remainder of the Cenozoic, although significant retreat of land-based ice has been modeled (30-36 m sea level equivalent, *72*) and estimated from proxies (Fig. 2c) for the Miocene Climatic Optimum (MCO). 500-kyr-mean CO_2 values increased to ~500 ppm during the MCO (Figs. 2a, S10), and benthic foraminiferal $\delta^{18}O$ (Fig. 2b, *43*) and clumped isotopes (*50*)

indicate warming. While the stability of the land-based Antarctic ice sheet depends on many factors in addition to CO_2-induced global warming (e.g., hysteresis (*73*), bed topography (*74*)), our composite record indicates that significant retreat of land-based ice did not occur below 441-480 ppm (2.5-50 percentiles), and some land-based ice may have persisted up to 563 ppm (97.5 percentile) during the MCO. Excepting the MCO, atmospheric CO_2 has remained below our current value of 419 ppm since the late Oligocene (Figs. 2a, S10), with relatively small sea-level variations (up to ~20m, Fig. 2c and *67*) being driven by orbitally-forced melting of the marine-based ice sheet (e.g., *72, 75*). Finally, at ~2.7 Ma, the transition to intensified northern hemisphere glaciation and orbitally-driven glacial cycles coincided with CO_2 values that began decreasing after a relative high during the Pliocene (Fig. 2a).

Evolutionary implications of the revised CO_2 curve

While geologic trends in terrestrial floral and faunal habitat ranges (e.g., *76, 77*) and diversity (e.g., *78, 79, 80*) are largely thought to be controlled by temperature and associated climate patterns, atmospheric CO_2 has been hypothesized to drive the evolution of biological carbon concentrating mechanisms and their subsequent diversification in terrestrial plants (CCMs, Fig. 2d, *81, 82*). Our realization of how atmospheric CO_2 has varied through the Cenozoic allows us to re-examine this hypothesis. The two primary CCMs in terrestrial plants are the crassulacean acid metabolism (CAM) and C_4 photosynthetic syndromes. CCMs in terrestrial C_4 and CAM plants confer competitive advantages over the ancestral C_3 pathway under higher growing season temperatures, low rainfall, and lower atmospheric CO_2. As a result, C_4 photosynthesis contributes about 23% of today's global terrestrial gross primary production (GPP, *83*).

Plant clades with the C_4 pathway first emerged in the early Oligocene (*84, 85*), yet did not expand to ecological significance until the late Miocene (i.e., <5% GPP before ~10 Ma, Fig. 2d, *86, 87, 88*). CAM plants (e.g., cacti, ice plants, agaves, and some orchids) underwent significant diversification events around the late Oligocene and late Miocene (*89-91*). Taken together, two general biological thresholds emerge based on our CO_2 record: (1) All known origins of C_4 plants occurred when atmospheric CO_2 was lower than ~550 ppm (i.e., after 32 Ma, Fig. 2a,d, *84*), which is in agreement with theoretical predictions (*92, 93*). (2) All major Cenozoic CAM diversification events coincided with intervals when CO_2 was lower than ~430 ppm (i.e., after 27 Ma, *89, 90*). Our record is thus consistent with decreasing atmospheric CO_2 (< 550 ppm) being a critical threshold for the Cenozoic origin, diversification, and expansion of C_4 and CAM plants within grasslands, arid habitats (such as deserts), and habits (such as epiphytes), and provides strong data support for previous hypotheses (*20, 84, 86, 88, 89, 92, 94, 95*). Importantly, following their origin in the early Oligocene, C_4 plants did not immediately proliferate. By ~24 to ~18 Ma, open habitat grasslands are evident on most continents (*96*), yet widespread dispersal of C_4 plants was delayed until the late Miocene, and without any apparent decline in CO_2 (Fig. 2d). Therefore, the rise of C_4 plants to their dominance in many tropical and subtropical ecosystems was likely driven (and maintained today) by other factors such as fire, seasonality of rainfall, and herbivory (i.e., grazing that keeps landscapes open) (*97, 98*). The temporal evolution of these factors warrants further study as we move towards a future where CO_2 may rise above the 550-ppm threshold that was key to the origin, taxonomic diversification, and spread of C_4 plants.

Terrestrial mammals evolved and adapted to the changing and more open floral ecosystems of the late Cenozoic (*99-101*), and are thus indirectly linked to the 550-ppm atmospheric CO_2 threshold discovered herein. In particular, dental wear patterns (such as the shape of the chewing surface of a tooth, i.e., mesowear) and tooth morphology, such as crown height, reflect an increasingly abrasive and tough diet (*102, 103*), and can be traced across many herbivore lineages during this period. For instance, mesowear in North American Equidae (horses and their ancestors, Fig. 2d) began to increase in the late Eocene, and steadily continued into the Quaternary. Similarly, equids evolved high-crowned (hypsodont) teeth in the Miocene (*103-105*), and their body size increased to accommodate higher intake of more abrasive, grassy vegetation (Fig. 2d).

Evolutionary trends are a little less clear in the ocean, because marine algal CCMs are ubiquitous and diverse in form (*106*) and are believed to have an ancient origin. Moreover, the large spatial and seasonal variance of dissolved CO_2 in the surface ocean (as compared to the relatively uniform seasonal and spatial concentration of CO_2 in the air) may somewhat decouple their evolution from geologic trends in atmospheric CO_2. Evidence exists that marine algae, and in particular the coccolithophores (i.e., the source of the alkenone biomarkers), express CCMs to greater extent when CO_2 is lower (e.g., *107, 108, 109*), with estimates of cellular carbon fluxes suggesting enhanced CCM activity in coccolithophores began ~7-5 Ma (*110*). However, our revised CO_2 curve displays mean atmospheric CO_2 broadly constant at 300-350 ppm since at least ~14 Ma (Figs. 2a, S10), suggesting that increased CCM activity may reflect other proximal triggers, perhaps involving changes in ocean circulation and nutrient supply.

Perspectives and opportunities for further advances

Our community-assessed composite CO_2 record and statistically modelled time-averaged CO_2 curve exhibit greater clarity in the Cenozoic evolution of CO_2 and its relationship with climate than was possible in previous compilations, and furthermore highlight the value of cross-disciplinary collaboration and community building. Generating a paleo-CO_2 record with even greater confidence requires targeted efforts using multiple proxies to fill in data gaps, higher resolution and replication from multiple locations, and novel approaches to resolve remaining differences between CO_2 proxy estimates. Specifically: although the number and diversity of paleo-CO_2 proxy records continues to grow, data remain relatively sparse during several key parts of the Cenozoic record (e.g., middle Paleocene, Oligocene). Moreover, records from the Paleocene and Eocene are dominated by estimates from the boron isotope proxy, increasing potential for bias. Targeted efforts are hence needed to expand the number and diversity of data through these intervals and to refine multi-proxy reconstructions. Secondly, despite substantial progress, there remains a lack of consensus regarding the identity and/or quantification of some of the factors underlying each of the proxy systems analyzed here. New experimental and calibration studies, particularly those that isolate and quantify specific mechanistic responses and/or their interactions, need to be undertaken in order to reduce potential biases and uncertainty for each method. For instance, the emerging fields of genomics, evolutionary and developmental biology, and proteomics provide exciting new opportunities for improving and

understanding paleo-proxy systematics. Thirdly, and associated with improved experimental quantification, refining our theoretical and mechanistic understanding of how proxies are encoded will allow us to create explicit and self-consistent representations of the processes involved. The development of proxy system forward models provides a promising leap in this direction (e.g., *111*). Bayesian statistical methods can then enable the full suite of models and data to be integrated and constrain the range of environmental conditions, including atmospheric CO_2 and other variables that are consistent with the multiproxy data (*112, 113*). Finally, development of new proxies is also a realistic and desirable aim. For instance, while this study focuses on more established proxies, new proxies such as coccolith calcite stable isotopes (*114*) and mammalian bone and teeth oxygen-17 anomalies (*115*) show promising results for reconstructing paleo-CO_2, but perhaps require further validation before they can be assessed with confidence.

Proxies and proxy-based reconstructions of how atmospheric CO_2 has varied through deep time have improved immeasurably over the past few decades. While they will never allow us to reconstruct past CO_2 with the same fidelity as direct air measurement, our study shows how community-based consensus assessment, together with a critical reanalysis of proxy models and assumptions, can progressively move us towards a quantitative history of atmospheric CO_2 for geological time.

References and Notes

1. S. Arrhenius, *Philosophical Magazine* **41**, 237 (1896).
2. IPCC, *Climate Change 2021: The Physical Science Basis. Contribution of Working Group I to the Sixth Assessment Report of the Intergovernmental Panel on Climate Change*. V. Masson-Delmotte, P. Zhai, A. Pirani, S. L. Connors, C. Péan, S. Berger *et al.*, Eds., (Cambridge University Press, Cambridge, United Kingdom and New York, NY, USA, 2021).
3. P. Tans, R. Keeling, NOAA/ESRL, Ed. (NOAA/ESRL, www.esrl.noaa.gov/gmd/ccgg/trends/, 2023).
4. K. E. Taylor, R. J. Stouffer, G. A. Meehl, *Bulletin of the American Meteorological Society* **93**, 485 (2012/04/01, 2011).
5. R. Caballero, M. Huber, *Proceedings of the National Academy of Sciences USA* **110**, 14162 (August 5, 2013, 2013).
6. J. Zhu, C. J. Poulsen, *Geophysical Research Letters* **47**, e2020GL089143 (2020/09/28, 2020).
7. J. Zhu, C. J. Poulsen, B. L. Otto-Bliesner, *Nature Climate Change* **10**, 378 (2020/05/01, 2020).
8. E. J. Judd, J. E. Tierney, B. T. Huber, S. L. Wing, D. J. Lunt, H. L. Ford *et al.*, *Scientific Data* **9**, 753 (2022/12/06, 2022).
9. R. J. Delmas, J.-M. Ascencio, M. Legrand, *Nature* **284**, 155 (1980).
10. A. Neftel, H. Oeschger, J. Schwander, B. Stauffer, R. Zumbrunn, *Nature* **295**, 220 (1982).
11. B. Bereiter, S. Eggleston, J. Schmitt, C. Nehrbass-Ahles, T. F. Stocker, H. Fischer *et al.*, *Geophysical Research Letters* **42**, 542 (2015).
12. Y. Yan, M. L. Bender, E. J. Brook, H. M. Clifford, P. C. Kemeny, A. V. Kurbatov *et al.*, *Nature* **574**, 663 (2019/10/01, 2019).
13. J. A. Higgins, A. V. Kurbatov, N. E. Spaulding, E. Brook, D. S. Introne, L. M. Chimiak *et al.*, *Proceedings of the National Academy of Sciences* **112**, 6887 (June 2, 2015, 2015).
14. C. Nehrbass-Ahles, J. Shin, J. Schmitt, B. Bereiter, F. Joos, A. Schilt *et al.*, *Science* **369**, 1000 (2020).
15. C. Le Quéré, M. R. Raupach, J. G. Canadell, G. Marland, et al., *Nature Geosci* **2**, 831 (2009).
16. P. Friedlingstein, M. O'Sullivan, M. W. Jones, R. M. Andrew, L. Gregor, J. Hauck *et al.*, *Earth Syst. Sci. Data* **14**, 4811 (2022).
17. P. Valdes, *Nat. Geosci.* **4**, 414 (2011/07/01, 2011).
18. W. Kiessling, M. Aberhan, L. Villier, *Nature Geosci* **1**, 527 (2008).
19. J. L. Payne, A. M. Bush, N. A. Heim, M. L. Knope, D. J. McCauley, *Science* **353**, 1284 (2016).
20. E. J. Edwards, C. P. Osborne, C. A. Strömberg, S. A. Smith, W. J. Bond, P. A. Christin *et al.*, *Science* **328**, 587 (Apr 30, 2010).
21. F. A. McInerney, S. L. Wing, *Annual Review of Earth and Planetary Sciences* **39**, 489 (2011/05/30, 2011).
22. W. Konrad, D. L. Royer, P. J. Franks, A. Roth-Nebelsick, *Geological Journal*, (2020/03/18, 2020).

23. J. C. McElwain, M. Steinthorsdottir, *Plant Physiology* **174**, 650 (2017).
24. B. A. Schubert, A. H. Jahren, *Geochim. Cosmochim. Acta* **96**, 29 (2012).
25. T. E. Cerling, *Am. J. Sci.* **291**, 377 (1991).
26. D. O. Breecker, *Geochemistry, Geophysics, Geosystems* **14**, 3210 (2013/08/01, 2013).
27. E. A. Jagniecki, T. K. Lowenstein, D. M. Jenkins, R. V. Demicco, *Geology* **43**, 1075 (December 1, 2015, 2015).
28. T. K. Lowenstein, R. V. Demicco, *Science* **313**, 1928 (2006).
29. M. Pagani, in *Treatise on Geochemistry (Second Edition),* H. D. Holland, K. K. Turekian, Eds. (Elsevier, Oxford, 2014), pp. 361-378.
30. B. Hönisch, S. M. Eggins, L. L. Haynes, K. A. Allen, K. Holland, K. Lorbacher, *Boron proxies in Paleoceanography and Paleoclimatology*. Analytical Methods in Earth and Environmental Science (John Wiley & Sons, Ltd., 2019).
31. J. W. B. Rae, in *Boron Isotopes: The Fifth Element,* H. Marschall, G. Foster, Eds. (Springer International Publishing, Cham, 2018), pp. 107-143.
32. D. J. Beerling, D. L. Royer, *Nat. Geosci.* **4**, 418 (2011).
33. G. L. Foster, D. L. Royer, D. J. Lunt, *Nature Communications* **8**, 14845 (04/04/online, 2017).
34. J. W. B. Rae, Y. G. Zhang, X. Liu, G. L. Foster, H. M. Stoll, R. D. M. Whiteford, *Annual Review of Earth and Planetary Sciences* **49**, 609 (2021).
35. S. Ji, J. Nie, A. Lechler, K. W. Huntington, E. O. Heitmann, D. O. Breecker, *Earth and Planetary Science Letters* **499**, 134 (2018/10/01/, 2018).
36. J. Da, Y. G. Zhang, G. Li, X. Meng, J. Ji, *Nature Communications* **10**, 4342 (2019/09/25, 2019).
37. E. Hyland, N. D. Sheldon, M. Fan, *GSA Bulletin* **125**, 1338 (2013).
38. J. Henderiks, M. Pagani, *Paleoceanography* **22**, (2007).
39. S. R. Phelps, G. M. M. Hennon, S. T. Dyhrman, M. D. Hernández Limón, O. M. Williamson, P. J. Polissar, *Geochemistry, Geophysics, Geosystems* **22**, e2021GC009657 (2021/07/01, 2021).
40. H. M. Stoll, J. Guitian, I. Hernandez-Almeida, L. M. Mejia, S. Phelps, P. Polissar *et al.*, *Quaternary Science Reviews* **208**, 1 (2019/03/15/, 2019).
41. Y. G. Zhang, J. Henderiks, X. Liu, *Geochimica et Cosmochimica Acta* **281**, 118 (2020/07/15/, 2020).
42. E. G. Hyland, N. D. Sheldon, *Palaeogeography, Palaeoclimatology, Palaeoecology* **369**, 125 (2013).
43. T. Westerhold, N. Marwan, A. J. Drury, D. Liebrand, C. Agnini, E. Anagnostou *et al.*, *Science* **369**, 1383 (2020).
44. J. Hansen, M. Sato, G. Russell, P. Kharecha, *Philosophical Transactions of the Royal Society A: Mathematical, Physical and Engineering Sciences* **371**, 20120294 (2013/10/28, 2013).
45. S. J. Ring, S. G. Mutz, T. A. Ehlers, *Paleoceanography and Paleoclimatology* **37**, e2021PA004364 (2022/12/01, 2022).
46. T. D. Herbert, K. T. Lawrence, A. Tzanova, L. C. Peterson, R. Caballero-Gill, C. S. Kelly, *Nature Geosci* **9**, 843 (11//print, 2016).

47. D. E. Gaskell, M. Huber, L. O'Brien Charlotte, N. Inglis Gordon, R. P. Acosta, J. Poulsen Christopher *et al.*, *Proceedings of the National Academy of Sciences* **119**, e2111332119 (2022/03/15, 2022).
48. C. L. O'Brien, M. Huber, E. Thomas, M. Pagani, J. R. Super, L. E. Elder *et al.*, *Proceedings of the National Academy of Sciences* **117**, 25302 (2020).
49. D. J. Lunt, A. Farnsworth, C. Loptson, G. L. Foster, P. Markwick, C. L. O'Brien *et al.*, *Clim. Past* **12**, 1181 (2016).
50. A. N. Meckler, P. F. Sexton, A. M. Piasecki, T. J. Leutert, J. Marquardt, M. Ziegler *et al.*, *Science* **377**, 86 (2022/07/01, 2022).
51. PALEOSENS-project-members, *Nature* **419**, 683 (2012).
52. A. Tripati, D. Darby, *Nature Communications* **9**, 1038 (2018/03/12, 2018).
53. H. D. Scher, S. M. Bohaty, B. W. Smith, G. H. Munn, *Paleoceanography* **29**, 628 (2014/06/01, 2014).
54. I. Sauermilch, J. M. Whittaker, A. Klocker, D. R. Munday, K. Hochmuth, P. K. Bijl *et al.*, *Nature Communications* **12**, 6465 (2021/11/09, 2021).
55. D. L. Royer, *Annual Review of Earth and Planetary Sciences* **44**, 277 (2016).
56. R. M. Brown, T. B. Chalk, A. J. Crocker, P. A. Wilson, G. L. Foster, *Nat. Geosci.* **15**, 664 (2022/08/01, 2022).
57. T. E. Wong, Y. Cui, D. L. Royer, K. Keller, *Nature Communications* **12**, 3173 (2021/05/26, 2021).
58. D. L. Royer, M. Pagani, D. J. Beerling, *Geobiology* **10**, 298 (2012/07/01, 2012).
59. J. E. Tierney, J. Zhu, M. Li, A. Ridgwell, G. J. Hakim, C. J. Poulsen *et al.*, *Proceedings of the National Academy of Sciences* **119**, e2205326119 (2022/10/18, 2022).
60. E. Anagnostou, E. H. John, T. L. Babila, P. F. Sexton, A. Ridgwell, D. J. Lunt *et al.*, *Nature Communications* **11**, 4436 (2020/09/07, 2020).
61. J. Hansen, M. Sato, P. Kharecha, D. Beerling, R. Berner, V. Masson-Delmotte *et al.*, *Open Atm. Sci. J.* **2**, 217 (2008).
62. J. T. Kiehl, C. A. Shields, *Philosophical Transactions of the Royal Society A* **371**, 20130093 (October 28, 2013, 2013).
63. J. Zhu, C. J. Poulsen, J. E. Tierney, *Science Advances* **5**, eaax1874 (2019).
64. D. J. Beerling, A. Fox, D. S. Stevenson, P. J. Valdes, *Proceedings of the National Academy of Sciences* **108**, 9770 (2011/06/14, 2011).
65. T. Schneider, C. M. Kaul, K. G. Pressel, *Nat. Geosci.* **12**, 163 (2019/03/01, 2019).
66. K. G. Miller, J. V. Browning, W. J. Schmelz, R. E. Kopp, G. S. Mountain, J. D. Wright, *Science Advances* **6**, eaaz1346 (2020).
67. E. J. Rohling, J. Yu, D. Heslop, G. L. Foster, B. Opdyke, A. P. Roberts, *Science Advances* **7**, eabf5326 (2021).
68. M. J. Henehan, K. M. Edgar, G. L. Foster, D. E. Penman, P. M. Hull, R. Greenop *et al.*, *Paleoceanography and Paleoclimatology* **35**, e2019PA003713 (2020/06/01, 2020).
69. E. Gasson, D. J. Lunt, R. DeConto, A. Goldner, M. Heinemann, M. Huber *et al.*, *Clim. Past* **10**, 451 (2014).
70. R. M. DeConto, D. Pollard, P. A. Wilson, H. Palike, C. H. Lear, M. Pagani, *Nature* **455**, 652 (2008).
71. R. M. DeConto, D. Pollard, *Nature* **421**, 245 (2003).

72. E. Gasson, R. M. DeConto, D. Pollard, R. H. Levy, *Proceedings of the National Academy of Sciences* **113**, 3459 (2016/03/29, 2016).
73. D. Pollard, R. M. DeConto, *Glob. Planet. Change* **45**, 9 (2005/02/01/, 2005).
74. G. J. G. Paxman, E. G. W. Gasson, S. S. R. Jamieson, M. J. Bentley, F. Ferraccioli, *Geophysical Research Letters* **47**, e2020GL090003 (2020/10/28, 2020).
75. J. J. Fürst, G. Durand, F. Gillet-Chaulet, L. Tavard, M. Rankl, M. Braun *et al.*, *Nature Climate Change* **6**, 479 (2016/05/01, 2016).
76. J. C. McElwain, *Annual Review of Plant Biology* **69**, 761 (2018/04/29, 2018).
77. S.-M. Popescu, J.-P. Suc, S. Fauquette, M. Bessedik, G. Jiménez-Moreno, C. Robin *et al.*, *Journal of Biogeography* **48**, 2771 (2021/11/01, 2021).
78. C. Jaramillo, M. J. Rueda, G. Mora, *Science* **311**, 1893 (Mar 31, 2006).
79. J. Y. Lim, H. Huang, A. Farnsworth, D. J. Lunt, W. J. Baker, R. J. Morley *et al.*, *Global Ecology and Biogeography* **31**, 425 (2022/03/01, 2022).
80. A. Graham, *Am J Bot* **98**, 336 (Mar, 2011).
81. J. R. Ehleringer, R. K. Monson, *Annual Review of Ecology and Systematics* **24**, 411 (1993).
82. H. Griffiths, in *Vascular plants as epiphytes,* U. Lüttge, Ed. (Springer, Berlin, 1989), pp. 42–86.
83. C. J. Still, J. A. Berry, G. J. Collatz, R. S. DeFries, *Glob. Biogeochem. Cycle* **17**, 6 (2003/03/01, 2003).
84. P.-A. Christin, G. Besnard, E. Samaritani, M. R. Duvall, T. R. Hodkinson, V. Savolainen *et al.*, *Current Biology* **18**, 37 (2008/01/08/, 2008).
85. A. Vicentini, J. C. Barber, S. S. Aliscioni, L. M. Giussani, E. A. Kellogg, *Glob. Change Biol.* **14**, 2963 (2008/12/01, 2008).
86. P. J. Polissar, C. Rose, K. T. Uno, S. R. Phelps, P. deMenocal, *Nat. Geosci.* **12**, 657 (2019/08/01, 2019).
87. L. Tauxe, S. J. Feakins, *Paleoceanography and Paleoclimatology* **35**, e2020PA003857 (2020/07/01, 2020).
88. T. E. Cerling, J. M. Harris, B. J. MacFadden, M. G. Leakey, J. Quade, V. Eisenmann *et al.*, *Nature* **389**, 153 (1997/09/01, 1997).
89. M. Arakaki, P. A. Christin, R. Nyffeler, A. Lendel, U. Eggli, R. M. Ogburn *et al.*, *Proc Natl Acad Sci U S A* **108**, 8379 (May 17, 2011).
90. T. J. Givnish, D. Spalink, M. Ames, S. P. Lyon, S. J. Hunter, A. Zuluaga *et al.*, *Proc. R. Soc. B.* **282**, (2015).
91. E. J. Edwards, *New Phytologist* **223**, 1742 (2019/09/01, 2019).
92. J. R. Ehleringer, T. E. Cerling, B. R. Helliker, *Oecologia* **112**, 285 (1997/10/01, 1997).
93. H. Zhou, B. R. Helliker, M. Huber, A. Dicks, E. Akçay, *Proceedings of the National Academy of Sciences* **115**, 12057 (2018/11/20, 2018).
94. C. E. R. Lehmann, S. A. Archibald, W. A. Hoffmann, W. J. Bond, *New Phytologist* **191**, 197 (2011/07/01, 2011).
95. W. M. Kürschner, Z. Kvacek, D. L. Dilcher, *Proceedings of the National Academy of Sciences USA* **105**, 449 (2008).
96. C. A. E. Strömberg, *Annual Review of Earth and Planetary Sciences* **39**, 517 (2011/05/30, 2011).

97. A. T. Karp, K. T. Uno, P. J. Polissar, K. H. Freeman, *Paleoceanography and Paleoclimatology* **36**, e2020PA004106 (2021/04/01, 2021).
98. T. Kukla, J. K. C. Rugenstein, D. E. Ibarra, M. J. Winnick, C. A. E. Strömberg, C. P. Chamberlain, *AGU Advances* **3**, e2021AV000566 (2022/04/01, 2022).
99. M. Fortelius, J. T. Eronen, F. Kaya, H. Tang, P. Raia, K. Puolamäki, *Annual Review of Earth and Planetary Sciences* **42**, 579 (2014/05/30, 2014).
100. F. Kaya, F. Bibi, I. Žliobaitė, J. T. Eronen, T. Hui, M. Fortelius, *Nature Ecology & Evolution* **2**, 241 (2018/02/01, 2018).
101. C. M. Janis, J. Damuth, J. M. Theodor, *Proceedings of the National Academy of Sciences* **97**, 7899 (2000).
102. M. Fortelius, N. Solounias, *American Museum Novitates* **3301**, 1 (2000).
103. M. C. Mihlbachler, F. Rivals, N. Solounias, G. M. Semprebon, *Science* **331**, 1178 (2011/03/04, 2011).
104. C. A. E. Strömberg, *Paleobiology* **32**, 236 (2006).
105. C. M. Janis, M. Fortelius, *Biol Rev Camb Philos Soc* **63**, 197 (May, 1988).
106. M. R. Badger, D. Hanson, G. D. Price, *Funct Plant Biol* **29**, 161 (Apr, 2002).
107. M. P. S. Badger, *Biogeosciences* **18**, 1149 (2021).
108. Y. G. Zhang, M. Pagani, Z. Liu, S. M. Bohaty, R. DeConto, *Philosophical Transactions of the Royal Society A: Mathematical, Physical and Engineering Sciences* **371**, (October 28, 2013, 2013).
109. P. D. Tortell, *Limnology and Oceanography* **45**, 744 (2000/05/01, 2000).
110. C. T. Bolton, H. M. Stoll, *Nature* **500**, 558 (2013).
111. M. N. Evans, S. E. Tolwinski-Ward, D. M. Thompson, K. J. Anchukaitis, *Quaternary Science Reviews* **76**, 16 (2013/09/15/, 2013).
112. G. J. Bowen, B. Fischer-Femal, G. J. Reichart, A. Sluijs, C. H. Lear, *Clim. Past* **16**, 65 (2020).
113. M. B. Osman, J. E. Tierney, J. Zhu, R. Tardif, G. J. Hakim, J. King *et al.*, *Nature* **599**, 239 (2021/11/01, 2021).
114. C. Godbillot, F. Minoletti, F. Bassinot, M. Hermoso, *Clim. Past* **18**, 449 (2022).
115. A. Pack, A. Gehler, A. Süssenberger, *Geochimica et Cosmochimica Acta* **102**, 306 (2013/02/01/, 2013).
116. C. R. Scotese, *Annual Review of Earth and Planetary Sciences* **49**, 679 (2021/05/30, 2021).
117. P. A. Christin, C. P. Osborne, R. F. Sage, M. Arakaki, E. J. Edwards, *Journal of experimental Botany* **62**, 3171 (2011).

Acknowledgments: We thank Candace Major at NSF and the many researchers who contributed advice and enthusiasm for this project over the years. We are grateful to the staff at NCEI for facilitating curation of the paleo-CO_2 database, and to LDEO, the UCLA Lake Arrowhead Lodge and the Lady Bird Johnson Wildflower Center for hosting the three workshops that framed this work. Editor Jesse Smith and two anonymous reviewers provided valuable comments that improved this manuscript. This study is dedicated to Wally Broecker and Taro Takahashi, who pioneered the study of CO_2 dynamics in a changing climate.

Funding:

National Science Foundation grant OCE 16-36005 (BH, PJP)
Heising-Simons Foundation 2018-0996 (BH, VF)
National Science Foundation grant EAR 21-21649 (BH, VF, JM, CG)
National Science Foundation grant EAR 21-21170 (GJB)
National Science Foundation grant EAR 20-02370 (YC)
National Science Foundation grant 18-43285 (AP)
Columbia University's Center for Climate and Life (KTU)
G. Unger Vetlesen Foundation (KTU)
National Science Foundation grant 21-00537 (AP, PJP)
National Science Foundation grant 21-00509 (PJP)
National Science Foundation grant EAR 21-21165 (AR)
National Science Foundation grant EAR 18-06015 (YGZ)
National Science Foundation grant DGE 16-44869 (SRP)
National Science Foundation grant 18-13703 (EGH)
National Science Foundation grant OCE 16-58023 (JCZ)
National Science Foundation grant 16-02905 (MH)
Swedish Research Council grant NT7-2016 04905 (MS)
European Research Council grant 101020824 (JCM)
SFI/RC/2092 (JCM)
UK Research and Innovation grant 101045371 (MJH)
Natural Environment Research Council grant NE/X000567/1 (MPSB)
Royal Society grant DHF\R1\221014 (CRW)
Australian Research Council grant DP150104007 (PJF)
Deutsche Forschungsgemeinschaft grant RA 2068/4-1 (MR)
European Research Council grant 805246 (JWBR)
ETH Fellowship (JKCR)
National Science Foundation of China grant 42030503 (JD)
The Sandal Society Museum (GR)
Royal Society Tata Fellowship (BDAN)
Natural Environment Research Council grant NE/P019048/1 (GLF)

Author contributions:

Conceptualization: BH, GJB, DOB, MJH, MJK, AP, PJP, SRP, AR, DLR, MS, RSB, PJF, MH, MFS, JKCR, NDS, YGZ

Data Curation: BH, GJB, DOB, YC, MJH, MJK, JCM, PJP, DLR, MS, SRP, EA, MPSB, RSB, TBC, EdlV, KAD, CFG, MG, DTH, LLH, TKL, MG, JNM, MHS, RW, AR-N, NDS, SS, CRW, YGZ, JMC, DJ, DDE, GLF, EGH, BDAN, JBWR, MR, GJR, OS, LZ, CTB

Formal Analysis: BH, GJB, DOB, CY, MJH, PJP, DLR, AM, CEL

Investigation: BH, DLR, DOB, PJP, SRP, GJB, MJH, YC, MS, JCM, MJK, AP, EA, MPSB, RSB, PJF, WK, TKL, MFS, YGZ,

Software: GJB, VF, JJM, RW

Visualization: BH, GJB, MJH, MS, JCM, KTU, PJP, DOB, JA, BAK, CRS, JJM, RW

Funding acquisition: BH, PP, DLR, DOB, GJB, MJK, AP, RMdC, MH, KES, VF

Project administration: BH, DLR, DOB, PJP, GJB

Writing – original draft: BH, DLR, DOB, PJP, GJB, MJH, YC, MS, JCM, MJK, AP, KTU, AR, SRP

Writing – review & editing: all

Competing interests: None.

Data and materials availability: The completed data sheets for each study can be accessed as the paleo-CO_2 'Archive' at NOAA's National Center for Environmental Information (NCEI). The specific choice of category, as well as the updated CO_2 and age estimates, are documented in 'Product' sheets for each data set and proxy. In contrast to the 'Archive', which will grow with new publications but will otherwise remain passive, the paleo-CO_2 'Product' is a living database that will be updated when newly published data or ancillary data constraints become available, and/or methodological improvements are developed that enable modernization of previously underconstrained datasets. The 'Product' sheets created for this study can be accessed in NCEI (link to be inserted after acceptance for publication), and this is also the place where future data updates will be made available in consecutive versions of the data 'Product'.

Authors composing the Consortium:

Bärbel Hönisch[1*], Dana L. Royer[2*], Daniel O. Breecker[3*], Pratigya J. Polissar[4*], Gabriel J. Bowen[5*], Michael J. Henehan[6], Ying Cui[7], Margret Steinthorsdottir[8], Jennifer C. McElwain[9], Matthew J. Kohn[10], Ann Pearson[11], Samuel R. Phelps[12], Kevin T. Uno[1], Andy Ridgwell[13*], Eleni Anagnostou[14], Jacqueline Austermann[1], Marcus P. S. Badger[15], Richard S. Barclay[16], Peter K. Bijl[17], Thomas B. Chalk[18], Christopher R. Scotese[19], Elwyn de la Vega[20], Robert M. DeConto[21], Kelsey A. Dyez[22], Vicki Ferrini[1], Peter J. Franks[23], Claudia F. Giulivi[1], Marcus Gutjahr[14], Dustin T. Harper[5], Laura L. Haynes[24], Matthew Huber[25], Kathryn E. Snell[26], Benjamin A. Keisling[27], Wilfried Konrad[28], Tim K. Lowenstein[29], Alberto Malinverno[1], Maxence Guillermic[30], Luz María Mejía[31], Joseph N. Milligan[16], John J. Morton[1], Lee Nordt[32], Ross Whiteford[33], Anita Roth-Nebelsick[34], Jeremy K. C. Rugenstein[35], Morgan F. Schaller[36], Nathan D. Sheldon[22], Sindia Sosdian[37], Elise B. Wilkes[38], Caitlyn R. Witkowski[6], Yi Ge Zhang[39], Lloyd Anderson[1], David J. Beerling[40], Clara Bolton[18], Thure E. Cerling[5], Jennifer M. Cotton[41], Jiawei Da[3], Douglas D. Ekart[42], Gavin L. Foster[43], David R. Greenwood[44], Ethan G. Hyland[45], Elliot A. Jagniecki[46], John P. Jasper[47], Jennifer B. Kowalczyk[48], Lutz Kunzmann[49], Wolfram M. Kürschner[50], Charles E. Lawrence[48], Caroline H. Lear[37], Miguel A. Martínez-Botí[51], Daniel P. Maxbauer[52], Paolo Montagna[53], B. David A. Naafs[6], James W. B. Rae[33], Markus Raitzsch[54], Gregory J. Retallack[55], Simon J. Ring[56], Osamu Seki[57], Julio Sepúlveda[26], Ashish Sinha[58], Tekie F. Tesfamichael[59], Aradhna Tripati[30], Johan van der Burgh[60], Jimin Yu[61], James C. Zachos[62], Laiming Zhang[63]

Affiliations:

*Corresponding authors. Email: hoenisch@ldeo.columbia.edu, droyer@wesleyan.edu, breecker@jsg.utexas.edu, gabe.bowen@utah.edu, polissar@ucsc.edu, andy@seao2.org

[1] Lamont-Doherty Earth Observatory of Columbia University, Palisades, United States
[2] Wesleyan University, Middletown, United States
[3] The University of Texas at Austin, Austin, United States
[4] University of California Santa Cruz, Santa Cruz, United States
[5] University of Utah, Salt Lake City, United States
[6] University of Bristol, Bristol, United Kingdom
[7] Montclair State University, Montclair, United States
[8] Swedish Museum of Natural History, Stockholm, Sweden
[9] Trinity College Dublin, Dublin, Ireland
[10] Boise State University, Boise, United States
[11] Harvard University, Cambridge, United States
[12] CIM Group, New York, United States
[13] University of California Riverside, Riverside, United States
[14] GEOMAR Helmholtz-Zentrum für Ozeanforschung Kiel, Germany
[15] The Open University, Milton Keynes, United Kingdom
[16] Smithsonian Institution, Washington, DC, United States
[17] Utrecht University, Utrecht, Netherlands
[18] Aix Marseille University, CNRS, IRD, INRAE, CEREGE, Aix-en-Provence, France
[19] Northwestern University, Evanston, United States
[20] University of Galway, Galway, Ireland
[21] University of Massachusetts, Amherst, United States
[22] University of Michigan, Ann Harbor, United States
[23] The University of Sydney, Sydney, Australia
[24] Vassar College, Poughkeepsie, United States
[56] Purdue University, West Lafayette, United States
[26] University of Colorado Boulder, Boulder, United States
[27] University of Texas Institute for Geophysics, Austin, United States
[28] University of Tübingen, Tübingen, Germany
[29] Binghamton University, Binghamton, United States
[30] University of California Los Angeles, Los Angeles, United States
[31] MARUM, University of Bremen, Bremen, Germany
[32] Baylor University, Waco, United States
[33] University of St Andrews, St Andrews, United Kingdom
[34] State Museum of Natural History, Stuttgart, Germany
[35] Colorado State University, Fort Collins, United States
[36] Rensselaer Polytechnic Institute, Troy, United States
[37] Cardiff University, Cardiff, United Kingdom
[38] Ginkgo Bioworks, Boston, United States
[39] Texas A&M University, College Station, United States
[40] University of Sheffield, Sheffield, United Kingdom
[41] California State University Northridge, Northridge, United States
[42] n/a, Salt Lake City, United States

[43] *University of Southampton, Southampton, United Kingdom*
[45] *Department of Biology, Brandon University, Brandon, Canada*
[45] *North Carolina State University, Raleigh, United States*
[46] *Utah Geological Survey, Salt Lake City, United States*
[47] *Molecular Isotope Technologies, LLC, Niantic, United States*
[48] *Brown University, Providence, United States*
[49] *Senckenberg Natural History Collections, Dresden, Germany*
[50] *University of Oslo, Oslo, Norway*
[51] *EIT Urban Mobility, Barcelona, Spain*
[52] *Carleton College, Northfield, United States*
[53] *Institute of Polar Sciences - National Research Council, Bologna, Italy*
[54] *Dettmer Group KG, Bremen, Germany*
[55] *University of Oregon, Eugene, United States*
[56] *Deutsches GeoForschungsZentrum GFZ, Potsdsam, Germany*
[57] *Hokkaido University, Sapporo, Japan*
[58] *California State University Dominguez Hills, Carson, United States*
[59] *Addis Ababa University, Addis Ababa, Ethiopia*
[60] *n/a, Rossum, The Netherlands*
[61] *Laoshan Laboratory, Qingdao, China*
[62] *University of California Santa Cruz, Santa Cruz, United States*
[63] *China University of Geosciences, Beijing, China*

List of Supplementary Materials

Supplementary Text, Sections 1-10, Figs. S1 to S13

Tables S1 to S3

References (*118-439*)

Figures :

Fig. 1. Documentation and assessment of all Cenozoic paleo-CO_2 estimates published to date. Individual proxy estimates are defined by colored symbols in legends. **(a)** Vetted Category 1 estimates with their fully developed uncertainty estimates (95% CIs); age uncertainties have been updated or established to the best of current understanding. **(b)** Vetted Category 2 estimates whose uncertainty is not yet fully constrained. Category 1 data are shown in grey for reference. **(c)** Archive compilation of all CO_2 estimates in their originally published quantification. To toggle view of individual proxy records in panels (a) and (c), please go to paleo-co2.org (Note: panel (a) visualization will be published on the website after acceptance of the manuscript for publication).

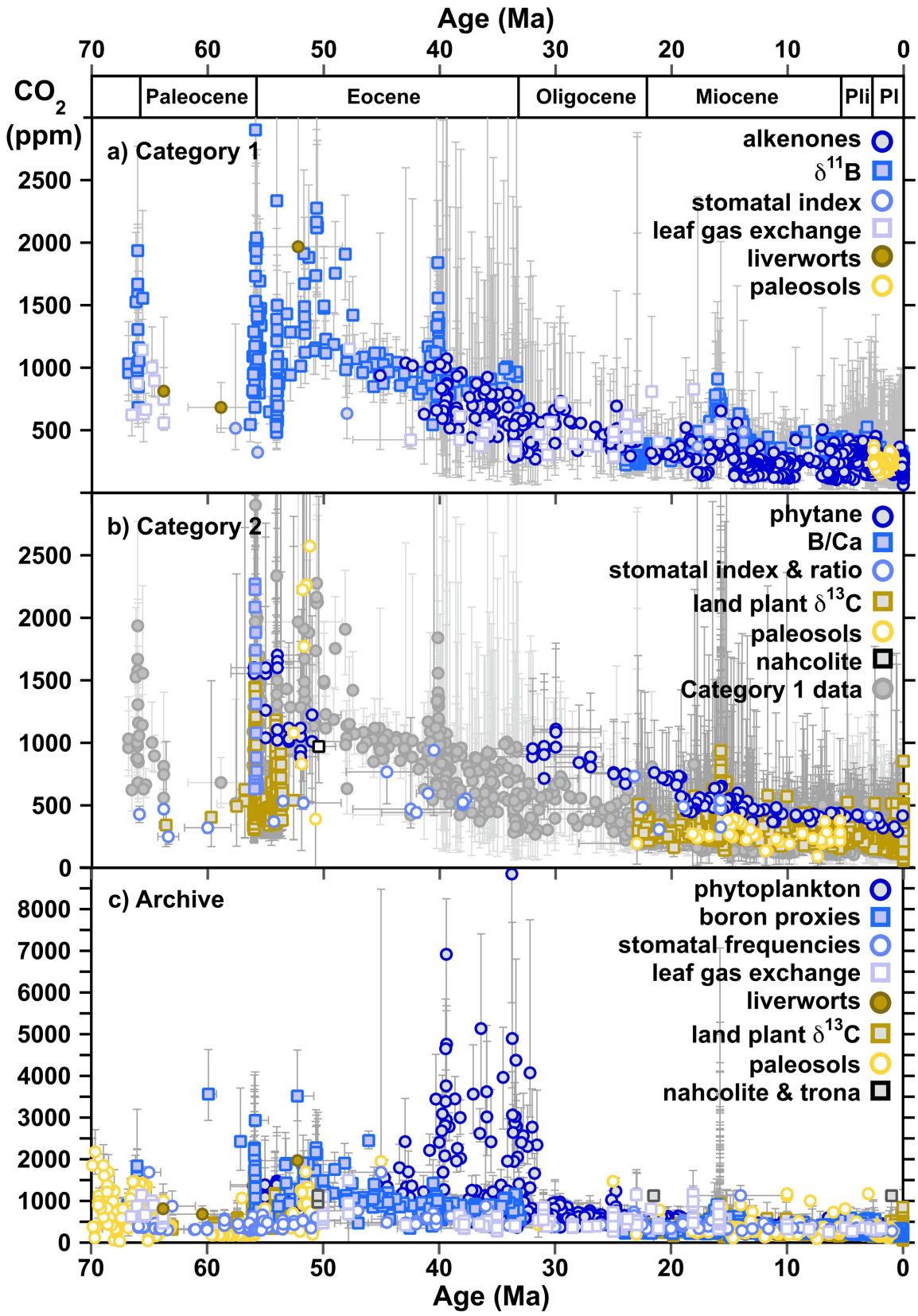
Age (Ma)
70
60
50
40
30
20
10
0
CO2 (ppm)
Paleocene
Eocene
Oligocene
Miocene
Pli
Pl
a) Category 1
alkenones
δ11B
stomatal index
leaf gas exchange
liverworts
paleosols
2500
2000
1500
1000
500
b) Category 2
phytane
B/Ca
stomatal index & ratio
land plant δ13C
paleosols
nahcolite
Category 1 data
2500
2000
1500
1000
500
0
c) Archive
phytoplankton
boron proxies
stomatal frequencies
leaf gas exchange
liverworts
land plant δ13C
paleosols
nahcolite & trona
8000
7000
6000
5000
4000
3000
2000
1000
0
70
60
50
40
30
20
10
0
Age (Ma)

840

Fig. 2. Category 1 paleo-CO_2 record compared to global climate signals. The vertical dashed line indicates the onset of continent-wide glaciation in Antarctica. **(a)** Atmospheric CO_2 estimates (symbols) and 500-kyr mean statistical reconstructions (median and 50 and 95% credible intervals - dark and light-blue shading, respectively). Major climate events are highlighted (K-PG - Cretaceous/Paleogene boundary, PETM - Paleocene Eocene Thermal Maximum, EECO - Early Eocene Climatic Optimum, MECO - Middle Eocene Climatic Optimum, EOT - Eocene/Oligocene Transition, MCO - Miocene Climatic Optimum, NHG - onset of Northern Hemisphere Glaciation, MPT - Mid Pleistocene Transition). The 2022 annual average atmospheric CO_2 of 419 ppm is indicated for reference. **(b)** Global mean surface temperatures estimated from benthic $\delta^{18}O$ data after Westerhold et al. (*43*) (solid line, individual proxy estimates as symbols, and statistically reconstructed 500-kyr mean values shown as the continuous curve, with 50 and 95% credible intervals) and from surface temperature proxies (*45*) (grey boxes). **(c)** Sea level after Ref. (*66*) with gray dots displaying raw data; the solid black line reflects median sea level in a 1-Myr running window. High- and lowstands are defined within a running 400-kyr window, with lower and upper bounds of highstands defined by the 75th and 95th percentiles, and lower and upper bounds of lowstands defined by the 5th and 25th percentiles in each window. Globes depict select paleogeographic reconstructions and the growing presence of ice sheets in polar latitudes from Ref. (*116*). **(d)** Crown ages show C_4 clades, with CCMs adapted to low CO_2, initially diversified in the early Miocene and then rapidly radiated in the late Miocene (*117*). Flora transition from dominantly forested and woodland to open grassland habitats based on fossil phytolith abundance data (*96*). North American equids typify hoofed animal adaptations to new diet and environment (*103*), including increasing tooth mesowear (black line, note inverted scale), hypsodonty (blue line), and body size.

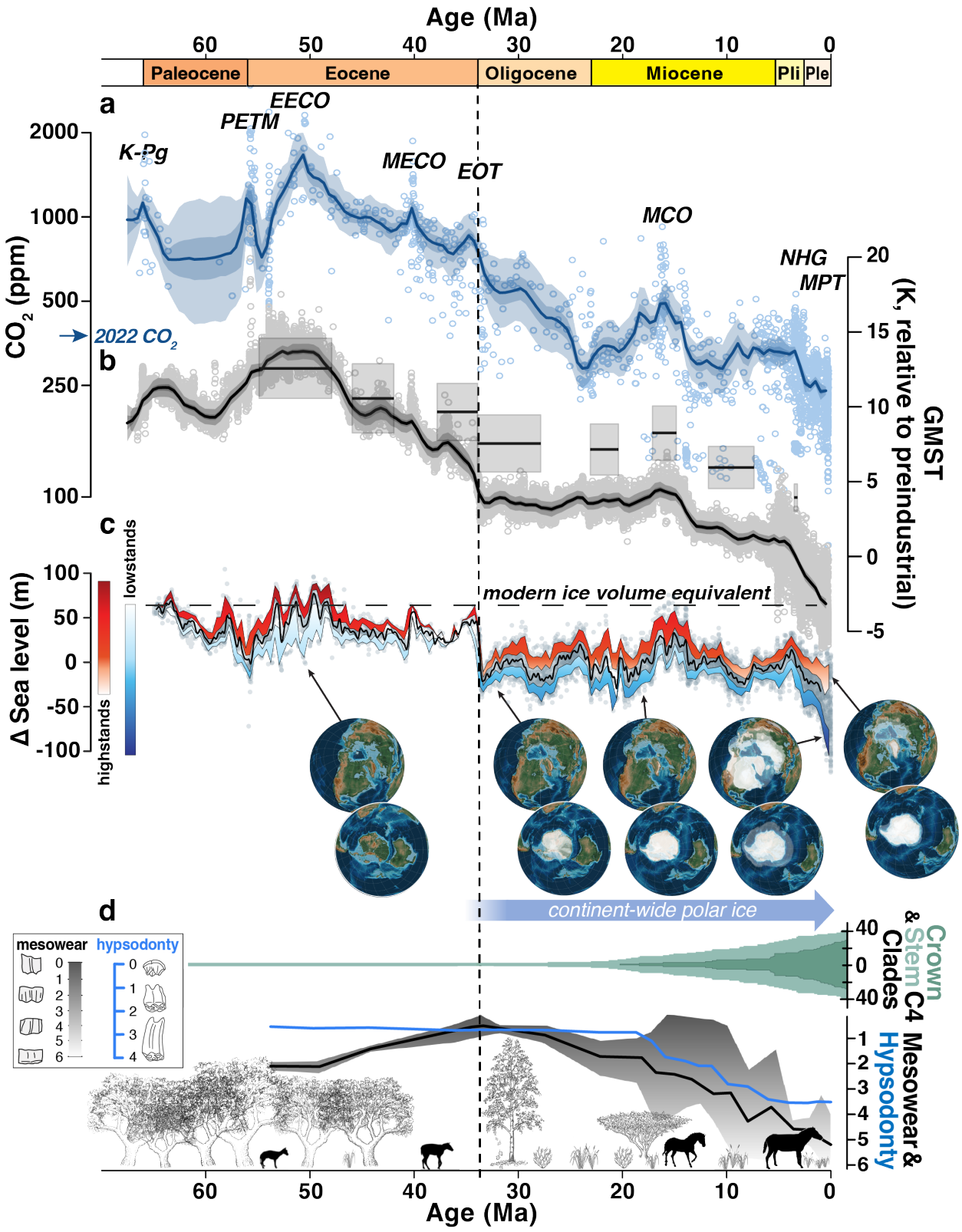
Age (Ma)
60
50
40
30
20
10
0
Paleocene
Eocene
Oligocene
Miocene
Pli
Ple
a
EECO
PETM
K-Pg
MECO
EOT
MCO
NHG
MPT
2000
1000
500
250
100
CO2 (ppm)
2022 CO2
b
20
15
10
5
0
-5
GMST
(K, relative to preindustrial)
c
100
50
0
-50
-100
Δ Sea level (m)
highstands
lowstands
modern ice volume equivalent
continent-wide polar ice
d
mesowear
hypsodonty
0
1
2
3
4
5
6
40
0
-40
Crown & Stem C4 Clades
1
2
3
4
5
6
Mesowear & Hypsodonty
60
50
40
30
20
10
0
Age (Ma)

Fig. 3. Application of the Category 1 CO_2 record to determine $ESS_{[CO2]}$. GMST deviation (K) from preindustrial global average surface temperature of 14.15°C is displayed versus paleo-CO_2 doublings relative to the preindustrial baseline of 280 ppm (upper x-axis) and paleo-CO_2 estimates on a log scale (lower x-axis). The slopes between two points in time reflect the average $ESS_{[CO2]}$. Circles reflect 500-kyr binned 'Category 1' CO_2 estimates paired with corresponding GMST-means from Ref. (*43*), squares pair CO_2 and GMST means from compilations of sea surface temperature (*45*) in seven coarsely resolved time intervals. Note that this figure omits the Pliocene temperature estimate of (*45*) because it samples too short a time interval (cf. Fig. 2) to be comparable with mean CO_2. Data from Cenozoic epochs are color coded and shift from red (Paleocene) to yellow (Pleistocene); labels indicate specific age bins (Ma). Dashed lines indicate reference $ESS_{[CO2]}$ lines of 8 and 5°C warming per doubling of CO_2.

880

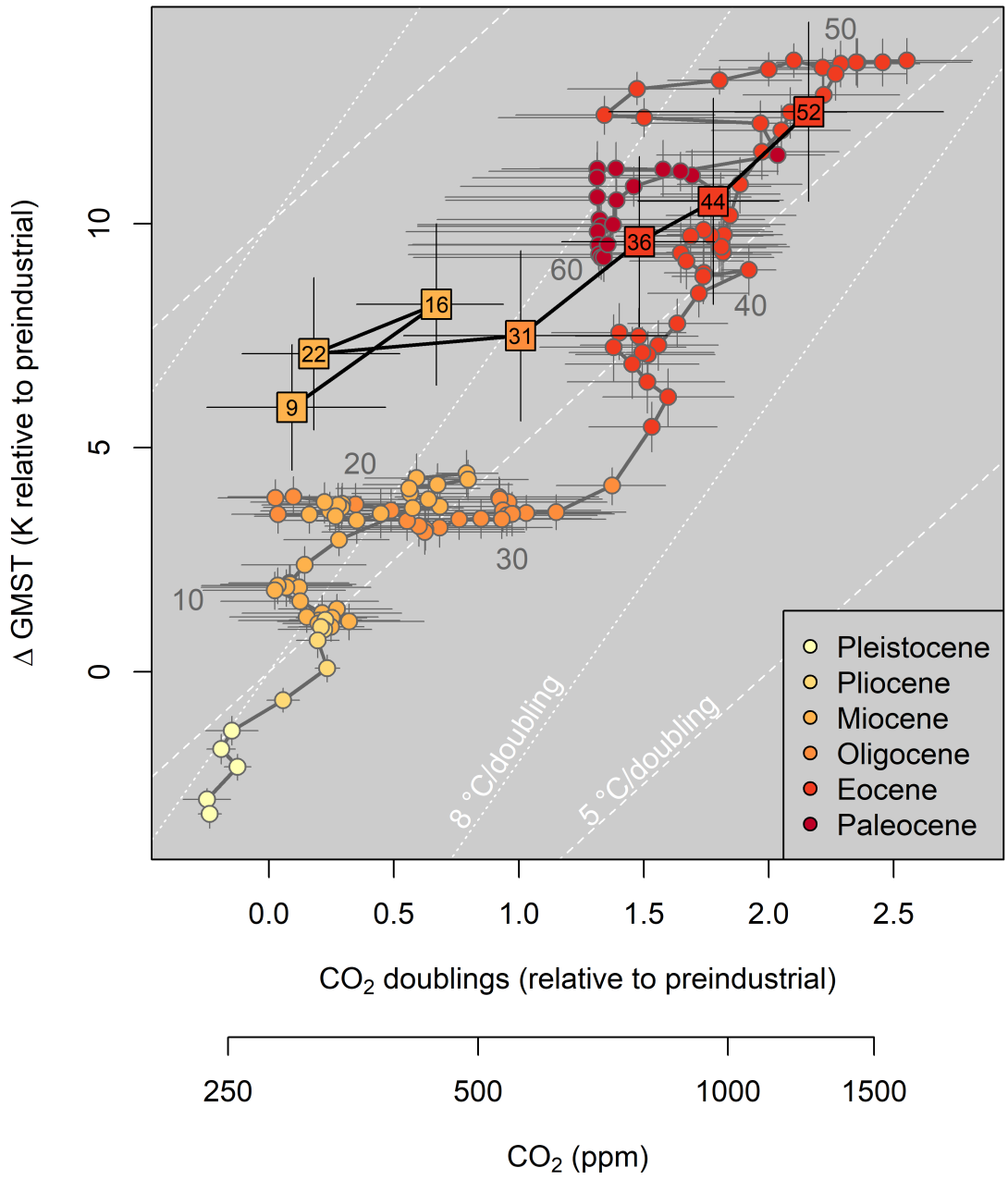
Δ GMST (K relative to preindustrial)
0
5
10
0.0
0.5
1.0
1.5
2.0
2.5
CO2 doublings (relative to preindustrial)
250
500
1000
1500
CO2 (ppm)
9
22
16
31
36
44
52
10
20
30
40
50
60
8 °C/doubling
5 °C/doubling
Pleistocene
Pliocene
Miocene
Oligocene
Eocene
Paleocene

881

Science
AAAS

Supplementary Materials for

Towards a Cenozoic History of Atmospheric CO_2

by the

Cenozoic CO_2 Proxy Integration Project ($CenCO_2PIP$) Consortium:

Bärbel Hönisch[1*], Dana L. Royer[2*], Daniel O. Breecker[3*], Pratigya J. Polissar[4*], Gabriel J. Bowen[5*], Michael J. Henehan[6], Ying Cui[7], Margret Steinthorsdottir[8], Jennifer C. McElwain[9], Matthew J. Kohn[10], Ann Pearson[11], Samuel R. Phelps[12], Kevin T. Uno[1], Andy Ridgwell[13*], Eleni Anagnostou[14], Jacqueline Austermann[1], Marcus P. S. Badger[15], Richard S. Barclay[16], Peter K. Bijl[17], Thomas B. Chalk[18], Christopher R. Scotese[19], Elwyn de la Vega[20], Robert M. DeConto[21], Kelsey A. Dyez[22], Vicki Ferrini[1], Peter J. Franks[23], Claudia F. Giulivi[1], Marcus Gutjahr[14], Dustin T. Harper[5], Laura L. Haynes[24], Matthew Huber[25], Kathryn E. Snell[26], Benjamin A. Keisling[27], Wilfried Konrad[28], Tim K. Lowenstein[29], Alberto Malinverno[1], Maxence Guillermic[30], Luz María Mejía[31], Joseph N. Milligan[16], John J. Morton[1], Lee Nordt[32], Ross Whiteford[33], Anita Roth-Nebelsick[34], Jeremy K. C. Rugenstein[35], Morgan F. Schaller[36], Nathan D. Sheldon[22], Sindia Sosdian[37], Elise B. Wilkes[38], Caitlyn R. Witkowski[6], Yi Ge Zhang[39], Lloyd Anderson[1], David J. Beerling[40], Clara Bolton[18], Thure E. Cerling[5], Jennifer M. Cotton[41], Jiawei Da[3], Douglas D. Ekart[42], Gavin L. Foster[43], David R. Greenwood[44], Ethan G. Hyland[45], Elliot A. Jagniecki[46], John P. Jasper[47], Jennifer B. Kowalczyk[48], Lutz Kunzmann[49], Wolfram M. Kürschner[50], Charles E. Lawrence[48], Caroline H. Lear[37], Miguel A. Martínez-Botí[51], Daniel P. Maxbauer[52], Paolo Montagna[53], B. David A. Naafs[6], James W. B. Rae[33], Markus Raitzsch[54], Gregory J. Retallack[55], Simon J. Ring[56], Osamu Seki[57], Julio Sepúlveda[26], Ashish Sinha[58], Tekie F. Tesfamichael[59], Aradhna Tripati[30], Johan van der Burgh[60], Jimin Yu[61], James C. Zachos[62], Laiming Zhang[63]

Corresponding authors: hoenisch@ldeo.columbia.edu, droyer@wesleyan.edu, breecker@jsg.utexas.edu, gabe.bowen@utah.edu, polissar@ucsc.edu, andy@seao2.org

This PDF file includes:

Supplementary Text Figs. S1 to S12
Tables S1 to S3
References (118-439)

Supplementary Text

This supplementary information details the procedures reported in the main text. Sections 1-8 provide the current understanding of each paleo-CO_2 proxy, the criteria for vetting, categorizing and revising individual records, and future directions for further proxy validation and improvement. Of these, Section 1 is the most detailed because the theory behind the phytoplankton proxy is currently being re-evaluated. Section 9 describes the approximation of age uncertainties assigned to marine paleo-CO_2 estimates. Section 10 describes the model for estimating the joint evolution of Cenozoic CO_2 as constrained by the compiled Category 1 proxy data, including alternative scenarios calculated at 100-kyr and 1-Myr resolution. This section also includes a figure displaying the number of data and proxies included in each 500-kyr timestep, an assessment of the last time CO_2 was as high as today, and a comparison of our results with a previous estimate by Hansen et al. (*44*). Table S1 summarizes the vetting criteria for classifying each proxy into data categories 1, 2, or 3. The specific categorization criteria for individual records and data points are reported in the product data sheets for each record, which are archived in NCDC. Table S2 provides an index to guide the reader to details for each proxy, as described in Sections 1-8. Table S3 provides the age uncertainty estimates assigned to those marine records that were published without such estimates.

1. Phytoplankton

1.1. Current understanding of the phytoplankton proxy and recent advances

Reconstructing paleo-CO_2 from carbon isotope ratios in algal organic matter is based on the difference in $^{13}C/^{12}C$ isotope ratios between aqueous CO_2 and the organic products of photosynthesis (*118-120*). In both laboratory cultures (e.g., *121*) and open marine settings (*122, 123*), the magnitude of phytoplanktic isotope fractionation (ε_p) is positively correlated to the ambient [$CO_{2(aq)}$]. The predominantly invoked explanation describes this relationship based on principles of diffusive supply and demand: as [$CO_{2(aq)}$] increases, so too does the diffusive influx of CO_2. This results in less complete CO_2 utilization by the organism and allows more discrimination between the two carbon isotopes (*124, 125*). Thus, ε_p is large when $CO_{2,atm}$ and [$CO_{2(aq)}$] are high, and ε_p is small when $CO_{2,atm}$ and [$CO_{2(aq)}$] are low; this general relationship is used for paleobarometry not only in the Cenozoic (e.g., *126*), but throughout the Phanerozoic (*127*).

The mechanism behind variation in ε_p is believed to lie with kinetic rate differences between the transport and fixation of $^{13}CO_2$ vs. $^{12}CO_2$ during irreversible step(s) of the net photosynthetic process. The CO_2-fixing enzyme ribulose 1,5-bisphosphate carboxylase/oxygenase (RuBisCO) in plants and algae preferentially utilizes $^{12}CO_2$, yielding a primary photosynthate that is 11-30‰ depleted in ^{13}C relative to the CO_2 supply (*128-132*). In addition to [$CO_{2(aq)}$] and the effect of RuBisCO, algal culture experiments have identified other factors that contribute to the net expression of ε_p. These variables include growth rate, cell size and geometry, species, growth conditions such as nutrient or light limitation, and potentially the expression of carbon concentrating mechanisms (CCMs) (*121, 133-136*).

Because algal species vary across many of the above parameters, the community has traditionally tried to reduce this variability by focusing on biomarkers with well-constrained biological sources, such as alkenones, which are produced exclusively by coccolithophorid algae belonging to the order Isochrysidales (clade Haptophyta). These are the organisms also utilized for the $U_{37}^{K'}$ alkenone paleotemperature index (e.g., *137*). Other than the datasets of Witkowski et al. (*127*) and Mejía et al. (*138*), which use the generic compound phytane and diatom-bound organic carbon, respectively, all phytoplankton data in the present compilation represent alkenone $\varepsilon_p$values. Return to **Table S2**.

1.2. Details of theory

1.2.1. Method 1 - Traditional Framework

The photosynthetic fractionation of carbon isotopes, ε_p, is calculated from estimates of the $\delta^{13}C$ values of CO_2 and biomass (Eq. 1.1):

$$\varepsilon_p = \left[\frac{\delta^{13}C_{CO_2(aq)}+1000}{\delta^{13}C_{biomass}+1000} - 1\right] \cdot 1000 \cong \delta^{13}C_{CO_2(aq)} - \delta^{13}C_{biomass} \quad \text{(Eq. 1.1)}$$

The former are reconstructed from sedimentary carbonates (such as planktic foraminifera) and estimates of local sea-surface temperature, while the latter are from biomarkers corrected for biosynthetic offsets from bulk cellular biomass $\delta^{13}C$. For more details, see section 1.4.

The classical framework for using alkenone-derived ε_p values to reconstruct atmospheric CO_2 (*139, 140*) assumes that ε_p changes in an inverse linear relationship to the ratio of carbon demand to $[CO_{2(aq)}]$:

$$\varepsilon_p = \varepsilon_f - \frac{b}{[CO_{2(aq)}]} \quad \text{(Eq. 1.2)}$$

Here, ε_f is assumed to be the maximum expressed fractionation by RuBisCO at the limit of infinite CO_2 (generally taken as 25 to 28‰). The b term represents all non-$[CO_{2(aq)}]$ effects on ε_p, including growth rate and all other biological controls on carbon demand. This relationship has been the basis for paleo-CO_2 reconstructions from alkenones (e.g., *141*) and other algal biomarkers such as chlorophyll and its degradation products (*119, 120*), phytane and phytol (cf. *127*), and the C_{17} *n*-alkane (e.g., *142*). Atmospheric pCO_2 is calculated using the temperature and salinity-adjusted Henry's law constant, K_H (*143*).

Equation 1.2 requires an input value for the parameter b. The conventional strategy to determine b for a given location uses empirical calibrations of modern samples that show a linear correlation between b and *in-situ* surface ocean $[PO_4^{3-}]$. The value of b is calculated using measured ε_p and $[CO_{2(aq)}]$ data for modern phytoplankton samples and/or core-tops, and then is correlated with measurements or best estimates for the local PO_4^{3-} concentrations in the photic zone:

$$b = \left(\varepsilon_f - \varepsilon_p\right)\left[CO_{2(aq)}\right];\ b \text{ plotted vs. } [PO_4^{3-}] \text{ to yield } b = A + B[PO_4] \quad \text{(Eq. 1.3)}$$

For paleobarometry applications, the modern or modeled $[PO_4^{3-}]$ in surface waters overlying the core location (often back-projected to its paleo latitude/longitude) is used in Eq. 1.3, enabling calculation of a single location-specific b value to plug into Eq. 1.2. Various solutions for the calibration parameters A and B have been proposed. Historically, most applications have used $b = 119\left[PO_4^{3-}\right] + 84$ (*126*). Here we use a recently updated compilation (*144*), filtered to include only photic zone samples from the water column (Figure S1, $b = 130[PO_4^{3-}] + 93$). Sediment core-top values were not used due to uncertainties in the age and duration over which these sediments accumulated and therefore corresponding difficulty in assigning their appropriate $[CO_{2(aq)}]$ and $[PO_4^{3-}]$ reference values. This approach is hereafter called Method 1, or the "traditional b" method. More recently, several modified approaches have been developed to account for some of the underlying physiological complexity encompassed by the parameter b. These revised schemes are elaborated in sections 1.2.2-1.2.4, where they are called Methods 2, 3, and 4.

<u>Factors underlying the b parameter.</u> A theoretical model by Rau et al. (*145*) proposed a formal description of the physiological parameters underlying ε_p. In this framework, the fractionation is related to the cellular carbon budget, τ (adapted from *146*), which is defined by the ratio of carbon demand to diffusive CO_2 supply (both mol C s^{-1}) (Eq. 1.4).

$$\tau = \frac{\text{C demand}}{\text{C supply}} = \frac{V \cdot [C_{cell}] \cdot \mu_i}{SA \cdot P_C \cdot [CO_{2(aq)}]} \quad \text{(Eq. 1.4)}$$

This implies τ is a unitless ratio, where V is cell volume (m^3), $[C_{cell}]$ is the organic carbon density of the cell (mol C m^{-3}), μ_i (seconds^{-1}) is the photoperiod-normalized (also termed instantaneous) growth rate (per second, *134*), SA is the surface area (m^2), P_C is the permeability of the cell

membrane to diffusion of aqueous CO_2 (m s^{-1}), and $CO_{2(aq)}$ is in units of mol m^{-3}; thus the numerator and denominator are each mol C s^{-1}. Note that some versions of Eq. 1.4 replace $V \cdot [C_{cell}]$ with POC (particulate organic carbon, mol C $cell^{-1}$).

Expression in this form easily shows how ε_p is a function of the relative degree of carbon utilization (τ) and the isotope effects of diffusive transport (ε_t) and carbon fixation (ε_f):

$$\varepsilon_p = \varepsilon_f - (\varepsilon_f - \varepsilon_t)\tau \quad \text{(Eq. 1.5)}$$

Since ε_t is nearly zero in aqueous systems (*147*), when C demand and supply are equal (τ approaching 1), ε_p approaches zero. Conversely, decreases in C demand or increases in C supply (lower τ) increase ε_p. Thus, b accounts for all the physiological (i.e., non-$[CO_{2(aq)}]$ components of τ:

$$b = (\varepsilon_f - \varepsilon_t)\left[CO_{2(aq)}\right]\tau = (\varepsilon_f - \varepsilon_t)\frac{V \cdot [C_{cell}] \cdot \mu_i}{SA \cdot P_C} \quad \text{(Eq. 1.6)}$$

The implications of understanding b as a shorthand for net cellular properties include the realization that cell geometry significantly impacts the expression of ε_p (*145, 148*). Traditional alkenone biomarker paleo-CO_2 reconstructions reduce this complexity due to the spherical geometry of Isochrysidales, but do not completely account for the changing V:SA ratios that accompany changes in cell size.

Several recent studies discuss the relative importance of incorporating these additional physiological parameters (*39-41, 138, 144, 149-152*). The proposed modifications fall into two categories: (i) modulating b using size-scaling and growth rate relationships, or (ii), empirical approaches based upon the response of ε_p to $[CO_{2(aq)}]$ observed in laboratory cultures. Return to **Table S2**.

1.2.2. Method 2 - size correction

The first major correction developed for the diffusive *b* model was based on the recognition that coccolith length scales with cell radius (Figure S2) (*38*).

This relationship was then applied to sedimentary alkenone paleo-CO_2 records using co-occurring fossil coccoliths to adjust the value of b (Eq. 1.7) according to the V:SA ratio for cells of the corresponding predicted radius (*153*):

$$b' = b\left[\frac{V/SA_{fossil}}{V/SA_{modern}}\right] \quad \text{(Eq. 1.7)}$$

This approach and the Method 3 strategy (below) both start with the standard definition of b and calculate a multiplier to account for changes in algal community properties. As such, Eq. 1.7 assumes that $[C_{cell}]$ and P_C remain constant so that past changes in V/SA capture changes in carbon demand and diffusive supply solely due to cell geometry.

1.2.3. Method 3- size and growth rate corrections

Modifications to b also have been adapted to account for estimated changes in growth rate (cf. *149, 154, 155*). These studies assume that changing physiological forms also indicate changes in cell-specific growth rates, with growth rate inferred from changes in paleo-productivity or nutrient proxies (*149, 156*). Alternatively, estimates of past phosphate concentrations are used

to calculate a variable *b* parameter with the relationship shown in Figure S1 (cf. *140, 155*). The b value is adjusted for changes in growth rate similarly to cell size:

$$b' = b\left[\frac{\mu_{\mathrm{i,fossil}}}{\mu_{\mathrm{i,modern}}}\right] \quad \text{(Eq.1.8)}$$

More recently, Zhang et al. (*41*) developed an approach that combines the geometric correction (Eq. 1.7) with the principles of the growth-rate correction (Eq. 1.8). This approach, here called Method 3, uses the cell size both to adjust for V:SA (diffusion dependence on geometry), and also to directly estimate the growth rate. The components of *b* that represent the term $\left[CO_{2(aq)}\right]\tau$ come from the Rau et al. (*145*) model and are symbolized as the $CO_{2(aq)}$ uptake rate per unit cell surface area (Q_S), the temperature-dependent $CO_{2(aq)}$ diffusivity (D_T), the cell radius (r), reacto-diffusive length (r_k, the term r/r_k accounts for the relative contribution to the CO_2 flux by extracellular spontaneous conversion of HCO_3^- to CO_2), and permeability (P_C):

$$b = (\varepsilon_f - \varepsilon_t)Q_S\left(\frac{r}{D_T\left(1+\frac{r}{r_k}\right)} + \frac{1}{P_C}\right) \quad \text{(Eq. 1.9)}$$

The empirical relationship between coccolithophore cell volume (V) and instantaneous growth rate (μ_i) (Figure S3) was established using the data from 89 nutrient- and/or light-limited chemostat and semi-continuous diluted batch culture experiments as compiled by Aloisi (*157*). Cell size, surface area and volume are estimated by measuring the coccolith length, as above (Figure S2). The cellular carbon content (POC/cell) is estimated from cell volume and an empirical relationship of POC to cell volume (Eq. 3 of *41*):

$$POC\ (\mathrm{fmol\ C\ per\ cell}) = 14.6 * V(\mu m^3) \quad \text{(Eq. 1.10)}$$

The growth rate vs. size relationship (Figure S3, *41*) yields μ_i, which is then multiplied by POC and divided by the cell surface area to determine Q_S. The membrane permeability (P_C) was calculated from Pleistocene alkenone-producers ($5.09 \pm 0.16 \times 10^{-5}$ m s^{-1}) using ice core CO_2 and ε_p data from Pleistocene sediment samples at two sites, based on a boot-strap resampling technique (*41*). This value for P_C is broadly consistent with laboratory estimates of the permeability of *E. huxleyi* (*158*).

1.2.4. Method 4 – empirical relationships

Finally, two recent studies have taken an empirical approach, bypassing the Rau et al. (*145*) approach to defining the sub-components of τ (Eq. 1.4; i.e., the underlying terms of b), thereby allowing for the presence of non-diffusive or other modes of carbon uptake (including bicarbonate) and CCMs. Using data for *E. huxleyi* and *G. oceanica* in cultures, both Stoll et al. (*40*) and Phelps et al. (*39*) found a different sensitivity of ε_p to changes in $[CO_{2(aq)}]$ when compared to any version of the purely diffusive model (Methods 1-3). Rae et al. (*34*) used this new approach to produce a revised paleo-CO_2 record. They first calculate CO_2 anomalies over the Neogene, and then referenced these anomalies to samples from the late Pleistocene, where paleo-CO_2 is known from ice core measurements. In this approach, relative changes in $[CO_{2(aq)}]$ are calculated using the slope (m) of the statistical relationship between $\ln[CO_{2(aq)}]$ and ε_p, and the relative changes are anchored with Quaternary sediment samples from the same site where atmospheric CO_2

from ice-core records is known. For each Quaternary-aged sample, an offset value ($I_{sample,Quaternary}$) is calculated:

$$I_{sample,Quaternary} = \varepsilon_p - m * \ln([CO_2]_{aq}) \quad \text{(Eq. 1.11)}$$

where m equals 2.66 ± 0.42 (±1-sigma, *40*). The mean of these offset values for each site is then used as the Quaternary anchor ($I_{Quaternary}$) for that site. The aqueous CO_2 concentration is then calculated from ε_p and Eq. 1.11, substituting the mean Quaternary intercept and slope to find $[CO_{2(aq)}]$. This approach requires Quaternary samples that overlap the ice-core record and is thus limited to a few sites in the dataset. Return to **Table S2**.

1.2.5. Remaining challenges for understanding the systematics of algal carbon isotopes

The above approaches primarily focus on improving how relative cellular carbon demand (τ, and by extension, b) is estimated. As such, they presume (i) that the diffusive model is correct and complete, and (ii) that the isotope fractionation associated with carbon fixation (ε_f, i.e., the value inferred to result from RuBisCO) is well understood and can be set as a constant. However, recent advances in understanding algal physiology are challenging both premises (see following section), and new factors soon may be incorporated into further revisions of the algal paleobarometry model. These additional considerations are summarized briefly here, because Method 4 utilizes aspects of these additional physiological factors such as irradiance.

The C isotope effect of RuBisCO. Isotopic fractionation during algal carbon fixation, ε_f ($\approx$25‰, *121, 148*), originally was thought to be equivalent to the fractionation by RuBisCO, $\varepsilon_{RuBisCO}$, as is observed in land plants ($\approx$29‰, *159, 160*). However, experiments demonstrate that Form ID RuBisCO of modern marine phytoplankton has a significantly smaller value of $\varepsilon_{RuBisCO}$ ($\approx$11‰ in the coccolithophore *E. huxleyi* and $\approx$18‰ in the diatom *Skeletonema costatum*, *131, 132*). This finding is particularly problematic for alkenone paleobarometry, because it would set a maximum value of ≈11‰ for alkenone-derived ε_P (Eq. 1.2), despite observations of much larger values (20-24‰) in the early and mid-Cenozoic portions of the existing ε_P dataset. Values of ε_p greater than $\varepsilon_{RuBisCO}$ are not permitted by the existing diffusive-supply model framework. The implication is that additional fractionation processes are required to explain high values of ε_p, and ε_f cannot simply be presumed to equal $\varepsilon_{RuBisCO}$ (*161*).

Irradiance. The effects of varying the photosynthetic irradiance provide clues about a potential source of this additional isotopic fractionation. Laboratory experiments (e.g., *135*) and environmental data (summarized in *152*) show that irradiance influences ε_p beyond simply the increase in growth rate enabled by higher light levels. In laboratory experiments across several different algal groups, high and continuous (24 hour) irradiance appears necessary to generate large values of ε_p (*39, 40*) but to date, the specific conditions that yield high ε_p values in the sedimentary record remain unknown despite their apparently common occurrence during the Eocene and Oligocene.

Carbon-concentrating mechanisms (CCMs). A further unanswered question is the role of carbon-concentrating mechanisms (CCMs) in altering both carbon acquisition and CO_2 concentration at the site of fixation (e.g., *162*). CCMs can mimic a diffusive CO_2 source, in which case they can be treated as "diffusive-like". Recently, Badger (*107*) observed that CO_2 reconstructed from algal ε_p

values during Pleistocene glacial cycles was systematically in error only at sites where the aqueous CO_2 concentration was < 7 µmol L^{-1}. This observation could suggest that CCMs affect ε_p at low CO_2 levels, but that diffusion dominates at higher CO_2 levels, i.e., during the Cenozoic until the Plio-Pleistocene (*107*). Alternatively, from analysis of laboratory cultures, Stoll et al. (*40*), Wilkes and Pearson (*161*), and Phelps et al. (*39*) suggest CCMs are ubiquitously present and functional, but that they scale with a curvilinear relationship between ε_p and $1/[CO_{2(aq)}]$ or τ (*39, 162*). Return to **Table S2**.

1.3. Criteria for vetting phytoplankton proxy records

The data compiled for this study and database come from over 30 years of published research, with varied approaches to constraining the necessary biological, geochemical, and environmental parameters needed to reconstruct past atmospheric CO_2 (*41, 108, 118, 126, 127, 138, 140, 141, 149-151, 154-156, 163-172*). These data were classified into three categories based upon the data completeness and several other criteria. 'Category 1' data are CO_2 estimates of high quality whose sources of uncertainty are fully developed. 'Category 2' data encompass estimates of high quality, but their sources of uncertainty are not yet fully constrained. 'Category 3' estimates are either superseded by newer evaluations of the same proxy data or are considered unreliable due to a variety of factors such as incomplete or outdated sample preparation and/or not fully quantifiable uncertainty estimation. The following criteria were used to categorize each phytoplankton data point in each study:

Category 1 – Fully quantified paleo-CO_2 estimates

A. All data needed to calculate paleo-CO_2 with modern methods are reported. We required the following data to be reported (or reporting of variables needed to calculate them): algal biomass $\delta^{13}C$ values, $\delta^{13}C$ values of aqueous CO_2 or DIC, and sea surface temperature (SST). Some additional variables are only needed for particular methods of calculating surface ocean pCO_2: $[PO_4^{3-}]$ and coccolith length (Method 2), coccolith length (Method 3), and Pleistocene samples from the same site for Quaternary anchoring (Method 4). If multiple values for a variable (e.g., SST from U^K_{37} and TEX_{86}) were reported, we used the original publication's choice of values, or averages of where the selection was ambiguous in the original publication (explained in the "notes" columns in data spreadsheets).

B. Known sources of error have been quantified and/or sensitivity of the paleo-CO_2 estimate to those sources is small.

Category 2 – Incompletely quantified paleo-CO_2 estimates

A. Samples include all of the data needed to quantify paleo-CO_2 but the aqueous CO_2 concentration falls outside the range used in calibrating empirical factors used in the estimation of paleo-CO_2. In Method 2, the range is from the minimum and maximum $[CO_2]_{aq}$ in the *b*-$[PO_4^{2-}]$ calibration dataset. In Method 4, the range is from the minimum and maximum $[CO_2]_{aq}$ values in the laboratory culture experiments that form the calibration dataset.

B. Samples/records where the organisms contributing to the algal carbon $\delta^{13}C$ value are unknown. This category includes samples where the $\delta^{13}C$ of algal organic matter is determined from biomarkers that lack taxonomic specificity (such as phytol and phytane).

Category 3 – Not used to estimate paleo-CO_2

A. Samples that are superseded by newer studies where additional or better information was added. Parent samples are superseded by the child samples and not included, but their citation is noted.

B. Samples where measurements of particular input variables in the published dataset were subsequently shown to be inaccurate (and could not be corrected). An example of exclusion for inaccurate values is the recognition that temperature estimates from $\delta^{18}O$ values of diagenetically altered foraminifera were systematically too low (*141*).

C. Datasets where data essential for re-calculating paleo-CO_2 were missing and could not be obtained from the authors.

D. Samples are from oceanic upwelling regions that are far out of equilibrium with atmospheric pCO_2 and thus cannot provide estimates for atmospheric CO_2. This excluded the data of Mejía et al. (*138*), the only diatom-based paleo-CO_2 reconstruction in the database, plus several other alkenone-based studies. These samples are still included in the database as they could be used to examine changes in upwelling or other processes that lead to air-sea disequilibrium. However, they are not used in the reconstruction of atmospheric CO_2.

E. Samples where paleo-CO_2 is calculated using a method that is no longer considered reliable for a particular proxy. For example, Method 1 does not use any correction for cell size – a correction considered essential for the alkenone-based paleo-CO_2 estimates. Therefore, all paleo-CO_2 estimates calculated from alkenone $\delta^{13}C$ values using Method 1 are considered Category 3 data.

In a handful of instances, where data were reported graphically but not in data tables, we used data visualization software (https://automeris.io/WebPlotDigitizer/) to extract the underlying data from the figure. This is documented in the database. Uncertainties on data estimation using this digitization approach are much smaller than measurement and proxy errors and we consider it to be negligible. Return to **Table S2**.

1.4. Calculational methods

We applied four published methods to reconstruct paleo-CO_2 for the data compilation:

- Method 1 – diffusive framework (b) without size correction. Only used for phytane/phytol dataset.
- Method 2 – diffusive framework (b) with correction for cell size based on coccolith morphometry (*38*);
- Method 3 – diffusive framework with b calculated using permeability determined from Pleistocene sediment samples, cell size based upon coccolith morphometry and growth rate based upon a statistical relationship between cell size and growth rate (*34, 41*);
- Method 4 – statistical relationship of ε_p to $\ln([CO_{2(aq)}])$ in culture (*40*) with anchoring to Quaternary samples with known $[CO_{2(aq)}]$ (*34*).

As many methods as allowed by the data were applied to each sample. For example, if a site lacked Quaternary samples for anchoring, then no paleo-CO_2 estimates could be determined for that site with Method 4 (although other Methods could be applied).

We begin by describing the calculation of variables common to all method: sea-surface temperature (SST), sea-surface salinity (SSS), $\delta^{13}C$ of aqueous CO_2, $\delta^{13}C$ of cellular biomass, and ε_p. Following, we describe the calculation of surface ocean pCO_2 with each method, followed by calculation of a weighted mean estimate from all methods. For each of the methods, uncertainties in CO_2 values were determined by Monte Carlo resampling of input parameters. The resulting distribution of pCO_2 values reflects the uncertainties in the input parameters and the 95% confidence interval was calculated from this distribution.

Sea Surface Temperature. The datasets included in the compilation use SST estimates from the proportion of di-unsaturated to tri-unsaturated C_{37} alkenones ($U^{k'}_{37}$), the ratio of Mg to Ca in foraminifera shells (Mg/Ca), and the ratio of internal cyclization of glycerol dialkyl glycerol tetraether (GDGT) membrane lipids (TEX_{86}). The published temperature values in the original studies are used for these proxies because many datasets lacked information (such as raw proxy values) needed for re-calculation. This approach may lead to some increase in the scatter of paleo-CO_2 estimates, and thus recalculation of SSTs would be a natural target for future work.

SST values calculated from $U^{k'}_{37}$, foraminiferal Mg/Ca ratios, and TEX_{86} values were assigned uncertainties of ±1.5, ±1.8, and ±5°C, respectively (±1σ, normally distributed), based upon uncertainties in published calibrations (*173-175*). Analytical uncertainties are typically smaller and are not included here. Where multiple SST estimates are reported (e.g., both $U^{k'}_{37}$ and TEX_{86}), the average of the two is calculated and the uncertainty is determined by the quadrature sum of the individual uncertainties.

Salinity. Salinity has a very minor influence on the solubility of CO_2 in seawater (Henry's constant; K_H) and the resulting [$CO_{2(aq)}$] calculated from algal ε_p. We apply a single salinity value of 35 ± 2‰ (1-sigma normal distribution) to all samples. This uncertainty captures variations from changes in the ocean's water balance (principally from ice volume) as well as probable long-term variations due to changes in solute balance.

Photosynthetic carbon isotope fractionation, ε_p. Isotopic values for algal biomass and aqueous CO_2 are required (Eq. 1.1) and are determined from $\delta^{13}C$ values of biomarkers and foraminifera calcite, respectively, as described below.

$\delta^{13}C_{CO2(aq)}$ values. The value of $\delta^{13}C_{CO2(aq)}$ is determined from surface dwelling planktic foraminiferal $\delta^{13}C$ values, if available. A few studies report DIC $\delta^{13}C_{DIC}$ values calculated from $\delta^{13}C_{foram}$, which we use as is. We use each publication's approach to deal with vital effects. The corrections are generally small and their uncertainty does not significantly affect the final paleo-CO_2 estimates.

$\delta^{13}C_{CO2(aq)}$ from $\delta^{13}C_{DIC}$. Where $\delta^{13}C_{DIC}$ is reported by the original authors, we use the relationship of Rau et al. (*145*) (following from *119, 176*) to calculate $\delta^{13}C_{CO2(aq)}$. Where reported, the 1-sigma uncertainty (normal distribution) in $\delta^{13}C_{DIC}$ is used for error propagation, otherwise an average value of ±0.3‰ (1-sigma, normal) is applied.

$\delta^{13}C_{CO2(aq)}$ from $\delta^{13}C_{foram}$. Where $\delta^{13}C_{foram}$ is reported, we calculate $\delta^{13}C_{CO2(aq)}$ values using the relationship between $\delta^{13}C_{CO2(g)}$ and $\delta^{13}C_{CaCO3}$ of Romanek et al. (*177*) combined with the relationship between $CO_{2(g)}$ and $CO_{2(aq)}$ determined by Mook et al. (*176*). Uncertainty in the $\delta^{13}C$ value of $\delta^{13}C_{CO2(aq)}$ from planktic foraminifera is propagated from the measurement uncertainty of foraminifera $\delta^{13}C$ values (normally distributed standard error of the mean) and uncertainty in the SST (described above). In studies where a uniform uncertainty is reported, a standard deviation is calculated by assuming this uniform distribution is equivalent to $\pm 3\sigma$. Samples with missing uncertainties or uncertainties that are in error (zero, negative values) are assigned the median of the uncertainties from the full dataset. For all data, the standard error of the mean is calculated from the number of observations (if reported), or assuming n=1 if the number is missing.

Several studies rely on $\delta^{13}C$ values of benthic foraminifera to estimate surface ocean $\delta^{13}C$ values. This approach applies a $\delta^{13}C$ offset that is meant to correct for the difference between surface and deep ocean $\delta^{13}C$ of DIC (largely due to the biological pump). We use the $\delta^{13}C$ values with the offset as applied in the original publication.

$\delta^{13}C_{biomass}$ values. Algal biomass $\delta^{13}C$ values are determined from measurement of $\delta^{13}C$ values of sedimentary algal biomarkers (alkenones, phytane/phytol) or fractions of cellular biomass (c.f. organic carbon in diatom frustules). Algal biomass is calculated using empirically determined fractionation factors between biomarker and cellular biomass. Fractionation factors are calculated from measurements of biomass and biomarker $\delta^{13}C$ values in laboratory culture:

$$\varepsilon_{\mathrm{biomass/biomarker}} = \left(\frac{\delta^{13}C_{\mathrm{biomass}}+1000}{\delta^{13}C_{\mathrm{biomarker}}+1000} - 1\right) \cdot 1000 \qquad \text{(Eq. 1.12)}$$

The mean values and uncertainty for $\varepsilon_{\mathrm{biomass/biomarker}}$ are listed in **Table S3**. Uncertainties in $\delta^{13}C$ biomass values reflect the propagated measurement uncertainty of biomarker $\delta^{13}C$ values (±1 standard error of the mean) and the uncertainty in $\varepsilon_{\mathrm{biomass/biomarker}}$. Biomarker $\delta^{13}C$ uncertainty is based upon the standard deviation if reported. If no uncertainty is reported or is entered as zero, then the median of the reported standard deviation across all samples is applied. The standard error of the mean is calculated for all samples using the number of replicates (if reported) or assuming n=2 (as is common for compound-specific isotope analysis). In all cases the normally distributed standard error of the mean is used for error propagation.

We assume that the standard deviation of $\varepsilon_{\mathrm{biomass/biomarker}}$ reflects real differences due to variation in species and growth conditions, and captures differences likely encountered in the modern and ancient oceans. However, we do not include the uncertainty of $\varepsilon_{\mathrm{biomass/biomarker}}$ in the error propagations because this uncertainty is already incorporated in the empirically determined b value (Methods 1 and 2), the calibration of permeability from Pleistocene sediments (Method 3), and the determination of the Quaternary anchor (Method 4).

1.4.1. Method 1 – diffusive framework, no size corrections

The procedure for Method 1 is:

1. calculate $\delta^{13}C_{\mathrm{biomass}}$ from measurements of $\delta^{13}C_{\mathrm{biomarker}}$ and Eq. 1.12.

2. calculate $\delta^{13}C_{CO_{2(aq)}}$ from planktic foraminifera or DIC $\delta^{13}C$. The proxy reconstruction of SST is used for the temperature dependence of these equations.
3. calculate ε_p (Eq. 1.1) from $\delta^{13}C_{biomass}$ and $\delta^{13}C_{CO_{2(aq)}}$
4. determine a *b* value from $[PO_4^{3-}]$ using Eq. 1.13 below
5. calculate $[CO_{2(aq)}]$ from ε_p, ε_f, and *b* with Eq. 1.2
6. calculate pCO_2 from $[CO_{2(aq)}]$ and the temperature-adjusted Henry's law constant.

We chose a uniform approach for calculating uncertainty to facilitate meaningful comparisons between samples. The uncertainty of the calculated pCO_2 was determined by 10,000 Monte Carlo simulations where each input parameter is resampled for every sample in the database 10,000 times. This assumes uncorrelated uncertainties in the input parameters. Parameters like SST that are used several times in the calculation of pCO_2 from a sample are only resampled once per Monte Carlo realization.

The b value is correlated to $[PO_4^{3-}]$ in the modern ocean, and this relationship is used to estimate a b value for each sampling location and its associated uncertainty. In this method the relationship of b to $[PO_4^{3-}]$ is assumed to remain unchanged in the past. The published $[PO_4^{3-}]$ value from each study is used in the recalculation and applied as a constant value for each site in a publication. We apply a uniformly distributed uncertainty equal to ±20% of the published $[PO_4^{3-}]$ value from the original study. The b values used for this relationship are recalculated with Eq. 1.3 using an ε_f value of 26.5‰. We use the compiled calibration data of Hernández-Almeida et al. (*144*) and a linear least-squares regression to relate *b* and $[PO_4^{3-}]$ to calculate *b* values (Fig. S1):

$$b = 129.621\left[PO_4^{3-}\right] + 93.043 \qquad \text{(Eq. 1.13)}$$

We calculate uncertainty in the calculated *b* values from both the uncertainty in $[PO_4^{3-}]$ values, the uncertainty in the fitted slope and intercept of the *b*-$[PO_4^{3-}]$, and the residuals from this fit. Uncertainty in the $[PO_4^{3-}]$ value has traditionally been the primary uncertainty propagated into paleo-CO_2 estimates, with some studies also including uncertainty in the fitted slope and intercept of the *b*-$[PO_4^{3-}]$ relationship. However, the residuals in the fit are substantial and reflect additional effects not captured in the *b*-$[PO_4^{3-}]$ relationship. We therefore include the residual uncertainties as a more complete measure of the uncertainty in the *b* value (Fig. S1). At low $[PO_4^{3-}]$, the uncertainty in the regression prediction can (rarely) return values for *b* that are zero or negative. In such a case, additional Monte-Carlo draws are done until no zero or negative *b* values are present.

All samples using phytane or phytol to determine biomass $\delta^{13}C$ are assigned a b value at the midpoint of the range in the calibration Tables S2 and S3 of Witkowski et al. (*127*). The uncertainty is applied as a uniform distribution with values that span the range of b values in the calibration tables ($b = 191 \pm 89$, uniform distribution). This value and distribution are chosen to capture the range of values present due to the variety of sites in these datasets. Return to **Table S2**.

1.4.2. Method 2 – diffusive framework with size correction

The calculation of PCO_2 and uncertainty using Method 2 is identical to Method 1 except that a correction to the *b* term is applied for changes in cell size:

1. calculate steps 1-4 as described in Method 1 (above)
2. calculate a mean cell radius using coccolith length and Eq. 1.14 (described below)
3. calculate a b' term corrected for changes in V/S using Eq. 1.7
4. calculate $[CO_{2(aq)}]$ from ε_p, ε_f, and b' with Eq. 1.2
5. calculate PCO_2 from $[CO_{2(aq)}]$ and the temperature-adjusted Henry's law constant.

Coccolith length is taken as reported in individual studies, with reported uncertainties used to determine the ±1-sigma range of a normal distribution. Uncertainties reported as both a positive and negative value are averaged to give a single, normally distributed, uncertainty value. Samples with a coccolith length but a missing or zero uncertainty value are assigned the median of the distribution of all uncertainties from samples with measured values, and a uniform distribution is used for error propagation. Alkenone samples that do not have a measured coccolith length are assigned a size that is the midpoint of the range of sizes in the distribution of all samples with measured values. These samples are assigned a uniformly distributed uncertainty that spans the range of coccolith lengths found in all samples with measured values.

Cell radius is calculated from coccolith length using the relationship between radius (r) and length (L) measured on discrete individual coccospheres found in Cenozoic sediments (Fig. S2) (*38*). The uncertainty in coccolith length, and the parameter uncertainty in the regression are used to propagate the error in predicted cell radius. The parameter uncertainty is the appropriate uncertainty, as the residual uncertainty would overestimate the uncertainty in the population of cell radii. At small coccolith length, the uncertainty in the regression prediction can (rarely) return values for the cell radius that are zero or negative. In such a case, additional Monte-Carlo draws are done until no zero or negative cell radii are present. Cell volume, surface area, and the volume/surface area ratio are calculated from the cell radius assuming a spherical cell. Uncertainties in the radii are propagated through these calculations.

In Method 2, Eq. 1.7 is used to calculate a revised *b'* value that reflects changes in cell size in the past. An important consideration is the modern cell size used to normalize past cell sizes. We follow the original work of Henderiks and Pagani (*38*) and use a V/SA ratio of 0.9 µm, determined from *E. huxleyi* cultures, to normalize past V/SA ratios and calculate *b*' values. Return to **Table S2**.

1.4.3. Method 3 – diffusive framework with cell size and growth-rate

Zhang et al. (*41*) developed an approach to calculating b that uses cell size to calculate both growth rate and the effects of V/S changes (Eq. 1.9). In this method, b is determined by six parameters, and among those, sensitivity analyses show that b is mostly dependent on growth rates, cell size and membrane permeability to CO_2.

The detailed procedure to calculate PCO_2 with this method is:

1. calculate steps 1-3 as described in Method 1 (above)

2. calculate a mean cell radius using coccolith length and Eq. 1.14 (as in Method 2)
3. calculate a cell carbon content using Eq. 1.10
4. calculate instantaneous growth rate from cell radius using Figure S3
5. calculate a b value from Eq. 1.9
6. calculate [CO2(aq)] from ε_p, ε_f, and b with Eq. 1.2.
7. calculate pCO_2 from $[CO_{2(aq)}]$ and the temperature-adjusted Henry's law constant.

Membrane permeability. The membrane permeability of Pleistocene alkenone-producers is 5.09±0.16 × 10^{-5} m s^{-1}, calculated using ice core CO_2 and $\boldsymbol{\varepsilon_p}$ data at two sites, based on a bootstrap resampling technique *(41)* (Sec 1.2.2). Uncertainty in the permeability is propagated from a normal distribution with a ±1-sigma of 0.16 × 10^{-5} m s^{-1}.

Cell carbon content and Qs. The cellular carbon content (POC/cell) is calculated from the cellular volume using Eq. 1.10 *(Eq. 3 in 41)*. The cell volume is derived from measurements of coccolith length and the uncertainty in volume is propagated through the calculation of cellular carbon content.

Growth rate from cell volume. The empirical relationship between coccolithophore cell volume (V) and instantaneous growth rate (μ_I) was established using the data from 89 nutrient- and/or light-limited chemostat and semi-continuous diluted batch culture experiments compiled by Aloisi *(157)* and calculated by Zhang et al. *(41)* (Fig. S3). This growth rate is an instantaneous growth rate that accounts for the light/dark photoperiod length and respiration in algal experiments.

Uncertainty in growth rate is from both the uncertainty in the cell volume (as propagated from the lith length), the uncertainty in the fitting parameters of the relationship, and the residuals from this fit (Fig. S3). We include the residual uncertainties as a more complete measure of the overall numerical uncertainty in the growth rate. Return to **Table S2**.

1.4.4. Method 4 – Statistical framework with Quaternary anchoring

Rae et al. (*34*) presented paleo-CO_2 estimates recalculated using a statistical relationship between $\ln[CO_{2(aq)}]$ and ε_p found in laboratory algal cultures (*40*). The detailed procedure is:

1. calculate steps 1-3 as described in Method 1 (above)
2. for Quaternary-age samples, calculate pCO_2 and $[CO_{2(aq)}]$ from the ice-core CO_2 record
3. for Quaternary-age samples, use Eq. 1.11 to calculate the mean Quaternary anchor value for each site (described below)
4. For each site, use Eq. 1.11 to calculate $[CO_{2(aq)}]$ from ε_p and the Quaternary anchor (described below)
5. calculate pCO_2 from $[CO_{2(aq)}]$ and the temperature-adjusted Henry's law constant.

Calculating pCO_2 and $[CO_{2(aq)}]$ from the ice-core CO_2 record. The surface ocean pCO_2 at the age of

each Quaternary sample is calculated from the ice core CO_2 record (*11*) by linear interpolation between data points. The [$CO_{2(aq)}$] value in equilibrium with this PCO_2 value is then calculated each of these samples using Henry's law and the proxy SST value from each sample. These ice-core-inferred [$CO_{2(aq)}$] values are the target for anchoring the relative paleo-CO_2 changes at each site.

Calculating the Quaternary anchor. For each Quaternary-aged sample, an offset value ($I_{sample,Quaternary}$) is calculated for each sample with Eq. 1.11. The mean of these offset values for each site is then used as the Quaternary anchor ($I_{Quaternary}$) for that site. The standard error of the mean for the offset is used in the uncertainty analysis.

Calculating [$CO_{2(aq)}$] from ε_p and the Quaternary anchor. The aqueous CO_2 concentration is calculated from $\boldsymbol{\varepsilon_p}$, the Quaternary intercept ($\boldsymbol{I_{Quaternary}}$), and the slope of the statistical relationship between $\boldsymbol{\varepsilon_p}$ and ln([$CO_{2(aq)}$]) as determined by Stoll et al. *(40)* using Eq. 1.11. The uncertainty in each parameter is propagated through subsequent calculations, including $\boldsymbol{m}$ = 2.66 ±0.42 (1-sigma, normal distribution). Note that this approach ignores the effects of cell size, growth rate, and irradiance that were also present in the statistical relationship.

Uncertainty in this approach is calculated from the uncertainty in (m) from the statistical fit between ε_p and ln[$CO_{2(aq)}$] as well as the standard error of the mean of the Quaternary anchor, and the propagated uncertainty in ε_p. Return to **Table S2**.

1.4.5. Calculation of weighted mean paleo-CO_2 from all Methods

Surface ocean PCO_2 and atmospheric pCO_2 are equal in ocean regions where surface seawater and the atmosphere are in CO_2-equilibrium, and at sea level (with ~1 atm pressure) PCO_2 and pCO_2 are approximately equal to the mole fraction of CO_2 (x_{CO2}), which is independent of altitude. To prevent any altitude effects, all proxies in this study report x_{CO2}, which we generally call 'paleo-CO_2'. Consequently, we refer to phytoplankton PCO_2 estimates as paleo-CO_2 and because we have applied up to 4 Methods for each ε_p value, we need to determine a mean paleo-CO_2 value for each sample. To do so, only Category 1 data are used, so not all methods are used for every sample. For each sample, the mean paleo-CO_2 is the inverse-variance weighted mean. Calculations are done on ln(PCO_2) values as their uncertainties more closely approximate a normal distribution.

The detailed procedure to calculate paleo-CO_2 with this method is:

1. For each sample, calculate ln(PCO_2) on Methods with Category 1 estimates. This calculation is done on the central PCO_2 estimate and the Monte-Carlo resampling-derived distribution of PCO_2 values (reflecting the uncertainty in the input parameters).
2. Calculate the variance of ln(PCO_2) from the Monte-Carlo derived distributions for each Method in each sample.
3. Calculate the inverse-variance-weighted mean ln(PCO_2) value for each individual Monte-Carlo resampled estimate in each sample. The distribution of these values is the distribution of the new weighted-mean ln(PCO_2) estimate. This approach reduces the

variance from parameters that are independent between the methods, while preserving variance from parameters shared between the methods.

4. Calculate paleo-CO_2 from the distribution of mean ln(PCO_2) estimates.

This approach assumes that the estimates of PCO_2 by the different methods are independent. Several of the underlying variables are common to all methods (e.g., ε_p, SST) which could violate this assumption. However, many of the parameters are unique to each method and thus would make the methods independent of each other. We tested this assumption by examining the correlation between the Monte-Carlo distribution of PCO_2 estimates from different methods in a single sample. These estimates were highly uncorrelated indicating the methods are largely independent and the weighted-mean approach is reasonable. An example of this lack of correlation is shown in Fig. S4. Return to **Table S2**.

1.5. Future opportunities

The approaches used here to re-calculate pCO_2 values from algal $\delta^{13}C$ values mostly rely on the assumption of diffusive (or diffusive-like) supply of CO_2 and an ε_f value that is assumed to reflect $\varepsilon_{RuBisCO}$. However, algal ε_p records generated using these models are unable to consistently capture both the late Pleistocene glacial-interglacial paleo-CO_2 changes (*107, 150, 151*) and the large ε_p values of the early Cenozoic. Some modifications appear to be required, and such revisions are nascent and an active area of research (cf. *39-41, 107, 138, 151, 152, 161*). Below we outline future research directions that may help address these issues and improve the algal paleo-CO_2 proxy. The cell size – growth rate relationship provides a possible approach to construct *b* as a variable for every sample used for paleo-CO_2 estimates. Automated systems have been developed to perform regional mapping of the size and weight of coccoliths in natural settings (e.g., *178, 179*). In the future, these techniques could be used in the field to better evaluate the potential of using coccolith size as an indicator of haptophyte growth rate and hence *b*. This should include evaluation of potential changes over time in the relationship of coccolith size to growth rate.

It is critical to replicate and extend the *in vitro* measurements of $\varepsilon_{RuBisCO}$ within algal groups. Measured carbon isotope fractionation in nutrient-limited, light-replete continuous chemostat cultures consistently indicate an effective maximum fractionation of ~25‰ for eukaryotic phytoplankton (*128, 148, 180*). Values approaching 25‰ are also found in Eocene and Oligocene sediments. Confirmation of the Boller et al. (*131*) *E. huxleyi* result of ~11‰, plus experiments on other algal groups, are needed to determine the magnitude of carbon isotope fractionation in algal carbon fixation.

The isotopic consequences of CCMs also remain largely unknown. CCM activity has been shown to increase with carbon limitation (e.g., *40, 181, 182, 183*). Such an effect modifies the [$CO_{2(aq)}$]-ε_p relationship but may not present an insurmountable challenge to the existing proxy calibration if CCM activity is expressed in proportion to [$CO_{2(aq)}$]. However, CCM activity may also be sensitive to interactions of light and nutrient limitation. For example, Wilkes et al. (*161*) proposed that a strongly fractionating CCM based on unidirectional hydration of CO_2 becomes active under nutrient-limited growth when photon fluxes exceed the requirement to synthesize biomass. Studies that relate CCM activity and isotopic consequences to [$CO_{2(aq)}$], nutrient

availability, and irradiance will be essential in order to account for such effects in paleo-CO_2 studies.

Coccolith calcite may be an additional avenue to reconstruct the past physiology of these organisms. The trace element geochemistry of coccoliths may incorporate a record of growth rate (e.g., *184*), while their stable isotopic composition ($\delta^{13}C$ and $\delta^{18}O$) is impacted by irradiance (e.g., *185*). Whether qualitative or quantitative, these properties may yield insights into algal growth or paleo-CO_2 directly (cf. *114*).

All of the factors described above are observed in laboratory cultures, the modern ocean, or core top sediments where we can constrain many environmental factors such as nutrient concentration, irradiance, temperature, and [$CO_{2(aq)}$]. While direct paleo-proxies for nutrients and irradiance generally do not exist, proxies for oceanographic setting such as mixed layer depth and thermocline strength are sometimes available. A promising approach will be to relate these biological factors important for algal ε_p values to (paleo)oceanographic settings to improve estimates of past CO_2 levels. This same approach could also be useful to address ecological questions important for phytoplankton pCO_2. For example, better constraints on the depth of phytoplankton production in the past would inform the degree to which the reconstructed [$CO_{2(aq)}$] is in equilibrium with the atmosphere (i.e., the near surface versus, e.g., the deep chlorophyll maximum). Return to **Table S2**.

2. Boron Proxies

2.1. Current understanding of boron proxies and recent advances

The boron isotope and B/Ca proxies, recorded in marine carbonates, are built upon the predictable change in the abundance and isotopic composition of dissolved borate ion in seawater with a change in seawater pH (*186*). In open-ocean regions where surface waters are in equilibrium with the atmosphere, surface ocean pH closely tracks atmospheric CO_2. As such, these regions are targeted for boron-based paleo-CO_2 reconstructions, by measuring B/Ca or (more commonly) $\delta^{11}B$ in fossil shells of surface ocean dwelling planktic foraminifera from open ocean sediment cores. Since the common basis of these proxies was first proposed by Vengosh et al. (*187*) and Hemming and Hanson (*188*), both proxies have been subject to considerable testing and ground-truthing, and have evolved and developed considerably over the last couple of decades.

Of the two boron-based proxies, the future of planktic B/Ca as a proxy for CO_2 is less secure. The dependence of planktic foraminiferal B/Ca on seawater pH has been repeatedly demonstrated in culture (*189-194*), but a number of secondary factors has also been shown to affect B/Ca. These include salinity (*189, 195*), dissolved inorganic carbon concentrations, or [DIC] (*189, 194*), light intensity (*196*), nutrient concentrations (*195*), surface ocean saturation state (*197*), or calcification intensity (*198*). Of these secondary factors, the apparent dual dependency of the B/Ca proxy on pH and [DIC] could have great potential when paired with pH data from boron isotopes to solve the whole carbonate system and derive surface ocean paleo-CO_2, provided error propagation is comprehensive (*199, 200*). While this is a powerful approach, and the coherent changes often seen between $\delta^{11}B$ and B/Ca in deep time studies (*200-203*) are consistent with a

predominant carbonate-system control on B/Ca as seen in culture, some lingering uncertainties remain. Specifically, until the sensitivity of B/Ca to the other secondary factors listed above can be falsified or corrected for, this will remain a background structural uncertainty to the application of B/Ca in planktic foraminifera shells to trace paleo-CO_2.

Contrastingly, since the first studies exploring the potential of the boron isotope proxy for reconstructing past atmospheric CO_2 (*204, 205*), subsequent culture and open-ocean studies have repeatedly shown that planktic foraminiferal $\delta^{11}B$ is predominantly a function of pH and the well-understood dependency of pK^*_B on temperature, salinity and pressure (*186, 206*). Notwithstanding refinements in the underlying physicochemical understanding of the proxy (*207, 208*), the basic understanding of the proxy has endured largely unchanged since the early studies of Hemming and Hanson (*188*) and Sanyal et al. (*204*). Because the $\delta^{11}B$ recorded in marine carbonates closely relates to the $\delta^{11}B$ of dissolved borate in seawater, pH can be calculated via $\delta^{11}B_{borate}$ from $\delta^{11}B_{CaCO3}$ as follows:

$$\delta^{11}B_{borate} = (\delta^{11}B_{CaCO3} - c)/m \quad \text{(Eq. 2.1)}$$

where c is the intercept and m the slope of the regression (*191*).

$$pH = pK^*_B - \log\left(-\left(\delta^{11}B_{sw} - \delta^{11}B_{borate}\right) / \left(\delta^{11}B_{sw} - \alpha_{B3\text{-}B4} * \left(\delta^{11}B_{borate}\right) - \varepsilon_{B3\text{-}B4}\right)\right) \quad \text{(Eq. 2.2)}$$

where pK^*_B is the dissociation constant of boric acid in seawater (*186, 206*), $\delta^{11}B_{sw}$ is the boron isotopic composition of seawater, $\alpha_{B3\text{-}B4}$ is the aqueous boron isotope fractionation factor (*207, 208*) and $\varepsilon_{B3\text{-}B4}$ the corresponding aqueous boron isotope fractionation. Because carbon speciation in seawater is coupled to equilibrium reactions, CO_2 can then be calculated from pH when paired with a second parameter of the marine carbonate system (e.g., alkalinity, dissolved inorganic carbon, $\Omega_{calcite}$), in addition to estimates of temperature, salinity and pressure. For a review of how this is done in practice, see Rae (*31*) and Hönisch et al. (*30*). It is worth noting that *relative* change in CO_2 climate forcing can often be effectively reconstructed using boron isotopes even in the absence of these other constraints on seawater chemistry (*209*).

In recent years, the main advances in our understanding have come largely in the realm of understanding foraminiferal vital effects (both in extant and extinct species), in more fully propagating uncertainty, and in the application of seawater dissociation constants adjusted for seawater major ion variability on multi-million-year timescales (*210, 211*). In terms of vital effects, more and more measurements of open-ocean Holocene foraminifera have revealed coherent patterns across species, with surface-dwelling symbiont-bearing foraminifera recording higher pH than ambient seawater (e.g., *191, 212, 213, 214*), and symbiont-barren and/or deeper-dwelling species recording lower pH than their surrounding seawater (e.g., *212, 215-221*). Thus far, these findings have largely been in-keeping with existing models of vital effects being driven by chemical alteration in the foraminiferal microenvironment (*218, 222, 223*). Return to **Table S2**.

2.1.1. Uncertainties and error propagation

Uncertainty propagation has greatly been improved since the earliest boron isotope-based pH and paleo-CO_2 reconstructions that only considered the analytical uncertainty of the boron isotope analysis (e.g., *204, 205*). Following Hönisch & Hemming (*224*), the additional

uncertainties of the second parameter of the carbonate system, temperature, salinity and pressure are now commonly accounted for. More recently, and partly by necessity when approaching deeper time questions, studies have begun to quantify uncertainties inherent in species-specific calibrations, uncertainties on the $\delta^{11}B$ of bulk seawater and variable seawater elemental composition through time, to name a few (e.g., *60, 68, 225-227*). Often, these error propagations use Monte Carlo approaches, which can be beneficial in yielding probability density functions of paleo-CO_2 that can be incorporated into future time series analysis, and can often better cope with linked uncertainties that apply at multiple stages on the path to a paleo-CO_2 estimate (e.g., major ion chemistry effects on accessory Mg/Ca temperatures, equilibrium constants, and carbonate saturation). Return to **Table S2**.

2.2. Criteria for vetting boron proxy records and data revisions

The paleo-CO_2 archive includes only boron proxy records that have been collected in the open ocean and outside of upwelling areas (*56, 60, 68, 156, 164, 191, 199, 205, 212, 215, 224-226, 228-240*). Several published studies have recalculated earlier data with the most recent proxy understanding and error propagation routines (e.g., *225, 230, 231, 239*), so that much of the vetting process focused on identifying superseded data and eliminating duplicate representation (for details, see vetting information in individual product proxy sheets).

Only three boron proxy studies have been placed in Category 3. These include Tripati et al. (*228*), who used the B/Ca proxy and their CO_2 estimates have been found to be driven mostly by temperature, while the actual B/Ca data play only a very minor role in the CO_2 these authors reconstructed (*241*). Stap et al. (*240*) did not measure the boron concentrations of their samples and their large data variability suggests their signal to noise ratio was too small. In addition, the pioneering work of Pearson and Palmer (*205*) over the Cenozoic is subject to uncertainties stemming from the inclusion of some mixed species foraminifer samples, variable size fractions, unverifiable efficacy of sample cleaning, and laboratory-specific analytical offsets. Anagnostou et al. (*212*) attempted to correct the data for these technique-specific offsets but cautioned that variable size fractions and possibly other factors might undermine this correction. Given that better-constrained and more highly-resolved data are now available, we err on the side of caution and exclude the data of Pearson & Palmer (*205*) from the vetted compilation.

The B/Ca study of Haynes & Hönisch (*199*) reports paleo-CO_2 estimates for the PETM, but the CO_2 estimates require two uses of pH estimates from boron isotopes, once to remove the pH (or better: the borate ion concentration) effect from the B/Ca signal, and then again to pair the DIC signal with pH as the second parameter of the carbonate system. Because of this, the CO_2 estimates are not strictly independent, and have been excluded from Category 1. However, given the growing uncertainty of CO_2 reconstructions further back in time, and the entirely proxy-based calculation, we report the data in Category 2.

Finally, Anagnostou et al. (*60, 212*), Sosdian et al. (*239*), Henehan et al. (*68*) and Guillermic et al. (*242*) provide multiple scenarios for CO_2 depending on underlying assumptions made. To eliminate duplicate representation of the data, the vetted product includes only one of those options, which has been selected in consultation with the original authors as the most likely best estimate. For example, Sosdian et al. (*239*) explored a range of options for the Mg and Ca elemental composition of seawater, the depth of the CCD and $\delta^{11}B_{sw}$. Of these, the best estimates

used the elemental composition from fluid inclusions (*243, 244*), the CCD after Pälike et al. (*245*), and $\delta^{11}B_{sw}$ after Greenop et al. (*246*). For details on other boron proxy studies, please review the vetting information in individual product proxy sheets. Return to **Table S2**.

2.3. Future directions

Although great progress has been made in grounding and expanding the boron isotope proxy in particular in the past decades, several key areas remain where there is scope to improve the precision and reliability of past CO_2 reconstructions. Broadly speaking, these fall into four categories: 1) detection and quantification of vital effects in extinct foraminifera; 2) better and independent reconstructions of past $\delta^{11}B_{sw}$; 3) improved reconstruction of the second parameter of the carbonate system, and 4) analytical advances.

As previously discussed, vital effects in modern planktic foraminifera are increasingly widely documented, with all modern species displaying some offset in $\delta^{11}B$ from the $\delta^{11}B$ of ambient borate ion. When applying the boron isotope proxy as far back as the first appearance of *T. trilobus* (~23 Ma, *247*), empirical calibrations based on extant species (e.g., *191, 219, 223, 225, 235, 239*) can be used. Earlier in the Cenozoic, however, the question of whether and how to apply modern-species calibrations to extinct species adds a structural uncertainty to paleo-CO_2 reconstructions, and has led to subtly different approaches being taken in earlier Cenozoic studies published to date. Anagnostou et al. (*212*) found that applying modern analogue vital effects to different tropical Eocene taxa according to their habitat depth and strength of photosymbiosis (as discerned from species-specific trends in $\delta^{18}O$ and $\delta^{13}C$ with shell size) resulted in likely unrealistic reconstructions of the water column pH profile. Because this study found certain shallow-dwelling photosymbiotic Eocene taxa not to display resolvable increases in $\delta^{11}B$ with size (as mixed-layer photosymbiotic species do today, *191, 213*), the authors suggested that boron isotope vital effects in the Eocene may have been smaller than observed in modern species. In contrast, Henehan et al. (*68*) found that applying modern analogue vital effects to middle Eocene planktic foraminifera successfully reconciled otherwise divergent trends in reconstructed pH from different species and locations, lending tentative support to this approach. Similarly, using modern vital effect calibrations for different species results in a more consistent magnitude of surface ocean pH change across the Paleocene-Eocene Thermal Maximum (*202*). Collectively, these deep-time studies illustrate the importance of careful interrogation of potential taxon-specific vital effects in extinct foraminifera. Fortunately, and in practice, the difference between Eocene paleo-CO_2 calculated from tropical mixed-layer taxa using a modern *T. sacculifer/trilobus* calibration is typically within uncertainty of assuming no vital effects at all (*60, 212*). That said, the fact that symbiont-bearing calibrations typically have a lower sensitivity of $\delta^{11}B$ to pH means that this decision also affects the magnitude of pH and paleo-CO_2 change reconstructed over a given interval or excursion (e.g., *30, 201, 202*).

To resolve issues surrounding vital effects going forward, there is a clear need to mechanistically understand vital effects in foraminiferal $\delta^{11}B$ and place this in a numerical framework that allows prediction of $\delta^{11}B$ vital effects in extinct species given a number of measurable parameters (e.g., foraminiferal test volume, presence/absence of spines, depth habitat, carbon and boron isotope changes with size/ontogeny, B/Ca ratios). A basis for this exists in the pioneering model of Zeebe et al. (*222*), which has already been useful in explaining vital effects on early Cenozoic

foraminiferal $\delta^{13}C$ (*248*), and might yet be used to predict deep time boron isotope vital effects pending further empirical physiological measurements from laboratory cultures (e.g., rates of respiration, photosynthesis and calcification, and spatially-resolved microenvironment pH change). Recent work has also demonstrated the power of fast repetition rate fluorometry (FRRF), Chlorophyll *a* quantification, and symbiont counts to quantify photosynthetic capacity (*223, 249, 250*), providing encouragement that these sorts of advances are within reach. Similarly, to constrain respiration rates in extinct species, shell porosity may yet prove informative (*251*).

Besides vital effects, another source of considerable uncertainty further back in geological time is the boron isotope composition of seawater, $\delta^{11}B_{sw}$ – a crucial parameter in converting foraminiferal $\delta^{11}B$ to seawater pH. A number of techniques has been used to estimate this parameter: researchers have studied which values of $\delta^{11}B_{sw}$ would produce feasible vertical ocean pH gradients or ocean saturation states given measured foraminiferal $\delta^{11}B$ (*212, 232, 234, 246, 252*), or have compared bottom water pH reconstructed from benthic foraminiferal $\delta^{11}B$ to predictions of Earth system models, and back-calculated $\delta^{11}B_{sw}$ (*253*). While often elegant, all approaches rely to some extent on model reconstructions of either ocean pH, alkalinity or [DIC], and some require assumptions to be made about the presence, magnitude or sign of vital effects, which as we discuss above, are not always certain. If a reliable independent record of $\delta^{11}B_{sw}$ could be found, it would remove a significant source of uncertainty in Cenozoic paleo-CO_2 reconstruction from this proxy. Fluid inclusions might yet provide one such archive, although the only reconstruction of $\delta^{11}B_{sw}$ from fluid inclusions published to date from evaporites (*254*) produced values too low to be compatible with early Cenozoic carbonate $\delta^{11}B$ values. Model estimates based on the long-term boron cycle also exist (*255, 256*), but these are extremely sensitive to the assumptions made (*257*), and cannot easily be corroborated independently.

Similarly, improving estimations of a second parameter of the marine carbonate system is an area of active research. In the absence of a proxy for alkalinity or DIC, reconstructions of Pleistocene CO_2 have tied modern alkalinity or DIC to sea level-modulated variations in salinity (e.g., *191, 224*), but variations in terrestrial weathering, mantle fluxes and seafloor weathering on multi-million year time scales have changed the elemental composition of seawater over the Cenozoic (e.g., *258*) and therefore also alkalinity and DIC (e.g., *211, 259*). Because the relative importance of weathering and mantle fluxes on marine carbonate chemistry is only weakly constrained, deeper time reconstructions therefore often utilize the surface ocean calcium carbonate saturation state (i.e., $\Omega_{calcite} = [Ca]_{sw} * [CO_3^{2-}]/K_{sp}$) as a constraint (e.g., *60, 68, 212*). This is because model estimates suggest that surface ocean $\Omega_{calcite}$ varied little (i.e., ±1) over the Cenozoic (*211, 245, 259, 260*). Studies often apply a modern or a modelled latitudinal gradient of $\Omega_{calcite}$ (e.g., from 6.5 in the tropics to 4.5 in the high latitudes), with some bounds of uncertainty, to estimate paleo-$\Omega_{calcite}$. This provides a reasonable approximation to surface ocean $[CO_3^{2-}]$, which can then be paired with $\delta^{11}B$-derived pH to estimate paleo-CO_2. We note however that reconstructions based on this approach are doubly subject to uncertainty in past ocean [Ca], since [Ca] is used both for adjusting dissociation constants in deeper time reconstructions and also in the numerator of $\Omega_{calcite}$. Although development of a targeted DIC or alkalinity proxy would substantially refine paleo-CO_2 estimates from boron isotopes, efforts to date have not yet found a proxy candidate with sufficient sensitivity or specificity.

Further development of the boron isotope proxy can also be made by leveraging recent analytical advances. Technological improvements, such as $10^{13}\Omega$ amplifiers (*261*) allow precise measurements to be made from < 2 ng of B, opening up the proxy to time periods where suitable carbonate material may be scarce. Additionally, the ability to analyse smaller samples should permit better exploration of vital effects: for instance, increasing $\delta^{11}B$ with shell size is a diagnostic feature of modern symbiont-bearing foraminifera (*203, 213, 217*), but typical ~20 cm^3 IODP core samples rarely yield sufficient material to analyse multiple size fractions of a species with previous sample-size requirements. Furthermore, new amplifiers coupled with advances in correcting for $CaCO_3$-matrix effects (*262-264*), could allow chamber-by-chamber analyses of foraminiferal shells by in situ laser ablation approaches - potentially informing on depth migration and changing physiology with ontogeny. Return to **Table S2**.

3. Stomatal frequencies

3.1. Current understanding of stomatal frequency proxies and recent advances

McElwain and Steinthorsdottir (*23*), Porter et al. (*265*) and Konrad et al. (*22*) provide a comprehensive overview of stomatal frequency proxies, their assumptions, limitations and recent methodological advances. These proxies are based on the observation that the frequency of stomatal pores often scales inversely with the concentration of atmospheric CO_2 during growth. This is because stomatal complexes are the main sites for CO_2 and water vapor exchange, and leaves operate following optimality principles to maximize CO_2 uptake and minimize water loss. Consequently, **stomatal density**, i.e., the number of stomata per unit leaf area, is typically low when atmospheric CO_2 is abundant, thereby minimizing water loss. In contrast, when CO_2 is low, a high stomatal density is necessary to ensure sufficient carbon supply, albeit at a higher water cost. Although conceptually straight-forward, the stomatal density proxy is affected by multiple environmental parameters in addition to CO_2 and there are always biological exceptions to these rules. This led to the use of the **stomatal index**, which is the percentage of stomata in the sum of stomatal and epidermal cells. The stomatal index is much less affected by humidity and other non-CO_2 factors than stomatal density, but both proxies (stomatal density and index) are explicitly defined by calibrations using living species. The **stomatal ratio** extends the concept to extinct species, by relating the ratio of modern/paleo stomatal density or stomatal index to the ratio of paleo/modern CO_2.

While leaf growth and subsequent development of stomatal patterning, geometry and density in direct contact with the paleoatmosphere is a major advantage of these proxies, the stomatal density and index proxies (also called transfer functions) are empirical and their calibrations are time consuming. While several studies have recorded species-specific responses (sometimes—but not always—different even within the same genus), many genera (and even higher taxonomic levels) record similar stomatal densities and stomatal indices of fossil leaves, and parallel responses to CO_2 (e.g., *266, 267-270*). To date, around 40 species have been calibrated for the stomatal density and stomatal index proxies, which means that most of the paleobotanical record currently cannot be used when the goal (such as here) is to generate fully quantitative CO_2 records that can be compared to independent proxy estimates. However, much can still be learned about relative paleo-CO_2 changes using more semi-quantitative methods, such as

stomatal ratios and **stomatal indices** calibrated with non-conspecific nearest living equivalents. In addition, many species lose their sensitivity at high CO_2 (above 500 to 1000 ppm), meaning that the upper uncertainties become unbounded, whereas others only seem sensitive to above-ambient CO_2 (*271, 272*). Recent advances address several of these limitations (*22, 23*), and assemblage approaches have been suggested to overcome inter-species variations (e.g., *265*). Return to **Table S2**.

3.1.1. Uncertainties and error propagation

Most recent estimates using calibrated functions of stomatal density and stomatal index constrain the uncertainties in estimated CO_2 by propagating the uncertainties in the calibration function and fossil measurements using Monte Carlo simulations (*269, 273*). Our strategy for updating uncertainties in older estimates is described in the following section. Return to **Table S2**.

3.2. Criteria for vetting stomatal frequency proxy records and data revisions

A total of 29 Cenozoic records has been published using these proxies (*95, 266, 273-299*). *Category 3:* Several records are considered unreliable in their current form, some for multiple reasons. For instance, stomatal density is usually more strongly affected than stomatal index by variations in environmental factors such as water availability and irradiance (*300*); this impacted three records (*276, 289, 297*). Estimates of Retallack (*285*) are based on measuring stomatal index from published figures of mixed quality (see examples in *277*) and do not represent a random field-of-view. Some stomatal index estimates applied calibrations of extant species to different fossil taxa (*281, 283, 285, 289-293*), the concern being that some stomatal index responses to CO_2 are species-specific, even within the same genus (*95, 266, 271, 301-303*), although this is not always the case (see above). Furthermore, some estimates do not fully propagate uncertainties in both the fossil and calibration measurements (*95, 281, 289, 291, 292, 295, 304*). In such cases where the calibration data are publicly available, estimates not placed into Category 3 for other reasons were revised using the approach of Beerling et al. (*273*), which fully propagates uncertainties in all fossil and calibration measurements (*95, 277, 295*). Similarly, the *Metasequoia* estimates of Beerling et al. (*273*) were updated with the more extensive calibration of Doria et al. (*280*).

Category 2: The stomatal ratio proxy relates the ratio of paleo-to-modern CO_2 to the ratio of fossil-to-modern stomatal density or stomatal index. The proxy assumes a prescribed inverse power law response between CO_2 and stomatal frequency, and applies a one-point calibration between present-day CO_2 and stomatal frequency measurements (e.g., *305*). This proxy is most often applied when the nearest living relative of a fossil is not clearly known and where it can be argued that selection of an ecological and/or morphological equivalent is a more robust approach than selection of a very distantly related phylogenetic relative. As such, these estimates and their associated uncertainties are less quantitative (*298, 306*) and thus cannot be compared directly to more quantitative estimates from other proxies. Because of this, we place stomatal ratio estimates into Category 2 if they do not otherwise satisfy conditions for Category 3 (*287, 290-293, 298, 299*). In cases where estimates at individual sites are based on multiple species (*292, 293*), the mean of the individual estimates and uncertainties is reported.

Additional stomatal frequency estimates that are valued semi-quantitatively (Category 2) are those whose (i) measured fossil stomatal values fall outside the range captured in the extant training set (*277*); (ii) where the same cuticles were used to estimate CO_2 using a leaf gas-exchange proxy (*273, 274, 282, 284*), which should yield more quantitative estimates (*22, 305*); or (iii) when estimates are based on fewer than five leaves, which is the minimum level of sampling generally observed to reduce the risk of spurious CO_2 estimates (*307, 308*). This final criterion affects the records of Kürschner et al. (*283*) and Stults et al. (*276*), who did not report the number of leaves analyzed, and parts of several others that measured <5 leaves for some of their data points (*273, 277, 281, 285, 291, 292, 295, 297, 304*). Return to **Table S2**.

3.3. Future directions

In all stomatal proxies, confidence in estimated CO_2 improves when multiple species (*293*) and multiple proxies (*282, 293, 309*) are analyzed. Stomatal frequency and leaf gas-exchange proxies would benefit from comparing paleo-CO_2 estimates from all methods on the same sample material, so that better insight can be gained for their respective strengths and weaknesses. Most importantly, a solid theory needs to be established for why stomatal frequency proxies tend to record low paleo-CO_2 for the Cenozoic relative to other proxies. Most climate models cannot reproduce the temperatures recorded for many parts of the Cenozoic with the paleo-CO_2 estimates of the stomatal frequency proxies (*310*); our current understanding of how the Earth system works does not support such low paleo-CO_2. Intra- and inter-proxy differences need to be mapped out carefully, and it needs to be established whether, e.g., a systematic correction factor could be justified for stomatal frequency proxies. Haworth et al. (*271*) and Elliott-Kingston et al. (*311*) have suggested that the magnitudes of plant developmental and physiological responses to atmospheric CO_2 are contingent on the long-term baseline CO_2 values under which the entire lineage has evolved, which may support the introduction of systematic correction factors. To this end, an IODP cruise to specifically target shallow marine Cenozoic sediments with abundant cuticle material or charcoalified fragments could be a compelling tool for evaluating and comparing stomatal proxies with marine based proxies and high stratigraphic control. The cuticle could be used to compare all aspects of isotope- and stomatal-based proxy methods, and comparison to marine proxies may be possible if abundance, preservation state and air-sea CO_2 equilibrium allow. More advanced plant growth chamber studies under elevated CO_2 atmospheres are also required to tease out limitations of the stomatal proxy and their underlying basis. An important target will be multi-generation studies where first, second and third generation seed produced under different long–term baselines can be evaluated for their capacity to generate robust CO_2 estimates under radically different CO_2 conditions (that is outside their 'evolutionary memory'). Finally, identifying well-preserved fossil plants (ideally with close living relatives) from well-dated (or datable) terrestrial strata, deposited at key intervals during the Cenozoic remains an important goal. Return to **Table S2**.

4. Leaf gas exchange

4.1. Current understanding of the leaf gas-exchange proxies and recent advances

Atmospheric CO_2 estimation based on leaf gas-exchange principles follows a mechanistic model that equates atmospheric CO_2 concentration (c_a) with the ratio of the rate of carbon assimilation

during photosynthesis (A_n, the flux of CO_2 into a leaf in units of µmol m^{-2} s^{-1}) to the product of total leaf diffusive conductance to CO_2 ($g_{c(tot)}$, in units of mol m^{-2} s^{-1}) and the relative CO_2 concentration gradient between atmosphere and leaf interior (1 - c_a/c_i) (*312*):

$$c_a = \frac{A_n}{g_{c(tot)} \times (1 - \frac{c_i}{c_a})} \quad \text{(Eq. 4.1)}$$

Equation 4.1 is a rearrangement of the basic diffusion equation governing A_n during photosynthesis (*159*). For a given relative CO_2 concentration gradient (1-c_i/c_a), higher c_a will be associated with higher A_n and/or lower $g_{c(tot)}$. The rationale behind the leaf gas-exchange proxies is that information about the components of equation 4.1 is preserved in the anatomical and chemical composition of fossil leaves.

There are two major leaf gas-exchange proxies for atmospheric CO_2 (*312, 313*). In both models, the ratio c_i/c_a is determined from measurements of fossil leaf $\delta^{13}C$ along with an estimate of paleoatmospheric $\delta^{13}C$, the latter of which probably varied by ~3‰ across the Cenozoic (*314*). In addition, the stomatal conductance to CO_2—one of the components of total leaf conductance along with boundary layer and mesophyll conductance—is calculated from fossil measurements of stomatal density and stomatal size. The inverse power law behavior between stomatal conductance and atmospheric CO_2 implied in Eq. 4.1 is broadly in keeping with the observations used in the stomatal frequency proxies described in section 3.1.

A_n and the other two components of leaf conductance (boundary layer and mesophyll conductance) cannot be measured directly on fossils. In the Franks et al. (*312*) model, A_n of the fossil leaf specimen referenced to modern c_a (i.e., A_0) is normally inferred from a nearest living relative and scaled to its value at paleo-c_a according to the theory that plants adapt to c_a by optimizing the relative investment of chloroplast protein in light-limited vs. Rubisco capacity-limited photosynthetic reactions (*315*); boundary layer conductance is fixed at a value that is typical for when leaves are photosynthesizing normally; and mesophyll conductance scales with A_n. In the reduced order model of Konrad et al. (*316*), A_n and $g_{c(tot)}$ are determined with a mechanistic model of photosynthesis that requires inputs such as the mitochondrial respiration rate (R_d), maximum rate of rubisco carboxylase activity (Vc_{max}), leaf size, thickness of assimilation tissue and leaf temperature.

The second major leaf gas-exchange proxy is the optimization model of Konrad et al. (*313*). This model assumes that stomatal activity regulates gas exchange in a way that assimilation is maximized and transpiration is minimized. Input parameters include leaf anatomy (available from fossils) and (assumed) values of leaf temperature, air humidity, insolation, and (soil) water availability. Though this model is more comprehensive than the models of Franks et al. (*312*) and Konrad et al. (*316*), it requires a more detailed knowledge of (or more audacious assumptions about) the paleoenvironment. Return to **Table S2**.

4.1.1. Uncertainties and error propagation

For all leaf gas exchange models, the current standard practice for constraining uncertainty in estimated CO_2 is to propagate uncertainties in all of the inputs (both measured and inferred) using Monte Carlo simulations (*282, 312*). Return to **Table S2**.

4.2. Criteria for vetting leaf gas exchange proxy records and data revisions

A total of 18 Cenozoic leaf gas exchange records has been published to date (*274, 275, 282, 284, 293, 312, 317-328*). *Category 3:* We placed the paleo-CO_2 estimates reported in Franks et al. (*312*) into Category 3 because leaf $\delta^{13}C$, which is used to calculate c_i/c_a, was not measured on the same samples from which stomatal dimensions were collected; instead, the authors inferred c_i/c_a via regression from a Phanerozoic compilation. While their CO_2 estimates are broadly consistent with the overall patterns presented here (Figs. 1a and 2a), they possibly contain some error as a result of differences between the regression-derived and directly inferred c_i/c_a values for leaf cuticles, the latter taken to be the standard for this proxy method. Data revisions were applied for several reasons. First, several studies estimated paleo-CO_2 at individual sites from multiple species (*282, 293, 323, 328*). To avoid oversampling of the same time window from a single site, the resampled CO_2 distributions from all species were combined into a single paleo-CO_2 estimate. Second, uncertainty of most estimates generated with the Konrad et al. (*313*) leaf-gas exchange method only include variations in the most sensitive inputs that are not directly measured in fossils. Kowalczyk et al. (*282*) presented a more rigorous alternative, where all inputs—directly measured in fossils and inferred from nearest living relatives—were propagated using Monte Carlo simulations. All estimates from the Konrad approach were revised along these lines (*322, 324, 325*). Return to **Table S2**.

4.3. Future directions

The sensitivity of the input variables on estimated CO_2 is explored extensively elsewhere (*282, 284, 305, 317, 329*). The Franks leaf gas-exchange method is particularly sensitive to two inputs not directly measured on fossils: the assimilation rate at a known CO_2 concentration (A_0) and the ratio between operational and maximum stomatal conductance to CO_2 (i.e., $g_{c(op)}/g_{c(max)}$, or ζ, *284, 329*). Global surveys of woody angiosperm taxa demonstrate generalized scaling relationships between $g_{c(op)}/g_{c(max)}$ (*330*) that broadly support the recommended values originally proposed by Franks et al 2014). However, tests with living plants generally yield more accurate CO_2 estimates when A_0 and $g_{c(op)}/g_{c(max)}$ are measured instead of assumed from recommended values for broad taxonomic groups (*265, 317, 328, 331*). Thus, accuracy in paleo-CO_2 estimates is likely best when based on taxon-specific information of A_0 and $g_{c(op)}/g_{c(max)}$.

As in all stomatal proxies, accuracy in estimated CO_2 improves when based on multiple species (*293, 323*) and multiple proxies (*282, 293*). For example, in a test of the Franks leaf gas-exchange proxy in 40 extant species, estimated CO_2 for individual species ranged between 275 and 850 ppm but the multi-species median was 472 ppm, close to the target concentration of 400 ppm (*305*). Multiple species and multiple proxies should be applied whenever possible. Return to **Table S2**.

5. Liverworts

5.1. Current understanding of the liverwort proxy and recent advances

Liverworts are one of the oldest groups of land plants. They are small in stature, have no tissues to conduct fluids (i.e., no xylem or phloem), and their photosynthetic gametophytic tissue always lacks stomata but typically has pores that remain fixed in size and shape when the epidermal cells are hydrated. Because liverworts lack functional stomata, their CO_2 uptake is controlled by

passive diffusion across cell membranes or through fixed pores. As such, the carbon isotope fractionation during photosynthesis is partly controlled by the amount of atmospheric CO_2, where higher CO_2 allows the plants to be more selective in their carbon assimilation and $\delta^{13}C$ of the plant tissues decreases. Similar to the marine phytoplankton proxy, carbon isotope fractionation is also affected by growth rate. This is accounted for with a photosynthesis model (for details, see *332*) that requires inputs such as irradiance. Return to **Table S2**.

5.2. Criteria for vetting liverwort proxy records and data revisions

Because liverwort fossils are uncommon, the proxy is rarely used - only three estimates have been published in two studies (*282, 333*). The only revision applied to these records is the update of atmospheric $\delta^{13}C$ following Tipple et al. (*314*). Return to **Table S2**.

5.3. Future directions

Similar to the leaf gas-exchange proxies, the leaf assimilation rate is an important input in the liverwort proxy and solar irradiance strongly affects this rate. This is normally not a problem with trees, because sun leaves dominate the fossil record (see *305*), but liverworts grow close to the forest floor. As a result, selecting sites with an interpreted open canopy or habitat is important (*282*) but given the rarity of liverwort fossils, future sampling efforts will likely be limited. Return to **Table S2**.

6. Land Plant $\delta^{13}C$ proxy

6.1. Current understanding of the land plant $\delta^{13}C$ proxy and recent advances

The modern land plant $\delta^{13}C$-based CO_2 proxy is based on a combination of observations of natural trends (e.g., *334, 335*) and experimental studies by Schubert and Jahren (*24*) that related increasing carbon isotope fractionation ($\Delta\delta^{13}C \approx \delta^{13}C_{air} - \delta^{13}C_{plant}$) to increasing atmospheric CO_2. The mechanism for the CO_2 effect on $\Delta\delta^{13}C$ is proposed to reflect carbon isotope fractionation during photorespiration (*336, 337*), a process that occurs when stomata close during hot and dry conditions during the day, and the concentration of O_2 in the leaves exceeds the concentration of CO_2. Under such conditions, formerly fixed glycine is reverted to CO_2 and O_2 is consumed. Photorespiration thus curbs carbon fixation and reduces the efficiency of photosynthesis. Experiments have shown that ^{13}C discrimination during photorespiration decreases the $\delta^{13}C$ of Arabidopsis by a few per mil (Schubert and Jahren, 2018). Photorespiration may have evolved when CO_2 levels were relatively high and oxygen levels exceptionally low (*338-340*).

The accuracy of the land plant $\delta^{13}C$ proxy has been tested using geological materials across the ~100 ppm CO_2 increase from the last glacial to the Holocene, and through analysis of fossil faunas or plant organic matter at (usually) elevated CO_2, but for which CO_2 is known only through other proxies (*341-345*). To minimize the dependency on other paleo-CO_2 proxies, it is recommended to calculate CO_2 concentrations relative to an independent baseline CO_2 value. For instance, for their Deglacial and Neogene reconstructions, respectively, Schubert and Jahren (*341*) and Cui et al. (*346*) calculated CO_2 relative to Holocene ice core measurements of 270 ±7ppm between 11,500 and 100 yrs ago (Method 1). However, using a Holocene baseline is not considered

feasible for deep time studies (e.g., *347*); Cui and Schubert (*348*) therefore used CO_2 estimates from stomatal and paleosol proxies as baseline for deep time studies (i.e., *286, 349, 350*).

Another approach (Method 2) to apply this proxy requires the knowledge of changes in CO_2 (ΔCO_2) across a rapid climate change event (e.g., the PETM and subsequent Early Eocene hyperthermals, *351*) and the difference in the magnitude of carbon isotope excursion (CIE) between the atmosphere and terrestrial organic matter (i.e., $\Delta CIE = CIE_{atm} - CIE_{OM}$). Because ΔCO_2 is often poorly known, or determined by carbon cycle models that require the assumption of a carbon source to determine the amount of carbon added to the Earth system, Method 2 is considered to be qualitative. The sensitivity of the proxy using Method 1 has been evaluated in several studies. An analysis of plant organic matter for the last glacial-Holocene transition suggested good correspondence with ice core measurements (*341*), with a sensitivity of ~2‰ increase in $\Delta^{13}C$ per 100 ppm increase in CO_2, although the reliability of this interpretation has been questioned in the context of other confounding factors (*345*)

Recent experiments (*265, 337, 352-354*) explored additional variables and emphasize three factors that independently contribute to $\Delta\delta^{13}C$: the ratio of atmospheric CO_2 to O_2, the latter of which has also varied through Earth history, water availability, and species or phylogeny (especially spore-producing vs. seed-producing plants, but also conifers vs. angiosperms, see *345, 355*). Other factors that can affect the $\Delta\delta^{13}C$ record include organic matter preservation (e.g., mixing, reworking, or diagenesis) and contributions from isotopically disparate C_4 plants and diatoms (e.g., *356*). While the effects of water availability and plant species on $\delta^{13}C_{plant}$ can be on the order of several per mil (*345, 352, 355*), the effects of variable O_2 are likely small (*265*). Direct measurements from ice cores show a 0.7% decrease in O_2 over the past 800 kyr (*357*), and models of Cenozoic O_2 suggest a range from ~18% to ~24%, with no consensus on trend (see summary by *358*). An uncertainty of ±3% in O_2 would propagate to a CO_2 uncertainty of ~±15%, which is smaller than uncertainties in calculated paleo-CO_2 that arise from annual precipitation and plant species, but still a significant contributor that would benefit from additional research. For instance, modern studies suggest a small CO_2-effect (~0.4‰/100 ppm) for oak (*Quercus*, *359*) and no resolvable CO_2-effect for pine (*Pinus*, *359*), tropical hardwoods (*345*), or ginkgo (*354*). Instead, ginkgo showed changes in other leaf characteristics, rather than $\Delta\delta^{13}C$ (*354*). Analyses of speleothems (*360*), which inherit their $\delta^{13}C$ values from surrounding vegetation, and tree ring cellulose (*343*) support a CO_2 effect across the last deglaciation, albeit smaller than proposed by Schubert and Jahren (*24*): 1.6±0.3‰ and 1.7±1.5‰ per 100 ppm, respectively. Analysis of collagen, which also inherits its $\delta^{13}C$ values from surrounding vegetation, is inconclusive (0.5±1.5‰/100 ppm, *343*). In contrast, sparse studies of Late Cretaceous through Pliocene sedimentary organic matter and tooth enamel of mammals show no clear CO_2 effect on $\Delta\delta^{13}C$, or possibly even a negative effect (-0.4‰/100 ppm) (*342, 344, 345*). However, these studies make corrections for precipitation, which is not always well known, and assume proxy-derived paleo-CO_2 estimates, which are subject to large uncertainties and/or may not coincide exactly in time.

One recent study did not find significant statistical relationship between $\Delta\delta^{13}C$ and CO_2 over short timescales (i.e., decadal to centennial, *361*), while other studies show that carbon isotope fractionation of angiosperms and gymnosperms responds to CO_2 differently, such that $\Delta\delta^{13}C$ is more sensitive to CO_2 in angiosperms (*347, 362*), and the carbon isotope fractionation may be

negatively related to CO_2 at low levels (<400 ppm) (*151, 363*). These conflicting results suggest that further work is needed to better quantify the effect of carbon isotope fractionation in land plants in both laboratory and natural settings.

Several recent studies have reconstructed Cretaceous through Cenozoic paleo-CO_2 including assessments of calibration uncertainty (e.g., *346, 348*). Because the sedimentary record offers a rich archive of organic carbon throughout the Phanerozoic, the land plant $\delta^{13}C$-based CO_2 proxy offers an opportunity to reconstruct paleo-CO_2 at much higher temporal resolution than many other proxies (*364*). In summary, significant progress has been made over the last 10 years to quantify paleo-atmospheric CO_2 from $\Delta\delta^{13}C$ in the fossil remains of C3 land plants, but more work is required to constrain the magnitude of the CO_2 effect, to define deep-time baseline CO_2 values and their effect on the CO_2 reconstruction, to account for variations in local flora that may have different sensitivity to CO_2, and to better understand the controlling mechanisms over geological timescales. Return to **Table S2**.

6.2. Criteria for vetting land plant $\delta^{13}C$ proxy records and data revisions

Because paleo-CO_2 estimates from this proxy change with the selected CO_2 baseline value, these estimates (*293, 341, 346, 348, 365*) are not truly independent of other CO_2 estimates and have therefore been excluded from the paleo-CO_2 compilation used for constraining the Cenozoic CO_2 curve (Fig. 1a), but are shown relative to that curve on Fig. 1b (Category 2). In addition, several revisions have been made relative to original publications. Because data from this proxy were originally published with 68% confidence intervals; these estimates have been recalculated using the R script developed by Cui and Schubert (*348*) and are now reported with propagated 95% confidence intervals. The error propagation includes the uncertainties of calibration equations and of the $\delta^{13}C$ values of organic matter, atmospheric CO_2, and modern leaves. Plant species effects and potential paleo-moisture variability are addressed by increasing the $\delta^{13}C$ uncertainties of fossil organic matter beyond the analytical uncertainty (*365*). Corrections for paleo-O_2 are not applied because this parameter is poorly constrained and proxy sensitivity to this parameter is relatively minor. Diagenesis is also not yet addressed because there is no clear basis for correcting data. In addition, Cui et al. (*365*) reported individual CO_2 estimates of 5-15 replicate analyses of coeval subsamples from the same collection site. To avoid overrepresentation of data from the same samples and time period, these replicate estimates have been averaged and uncertainties are reported as the maximum and minimum 95% confidence limits of the highest and lowest original CO_2 estimates of each sampling interval. Return to **Table S2**.

6.3. Future directions

Improving the land plant $\delta^{13}C$ proxy will require probing in several directions. In particular, previous experiments have been mostly restricted to a constant water regime (*24, 353*). Experiments testing the moisture effect on $\delta^{13}C_{plant}$ often used watering rates in excess (i.e. >950 mm/yr, *352*) of the mean annual precipitation rates that $\delta^{13}C_{plant}$ is most sensitive to (i.e. ≤500 mm/yr, *355, 366*). New experiments are needed to investigate different phylogenetically disparate plant species under environmental and watering regimes that encompass more natural conditions, e.g., in free air experiments (e.g., *354*). Correction for precipitation should be included

and may be estimated using proxies based on water isotopes (e.g., *367*), tree rings (e.g., *368, 369*), leaf fossils (e.g., *370*) and/or organic compounds (*371*). Although independent precipitation proxies are scarce, progress may be possible using other geochemical indices such as paleosol chemistry (*372*) or from new advances in constraining paleoaridity using either isotopic discrimination among sympatric taxa or from multiple isotopes (e.g., *373, 374-376*).

Furthermore, it has been suggested that land plant $\delta^{13}C$ might be sensitive to CO_2 on short timescales, but evolves to show smaller sensitivity on longer, evolutionary, timescales (*345*). Further laboratory, field and geological studies are needed to improve the accuracy and precision of the land plant $\delta^{13}C$ proxy on both short and long evolutionary timescales. The rapid deglacial and anthropogenic CO_2 increases provide excellent opportunities to better quantify the CO_2 effect on recent and short time scales. For deeper-time validation, $\Delta^{13}C$ of fossil faunal and floral remains could be cross-validated against other paleo-CO_2 proxies. Furthermore, and because most observational data are as yet restricted to northern Europe, tests should be conducted in different areas of the world with different species. Analyses of sedimentary organic matter should also be supplemented with information on the preservation state of the studied organic materials, and, if possible, taxonomic specification, so that species-specific fractionation can be taken into account and phylogenetic correction factors applied where applicable (e.g., *353*). Return to **Table S2**.

7. Paleosols

7.1. Current understanding of the paleosol proxy and recent advances

The paleosol carbonate paleo-CO_2 proxy is based on the mixing of CO_2 in soil pore spaces between two endmembers 1) respired CO_2 from plant roots and microbes in the soil and 2) atmospheric CO_2 (Fig. S5, *25, 377*). In the relevant mixing relationship, typically expressed as:

$$CO_{2,atm} = S(z)\left[\frac{\delta_s - 1.0044\delta_r - 4.4}{\delta_a - \delta_s}\right] \quad \text{(Eq.7.1)}$$

there are five variables: 1) the concentration of atmospheric CO_2 ($CO_{2,atm}$) 2) the concentration of CO_2 from soil respiration (S(z)), 3) the $\delta^{13}C$ value of atmospheric CO_2 (δC_a), 4) the $\delta^{13}C$ value of respired CO_2 ($\delta^{13}C_r$, sometimes referred to as soil-respired CO_2 to distinguish from CO_2 respired aboveground) and 5) the $\delta^{13}C$ value of soil CO_2 ($\delta^{13}C_s$, this is the CO_2 mixture that occupies the soil pore spaces). The constants in equation 7.1 account for carbon isotope fractionation that occurs during gas phase diffusion in the soil pore network (Cerling 1984) and are based on well-established theory (*378, 379*). Atmospheric CO_2 concentrations are determined by specifying values of the other four variables. Whereas various approaches have been used over the past 30 years to determine values for S(z), $\delta^{13}C_r$ and $\delta^{13}C_a$ (as reviewed by Breecker 2013) all applications of this proxy determine values for $\delta^{13}C_s$ from measurements of $\delta^{13}C$ values of paleosol carbonates and a temperature-sensitive carbon isotope fraction factor relating $\delta^{13}C$ values of calcite to $\delta^{13}C$ values of CO_2 gas (*177*). In the subsequent paragraphs, we discuss each of these variables, the methods that have been used to determine their values for use in Eq. 7.1 and current understanding of the proxy.

Values of $\delta^{13}C_a$ for use in Eq. 7.1 are based on either the $\delta^{13}C$ of contemporaneous marine carbonates or on the $\delta^{13}C$ of land plants, applying relevant carbon isotope fractionation factors (e.g., *380*). Values of $\delta^{13}C_r$ have been either based on 1) the $\delta^{13}C$ of organic matter from the paleosol of interest, from stratigraphically nearby coal, or from more geographically distant locales, or 2) the $\delta^{13}C$ of marine carbonates from which the $\delta^{13}C$ of atmospheric CO_2 and $\delta^{13}C$ of land plants have been inferred. The sensitivity of C_3 plant $\delta^{13}C$ values to atmospheric CO_2 (see also Section 6 above, e.g., *24, 334*) and rainfall (e.g., *342, 345*) indicate complications associated with calculating atmospheric CO_2 $\delta^{13}C$ values from plant $\delta^{13}C$ values (or vice versa). This is particularly the case since soils that precipitate calcium carbonate are most common in arid – subhumid environments, where plant $\delta^{13}C$ is most sensitive to rainfall. For this same reason, the $\delta^{13}C$ of plants growing in coal swamps may not be representative of plants growing in calcic soils, even if these deposits are stratigraphically close together. Therefore, it is preferable to determine $\delta^{13}C_a$ from marine records and $\delta^{13}C_r$ from organic matter in the paleosol of interest. That said, if multiple variables sensitive to CO_2 can be measured from the same deposits – e.g., $\delta^{13}C$ values of organic carbon and of paleosol carbonate – this would certainly be worthy of exploration, with the understanding that other factors may affect both.

There are also complications associated with using $\delta^{13}C$ of paleosol organic matter as a proxy for $\delta^{13}C_r$. These complications are rooted in the effects of decomposition on the $\delta^{13}C$ values of soil organic matter. For instance, in well-drained modern soils, the $\delta^{13}C$ of organic carbon typically increases with depth by up to 6‰ (Fig. S5, e.g., *381, 382*). Approximately 2‰ of this down-profile $\delta^{13}C$ increase can be explained by the decrease in $\delta^{13}C$ values of atmospheric CO_2 over the past century (i.e., the Suess effect, *383*), leading to organic carbon with lower $\delta^{13}C$ in shallower soils. However, the magnitude of the Suess effect is insufficient to explain the entire down-profile $\delta^{13}C$ increase. In addition, the study of an archived soil core (avoiding most of the Suess effect) shows a relatively small, but non-zero down-profile $\delta^{13}C$ increase (from the A to the B horizon) of approximately 1.5‰ (*384*). These considerations suggest other processes contribute to down-profile $\delta^{13}C$ increases. It has been suggested that soil microbes release CO_2 with a lower $\delta^{13}C$ than the organic carbon they consume (*385, 386*). Although laboratory soil incubations suggest that $\delta^{13}C$ of respired CO_2 is nearly indistinguishable from $\delta^{13}C$ of total organic matter in the top 2 cm of soil where the youngest and freshest organic matter resides (*387*), it is possible that fractionation occurs during metabolism of more recalcitrant organic carbon deeper in soils, contributing to the down-profile $\delta^{13}C$ increase. Although respiration occurs throughout the soil, the organic matter preserved in paleosols is typically from the deeper B horizon, where respiration rates are lower (Fig. S5). Therefore, the organic matter preserved in paleosols probably does not directly reflect the majority of soil respiration which occurred at shallower depths where organic matter $\delta^{13}C$ values are typically lower. Therefore, a small adjustment (currently estimated at -1‰) is probably necessary to determine $\delta^{13}C_r$ from measured $\delta^{13}C$ values of paleosol organic carbon. However, for most paleosols, the uncertainty in the magnitude of this adjustment is strongly overshadowed by uncertainty in the value of S(z) (see below).

Temperatures of paleosol carbonate formation can be determined using the clumped isotope thermometer (*388, 389*). The temperature sensitivity of calculated atmospheric paleo-CO_2 is 4% of the calculated CO_2 per Kelvin. Therefore, a temperature uncertainty of ±3°C results in

reasonably small error. However, soil carbonate formation temperatures determined from modern soils span a few degrees below mean annual air temperature (MAAT) to maximum monthly air temperature (MMAT, *390*). The difference between MAAT and MMAT is large and quantifying temperature of carbonate formation rather than assuming mean annual temperature can make a difference (e.g., compare Ji et al. (*35*) with Heitmann et al. (*391*) and Zhang et al. (*392*) with Huang et al. (*393*), and is recommended when possible (e.g., when samples are not too deeply buried, *26*).

The concentration of CO_2 contributed by soil respiration (S(z)) is the most uncertain variable in Eq. 7.1 and the largest source of error for this proxy. The values for S(z) used in early applications of this proxy ranged between 5000 and 10,000 ppmV and were based on mean growing season CO_2 concentrations in modern soils (*394*). By solving Eq. 7.1 for S(z) and applying to Holocene soils for which atmospheric CO_2 levels are known from ice cores (*395*), Breecker et al. (*396*) suggested average S(z) were closer to 2500 ppmV. Recent advancements (discussed below) have further refined values for S(z) but this variable is still difficult to quantify precisely.

Several advancements to the paleosol carbonate paleo-CO_2 proxy have been made in the past decade. In particular, the Cenozoic record of atmospheric $\delta^{13}C_{CO2}$ (*314*) provides a consistent framework from which paleosol-based studies can extract this necessary constraint for the time period of interest. Several new approaches for estimating S(z) have recently been proposed, including reconstructions based on (i) soil order (*397*), which is recognizable from paleosols and varies with climate and soil parent material, both of which influence soil carbon cycling, (ii) independently reconstructed mean annual precipitation (*398*), (iii) the depth in the soil to the calcium carbonate accumulating horizon (*399*) and (iv) magnetic susceptibility (*36*), which is thought to proxy rainfall in the East Asian Monsoon region (*400*). Although these approaches might allow secular change in S(z) to be resolved, it is clear that more precise estimates are needed and the error associated with these proxies needs to be better quantified (Fig. S6). Of the existing S(z) proxies, magnetic susceptibility has the smallest error but its current calibration is entirely empirical and therefore may only be applicable to soils on the Chinese Loess Plateau.

Uncertainty on the value of S(z) aside, the paleosol CO_2 proxy has a number of advantages. One advantage is that paleosols with calcium carbonate horizons are common in much of the Phanerozoic geologic record. Another is the relative simplicity of the proxy, being possibly void of, or at least relatively immune to, vital effects. A third and perhaps the most significant advantage is that unlike most CO_2 proxies which saturate in the 500 – 1000 ppm range, the paleosol carbonate paleo-CO_2 proxy typically works better at higher CO_2. The better performance at higher CO_2 occurs because uncertainty is reduced when atmospheric CO_2 concentrations and soil-respired CO_2 concentrations are approximately equal to each other (*26*). Appropriate soil-respired CO_2 concentrations (i.e., those that occur during the formation of soil carbonates), although currently difficult to quantify in paleosols (see below), typically range from 400 to several thousand ppm (*397, 398, 401*), meaning that application of this proxy is generally best suited to times periods with atmospheric CO_2 higher than modern. However, paleo respiration rates determine how well a specific paleosol is suited for use with this proxy. Paleosols with lower respiration rates are better suited for periods with low atmospheric CO_2 whereas more productive paleosols are better suited to periods with high CO_2 because the proxy works best

when S(z) and atmospheric CO2 are approximately equal to each other (*402*). This versatility is a specific advantage of this proxy. The suitability of a paleosol (in terms of the comparison between respired CO_2 and atmospheric CO_2 levels) can be determined using Eq. 7.2 below.

$$\frac{CO_2}{S(z)} = \left[\frac{\delta_s - 1.0044\delta_r - 4.4}{\delta_a - \delta_s}\right] \quad \text{(Eq. 7.2)}$$

If the CO_2/S(z) ratio is less than 0.3, then sensitivity of $\delta^{13}C_s$ to atmospheric CO_2 is small because the mixture is dominated by respired CO_2 (i.e., with a little higher or lower atmospheric CO_2 the mixture would still be dominated by respired CO_2, hence the small sensitivity) and the soil should be avoided for the purpose of atmospheric CO_2 reconstruction (*399, 402*). Theoretically, saturation can also occur if soil respiration rates are very low (or atmospheric CO_2 very high), in which case the soil pore spaces would be dominated by atmospheric CO_2 (i.e., paleosol carbonate $\delta^{13}C$ would record $\delta^{13}C_a$ but not atmospheric CO_2 concentration), but that problem has not, to our knowledge, been encountered in nature. Despite the absence, for all practical purposes, of loss of sensitivity at high CO_2, many CO_2 determinations made using this proxy have right (or high CO_2)-skewed probability distributions, resulting from S(z)) distributions that are skewed high and from effects inherent to propagating error through an expression with variables that are multiplied by each other (Eq. 7.1).

As described above, the primary weakness of this proxy is the poor quantification of S(z) values and this is where future work refining this proxy should focus. Another weakness is the uncertainty associated with decomposition effects (including possible microbial fractionation) on the $\delta^{13}C$ of soil organic matter. Error on $\delta^{13}C_r$ has a relatively small effect on CO_2 (Eq. 7.1) that scales with CO_2/S(z). As CO_2/S(z) increases, the difference between $\delta^{13}C_s$ and $\delta^{13}C_r$ increases (Eq. 7.2) and therefore errors on $\delta^{13}C_r$ matter less. But uncertainty about the effect of decomposition on the $\delta^{13}C$ of paleosol organic matter may be more important for time periods when atmospheric CO_2 was relatively low (i.e., the ratio of CO_2/S(z) was small). Carbon isotopic fractionation during microbial respiration is one possible decomposition effect that should be further investigated, particularly in the lower parts of the A and the B horizons of soils (Fig. S5). However, quantifying microbial carbon isotope fractionation in natural soils is difficult because it can be easily conflated with preferential respiration of organic matter of different ages, which can have different carbon isotope compositions due the Suess effect. For instance, preferential respiration of younger organic matter with lower $\delta^{13}C$ could easily be confused with microbial fractionation. Additionally, use of this proxy requires quantification of the depth beneath the paleosurface from which the carbonate sample was acquired or, at minimum, demonstration that samples were acquired from depths at which soil CO_2 concentrations were approximately invarient with depth, i.e., typically taken at >30 cm below the paleosurface. While this can be determined in some cases (e.g., *391, 403*) in many paleosols, this term is difficult to define due to erosion or non-preservation of the tops of soil profiles. This is, however, likely to be only a minor contributor to error in this proxy. A final weakness is the need to correlate marine records of $\delta^{13}C_a$ to values of $\delta^{13}C_s$ and $\delta^{13}C_r$ that are determined from terrestrial deposits. This can introduce error, especially when rapid carbon cycle perturbations are being investigated. Return to **Table S2**.

7.2. Criteria for vetting paleosol proxy records and data revisions

A total of 17 Cenozoic paleosol proxy records has been published to date (*35-37, 42, 349, 350, 392, 393, 398, 399, 404-410*). Three primary criteria were used to vet the paleosol-based records: 1) $\delta^{13}C$ values of respired CO_2 must be determined from $\delta^{13}C$ values of paleosol organic matter; 2) the paleosols must be appropriate for this approach; and 3) S(z) must be estimated with quantifiable uncertainty. The rationale for criterion 1 is the large spatiotemporal variability of vegetation $\delta^{13}C$ values (*355, 366, 411*). The best indicator for $\delta^{13}C$ values of respired CO_2 is the organic matter in the paleosol of interest (ideally occluded within the paleosol carbonate nodules). Enforcing this criterion resulted in five records being placed in Category 3 (*392, 393, 399, 406, 409*). The rationale for the second criterion is that soils with high respiration rates have too small of an atmospheric component in soil CO_2, which results in loss of sensitivity as described above (*402*). Therefore, in practice, some highly productive soils are not appropriate for this approach. We screened the records and removed those for which $CO_2/S(z) < 0.3$ (see above). Enforcing this criterion resulted in two records being placed in Category 3 (*350, 412*), as well as some of the estimates from two additional records (*37, 42*). The rationale for the third criterion is that without error for S(z), the uncertainty of reconstructed atmospheric CO_2 cannot be determined. Enforcing this criterion resulted in two additional records being placed in Category 3 (*349, 404*). One record (*36*) satisfies all three criteria and was placed in category 1. Da et al. (*36*) determined S(z) from magnetic susceptibility, and the calibration and application of this S(z) proxy use soils formed from similar parent material in similar climates, supporting high confidence in quantification.

In order to help evaluate whether or not error is fully quantified in the remaining records, we compared, where possible, CO_2 estimates from the same paleosols using two different methods to determine S(z) (Fig. S6). This was only possible for a few records in the database. We examined some Eocene records (*37, 42*) for which we compared S(z) estimated from 1) soil order (*26, 397*) and 2) mean annual precipitation (MAP, *398*), which was determined from the chemical index of alteration minus potassium (CIA-K, *413*). The soil-order based S(z) values are similar to the smallest S(z) values estimated from MAP and therefore the difference between the two CO_2 estimates for each paleosol increases with increasing MAP. This discrepancy could result from actual sensitivity of S(z) to MAP that is not recorded by soil order and/or it could result from extrapolation beyond the S(z)-MAP calibration curve (*398*). Importantly, for more than half of the paleosols for which the comparison was made there is no overlap of 97.5 and 2.5 percentile error bars. Although agreement between the two proxies is somewhat better during the Miocene (*399*), we conclude that the error associated with S(z) is semi-quantified by soil order and MAP-based proxies and therefore place paleosol records based on these S(z) proxies in Category 2.

Several older records had already been updated in the peer-reviewed literature. Specifically, the uncertainty quantification for Cotton and Sheldon (*398*) was updated by Breecker and Retallack (*399*) and the record originally published by Da et al. (*405*) is superseded by Da et al. (*36*). We also recalculated the original paleo-CO_2 estimates published by Ji et al. (*35*) and Breecker and Retallack (*399*) to provide 97.5 and 2.5 percentile values for CO_2. Records originally published by Hyland & Sheldon (*42*) and Hyland et al. (*37*) were also recalculated. In particular, Hyland et al. (*42*) determined temperature from running means of paleosol carbonate $\delta^{18}O$ values. In our recalculation, we replaced the running means by averaging $\delta^{18}O$ values from the specific paleosol of interest. Both records were also recalculated using the computer program PBUQ (*26*), which

involves updated calculation of $\delta^{13}C_r$ from $\delta^{13}C$ of bulk paleosol organic matter, calculation of calcium carbonate formation temperatures from mean annual temperatures, and an updated regression approach for calculating mean annual precipitation from a commonly employed weathering index (CIA-K, for the original regression see *413*). Return to **Table S2**.

7.3. Future directions

The largest source of error in atmospheric CO_2 reconstructed from paleosol carbonates is associated with the estimation of S(z) (*26*). Disentangling secular changes in soil respiration rates from changes in atmospheric CO_2 levels requires an independent proxy for soil CO_2 and/or pH (*414*). New calibrations for estimating S(z) from magnetic susceptibility (*36*) might be possible for regions outside of the Chinese Loess Plateau with different soil parent material, and several groups are currently working on developing new proxies for quantifying the respiratory contribution to soil CO_2. Alternatively, Eq. 7.1 can be solved for S(z) and measurements in paleosols can then be used with CO_2 determined from other proxies to reconstruct changes in soil respiration (e.g., *415, 416-418*). Ultimately, inversion of forward, process-based models that relate the various measurable quantities in paleosols may be the most useful approach to determining environmental changes that are consistent with all the observations.

Whereas improved precision of S(z) determinations is the single most important direction for the improvement of paleosol carbonate-based CO_2 reconstructions, there are other directions that might also be fruitful to pursue. The use of leaf wax $\delta^{13}C$ values in addition to bulk soil organic matter as a proxy for respired $\delta^{13}C_{CO2}$ would avoid uncertainty associated with decomposition because it would provide insight into paleo-soil carbon cycling. While $\delta^{13}C_r$ is currently the second largest contributor to the uncertainty of paleo-CO_2 estimates from the paleosol proxy, it could become the largest source of error if S(z) estimates are improved. In comparison, $\delta^{13}C_a$ is generally less important than $\delta^{13}C_r$ for paleosol CO_2 estimates, but a high-resolution record of atmospheric $\delta^{13}C_{CO2}$ for the Mesozoic (similar to this recent example for the Creaceous, *419*) and Paleozoic would certainly improve all proxies that rely on this constraint.

The Loess-Paleosol sequence and the underlying Red Clay on the Chinese Loess Plateau is a promising target for future application of the paleosol carbonate proxy (e.g., *35, 36, 405*). The abundant calcic paleosols, good exposure and uniformity of soil parent material through space and time in this region should allow for continuous, high resolution CO_2 records spanning much of the Neogene, including replication across paleoenvironmental gradients. Return to **Table S2**.

8. Nahcolite

8.1. Current understanding of the nahcolite/trona proxy and recent advances

Eugster (*420*) first proposed that estimates of paleo-CO_2 could be made from the sodium carbonate minerals (nahcolite/trona) formed in ancient saline alkaline lakes. The amount of dissolved carbonate and other constituents in a paleolake, the temperature, and the concentration of atmospheric CO_2 in equilibrium with surface brines control which sodium carbonate mineral forms. The nahcolite/trona proxy was reexamined by Lowenstein and Demicco (*28*), who proposed that the layered nahcolite deposits in the early Eocene Green River

Formation, USA, indicate elevated paleo-CO_2 during a well-recognized warm period, the early Eocene climatic optimum (EECO). The nahcolite/trona proxy has since been improved by experiments using seeded reactants and known CO_2 concentrations, which revised the sodium carbonate mineral equilibria (trona, nahcolite, and a third sodium carbonate, natron) as a function of pCO_2 and temperature (*27*). That work constrained the position of the triple point in pCO_2 - temperature space and defined the minimum atmospheric pCO_2 at which nahcolite can form. New modeling of the temperatures and pCO_2 involved in precipitation of layered nahcolite and halite in the Eocene Piceance Creek Basin, Green River Formation, includes coupled summer-winter fluctuations in temperature and variations in total dissolved CO_2 in different parts of the paleolake (*421*). That work confirms that elevated pCO_2 was needed to form nahcolite during the EECO and that paleolake water temperatures in the Green River basin were high, similar to those of the modern Dead Sea. Return to **Table S2**.

8.2. Criteria for vetting nahcolite/trona proxy data and data revisions

The nahcolite/trona proxy requires petrographic study of the sodium carbonate minerals under consideration to ensure that they formed at the surface (air-water interface) of a saline alkaline paleolake and not during burial. The paleo-CO_2 estimates of Lowenstein and Demicco (*28*) have been superseded by Jagniecki et al. (*27*) using their experimental constraints on the nahcolite-trona phase boundary and the nahcolite-trona-natron triple point in pCO_2 - temperature space. Depending on whether the brines contained NaCl and using a possible precipitation temperature range of 19.5-28°C, the lower limit of atmospheric paleo-CO_2 from these minerals can be constrained to 640-1260 µatm. The upper limit of nahcolite precipitation cannot be determined from the nahcolite proxy. In contrast, trona forms at lower pCO_2 than nahcolite and its occurrence in an ancient lake deposit can therefore establish an upper limit of paleo-CO_2. However, because conditions to precipitate trona occur almost throughout the entire Cenozoic, the presence of trona has less value in paleobarometry than the presence of nahcolite. We therefore follow Jagniecki et al. (*27*) and eliminate the trona-based paleo-CO_2 estimates of Lowenstein and Demicco (*28*) from the vetted paleo-CO_2 compilation. Return to **Table S2**.

8.3. Future directions

Paleo-CO_2 estimates of the nahcolite/trona proxy could be improved with the availability of independent data on the lake brine temperatures at which sodium carbonate minerals precipitated, e.g., based on clumped isotopes or the newly developed Brillouin thermometry, which uses femtosecond laser technology for nucleating vapor bubbles in evaporites (*422*). In addition, and although limited in number, there are additional trona/nahcolite lake deposits that have not yet been explored for their suitability as paleo-CO_2 indicators, most notably the late Eocene Anpeng and Wucheng deposits of Henan province, China. Finally, the pCO_2 in modern saline lakes is poorly known, but in some cases, is higher than in the atmosphere (*423, 424*). Understanding the reasons for this air-water disequilibrium and hindcasting such conditions for ancient lakes requires additional limnologic study of modern saline alkaline lakes. Return to **Table S2**.

9. Approximated sample age uncertainty for marine paleo-CO_2 records

Unlike terrestrial records, most publications based on marine sediment records do not estimate or report the age uncertainty. This is a problem that needs to be addressed systematically in the future. If not assessed by the original publications, we use sample ages as reported in the most recent publications and estimate the age uncertainty across marine-sediment-based datasets with a unified approach. We base the estimates on a power-law fit to the uncertainty reported in the LR04 benthic stack (*425*) (0 to 5.3 Ma, **Table** 3), extrapolated over the Cenozoic (Fig. S7). The larger of the power-law fit and the LR04 uncertainties is used. The uncertainties are treated as 1-sigma uniform distributions that are incorporated into the calculation of the Cenozoic CO_2 curve.

The approach used here ensures that comparisons of data from different sites include a reasonable estimate for the uncertainty in their age alignment. Within a site, however, the age uncertainty is applied to all samples such that their stratigraphic ordering and relative spacing are not affected. The true age uncertainty of individual datasets may differ from our simplified approach, however, the lack of a uniform approach to these uncertainties in the literature precludes an individualized approach. Future CO_2 (and really all paleoceonographic) datasets will greatly benefit from projects that provide robust, traceable, and updateable age estimates and uncertainties.

10. Cenozoic CO_2 model

We adapt the Joint Proxy Inversion framework of Bowen et al. (*112*) to estimate the evolution of Cenozoic CO_2 as constrained by the compiled Category 1 proxy data. The model code has been published (*426*). This approach uses inversion of a 2-level Bayesian hierarchical model via Markov Chain Monte Carlo sampling (MCMC) to obtain posterior samples of all model parameters, including paleoenvironmental timeseries. In this case, the first (process) model level represents atmospheric CO_2 levels throughout the Cenozoic, and the second (data) model level represents the relationship between the paleo-CO_2 record and the proxy data compiled here.

Our process model simulates natural log-transformed global atmospheric CO_2 concentrations (C) at 500-kyr time steps from 67 Ma to present (see Fig. S8 for the number of data and proxies in each timestep) using an autocorrelated random walk model, where:

$$C(t) = C(t-1) + \epsilon(t), \text{ and} \quad \text{(Eq. 10.1)}$$

$$\epsilon(t) \sim N[\epsilon(t-1) * \phi, \tau_\epsilon]. \quad \text{(Eq. 10.2)}$$

Here, ϵ is the time-dependent error term (change in C between timesteps). This model has four free parameters: the initial conditions $C(1)$ and $\epsilon(1)$ and error autocorrelation (ϕ) and precision (τ_ϵ, where precision = variance^{-1}). We specify prior distributions for each of these parameters as:

$$\phi \sim U[0.01, 0.99], \quad \text{(Eq. 10.3)}$$

$$\tau_\epsilon \sim \Gamma[1, 0.1], \quad \text{(Eq 10.4)}$$

$$C(1) \sim U[6, 8], \text{ and} \quad \text{(Eq. 10.5)}$$

$$\epsilon(1) \sim N[0, \tau_\epsilon]. \quad \text{(Eq. 10.6)}$$

The error autocorrelation term governs the 'stiffness' of the CO_2 timeseries, leading to greater smoothing of the reconstruction and emphasizing long-term trends at the expense of high-frequency change. Although the importance of long-term (multi-Myr) forcing related to tectonic and biological change as a driver of Cenozoic CO_2 is generally accepted (*427-429*), we also expect important short-term (multi-kyr) events to be expressed in the data. As a result, we adopt a minimally-prescriptive uniform distribution as the prior of the autocorrelation parameter ϕ, allowing this parameter to be optimized to fit the proxy estimates. Error precision defines the distribution of possible values for CO_2 change between adjacent timesteps. We use a broad gamma distribution with a mean that corresponds approximately to a standard deviation of 0.5 for the error term but allows for a broad range of possible values for this parameter. After burn-in the model is minimally sensitive to the priors on $C(1)$ and $\epsilon(1)$, and our choices here are intended to encompass a range of potential values for late Cretaceous CO_2 and possible trajectories for late Cretaceous CO_2 change, respectively.

We incorporate a simple treatment of proxy age uncertainty and local (in space and time) variability to estimate the CO_2 value 'experienced' by each proxy record i (C_i). Age uncertainties can be decomposed into two components: uncertainty associated with the absolute age constraints on a given stratigraphic section or drill hole ('locality'), and those associated with the relative age offset between a sample and the within-section constraints (e.g., due to variations in sediment accumulation rate). Because the age data compiled in our database do not provide a basis for separating these two components, our analysis assumes that the majority of the age uncertainties affecting the samples is associated with the first component and keeps the relative age differences between data from a single locality fixed. We further assume that CO_2 differences between the local, short-term conditions reflected in a given proxy datum and the long-term mean condition modeled by equation 10.1 is drawn from a zero-centered normal distribution with precision τ_l. Thus, for proxy datum i obtained from locality j:

$$C_i \sim N\left[C\left(t\left(a_i + e_j\right)\right), \tau_l\right], \text{ where} \quad \text{(Eq. 10.7)}$$

$$e_j \sim N\left[0, s_j\right], \text{ and} \quad \text{(Eq. 10.8)}$$

$$\tau_\epsilon \sim \Gamma[2, 0.1]. \quad \text{(Eq. 10.9)}$$

Here, a_i is the mean age estimate for the proxy datum and s_j is the average reported age uncertainty (1 standard deviation) for all data associated with locality j. The numeric ages are converted to integers (t = 1, 2, …) that correspond to the process model timesteps within which the ages fall.

In lieu of formal proxy system modeling, our data model uses the interpreted CO_2 reconstructions (and their associated uncertainties) developed by the proxy system working groups. In most cases and for most proxies the upper and lower error estimates are consistent with a log-normally distributed uncertainty, and all values were transformed to ln(CO_2) and used to prescribe a mean estimate (c) and standard deviation (σ, calculated as the half-range of the 5% and 95% confidence intervals / 1.96) for each proxy datum. The likelihood of each observed proxy value c_i is then evaluated relative to the modeled local CO_2 value according to:

$$c_i \sim N[C_i, \sigma_i], \quad \text{(Eq. 10.10)}$$

and the joint likelihood of all proxy data can be calculated for any model state.

We conducted Markov Chain Monte Carlo sampling of the model using the JAGS (Just Another Gibbs Sampler) program (*430*) called from R v4.2.3 (*431*) using the rjags and R2jags packages (*432, 433*). A total of 500,000 posterior samples were obtained in each of 4 chains, including a burn-in period of 50,000 samples; the burn-in samples were discarded and the remaining samples were thinned to retain 2,500 samples per chain. Stability and convergence were assessed using trace plots, effective sample size (N_{eff}), and the Gelman and Rubin convergence diagnostic ($\hat{R}$) (*434*). Values of $\hat{R}$ < 1.1 and N_{eff} ≥ 50 were achieved for all parameters and CO_2 nodes except for the earliest model time steps (representing ages older than the oldest proxy data); values of $\hat{R}$ < 1.03 and N_{eff} ≥ 100 were typical for the CO_2 nodes at most time steps, suggesting strong convergence.

We conducted an independent analysis of global mean surface temperature (GMST) estimates from Westerhold et al. (*43*), calculated after Hansen et al. (*44*). The model form is identical to that described above with the exception that no age model uncertainty was incorporated and that local deviations from the long-term mean were not treated independently from proxy uncertainty (see below). This lack of consideration of age uncertainties is reasonable given that the data come from a limited number of astronomically-tuned deep sea sediment cores and the age uncertainties of individual data are likely to be trivial relative to the 0.5-Myr model time step. Priors on the model parameters were the same as those shown above, with the exception of the error precision and temperature initial value, which were scaled appropriately for the target variable (GMST, expressed as difference relative to the preindustrial value of 14.15, in °C):

$$\tau_\epsilon \sim \Gamma[2,2], \quad \text{(Eq. 10.11)}$$

$$GMST(1) \sim U[5,15]. \quad \text{(Eq. 10.12)}$$

No quantitative estimate of the uncertainty of the individual proxy temperature estimates was provided by the original authors, and for the purpose of our analysis we adopt a normally distributed (and independent) uncertainty with a standard deviation of 4 °C on all data. This value is about an order of magnitude greater than the uncertainty of the species-specific calibration relationships linking temperature and foraminiferal $\delta^{18}O$ (*435*), and is intended to encompass calibration uncertainty, variability in deep-water temperatures over timescales less than the modeled time resolution, and uncertainties in translating the deep-ocean temperatures to GMST. Because the underlying drivers of these uncertainties are generally related to slow and gradual changes in the ocean and climate systems, we suggest that inaccuracies in the corrections are unlikely to substantially affect reconstructed shorter-term (e.g., up to ~10 Myr) changes in GMST, but they may impart some bias to comparisons made across longer time scales. A model that assumes independent errors (such as that used here) cannot account for these potential biases, and our assumed error model is intended only to provide a conservative estimate of the individual temperature estimate generated under the assumptions of the Westerhold et al. (*43*) analysis.

The temperature model achieved satisfactory convergence with 4 chains of 12,000 samples, including a burn-in of 2,000 samples, and the posterior was thinned to retain 2,500 samples per

chain. This produced $\hat{R}$ < 1.02 and an effective sample size ≥ 180 for all model parameters and temperature values, with the exception of temperature values at the first several model time steps (prior to the first data) and a single time step at 36.25 Ma which exhibits slightly poorer convergence ($\hat{R}$ = 1.03, N_{eff} = 110).

10.1. Comparison of data subsets and a**lternative temporal resolutions**

As described and justified here and in the main text, we focus on reconstructing the Cenozoic CO_2 record at a 500-kyr temporal resolution using all available Category 1 data. We also present alternative reconstructions at coarser (1-Myr) and finer (100-kyr) resolutions for comparison with our primary analysis (Fig. S9). The features of these curves are quite similar to those of the 500-kyr curve, but the 1-Myr curve mutes and the 100-kyr curve amplifies the expression of short-term features. The higher-resolution reconstruction may better capture real and meaningful features in some cases (e.g., the PETM, Eocene-Oligocene, Plio-Pleistocene); whereas it accentuates questionable features driven by anomalous or unevenly distributed data (e.g., late Paleocene).

To evaluate the impact of the relatively sparse terrestrial proxy data on the reconstruction, we generated an alternative reconstruction using only boron and alkenone isotope proxy data (Fig. S10). Comparison with the full reconstruction highlights two points. First, during intervals of the Cenozoic when marine proxy data are sparse (most notably the Paleocene) the non-marine records substantially influence the reconstruction. During the Paleocene in particular, the results of the full analysis suggest a decline in CO_2 that is consistent with reconstructed temperature records but is necessarily absent in the curve generated using only marine proxy data. This is because to date, marine proxy data have only been generated for the K/Pg (*234*) and PETM (*60*), and the lack of marine estimates across the Paleocene leads to connecting distant events and erroneously suggesting elevated CO_2 for the duration of the Paleocene (see also *34*). Second, throughout most of the Cenozoic the inclusion of terrestrial proxy records only subtly changes the reconstruction, implying broad consistency between proxy types and increasing confidence in the reconstruction. The differences in Fig. S10 underscore the need to fill in data gaps using both terrestrial and marine proxies.

10.2. When was the last time CO_2 was as high as today?

Using the full posterior suite of 10,000 Cenozoic CO_2 curves from this analysis, we compare the reconstructed values to the average atmospheric CO_2 levels measured in 2022 at the Mauna Loa observatory (419 ppm, *3*) to determine the most recent time in Earth's history that long-term (500-kyr) average CO_2 levels exceeded the current value (Fig. S11). At each timestep in the reconstruction, the probability that atmospheric CO_2 concentrations had exceeded the current level was calculated as the fraction of the reconstructed curves that exceeded 419 ppm at one or more points between that timestep and the present. Using the calibrated language adopted by the IPCC AR6 (*2*), we find that it is exceptionally unlikely (<0.1% chance) that 500-kyr mean CO_2 values exceeded the current atmospheric concentration at any point in the past 8 million years. This probability rises to 5% by 9 Ma, but it remains very unlikely (<10% chance) that long-term mean CO_2 levels ever exceeded the modern value since the middle Miocene (14 Ma). Reconstructed paleo-CO_2 decreases sharply between 15 and 14 Ma, such that it is likely (>66% chance) that 500-kyr mean values exceeded the modern value at some time between 15 Ma and

present.

Fluctuations in atmospheric CO_2 levels, for example those associated with glacial cycles, may have caused paleo-CO_2 levels to briefly exceed the modern concentration more recently than indicated in Fig. S11. To address this issue, we conducted a second analysis in which we used the ensemble of reconstructed CO_2 curves to assess the probability that the change in CO_2 concentration relative to the curve's modern endpoint (representing the mean of the past 500 kyr) had exceeded the change between pre-industrial (i.e., 280 ppm, *436*) and current values (Fig. S12). Because the pre-industrial baseline represents peak interglacial conditions, this analysis should conservatively account for short-term CO_2 variations associated with glacial cycles as long as 1) the amplitude of these cycles in the Miocene and Pliocene did not exceed that of the late Pleistocene cycles (as suggested, e.g., by proxies for ice volume, *437*), and 2) there is no sampling bias towards glacial or interglacial extrema in our proxy records. This analysis suggests that it is exceptionally unlikely that short-term transient CO_2 values exceeded the modern value at any time in the past 4.5 million years, and very unlikely that this situation occurred within the past 7 million years. Short-term CO_2 values exceeding modern remain unlikely (<33% chance) until 9 Ma. However, it is very likely (>90% chance) that transient CO_2 values exceeding the modern value have occurred during the past 14.5 million years.

10.3. Comparison with CO_2 estimates from Hansen et al. (*44*)

We compare the Paleocene-Eocene reconstruction with estimates of CO_2 generated under the assumption that 1) benthic $\delta^{18}O$ values reflect global surface temperature change over this interval, and 2) temperature change results entirely from direct and indirect radiative forcing from CO_2 and linearly increasing solar luminosity (*44*). Throughout most of this interval the proxy-reconstructed values are broadly compatible with the temperature-inferred values estimated using state-dependent climate sensitivity, but the two estimates diverge during the late Eocene (Fig. S13). This is because our proxy estimates suggest that during the cooling leading into the Eocene Oligocene Boundary, CO_2 values declined more slowly than inferred from the temperature proxy data.

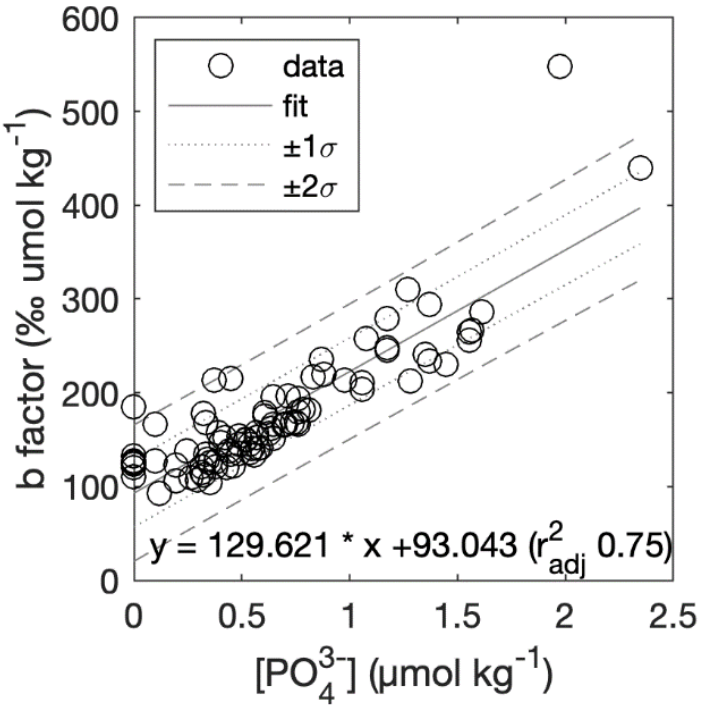

Figure S1: Relationship between phosphate and b in photic zone samples. Data are from the compilation of Hernández-Almeida et al. (*144*). One- and two-sigma confidence bounds are the prediction uncertainty on b that includes both the parameter uncertainty and the data uncertainty in the regression. Note that phosphate values at zero are from Bidigare et al. (*139*) where phosphate was measured as zero with a detection limit of 0.03 µmol/kg.

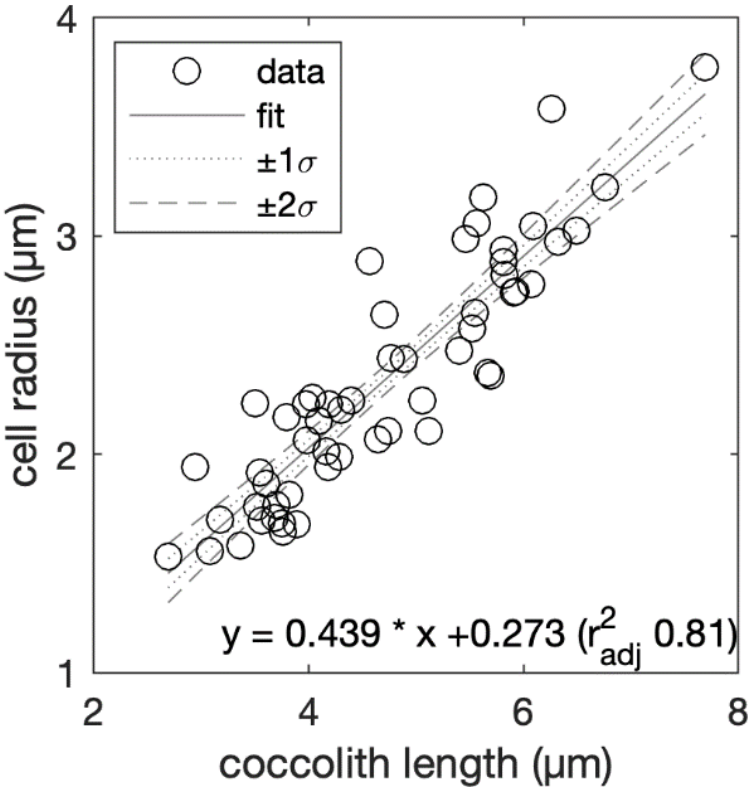

Figure S2: Relationship of coccolith length and cell radius determined from intact individual coccospheres in Cenozoic sediments (after *38*). Confidence bounds are the prediction uncertainty on cell radius that includes only the parameter uncertainty.

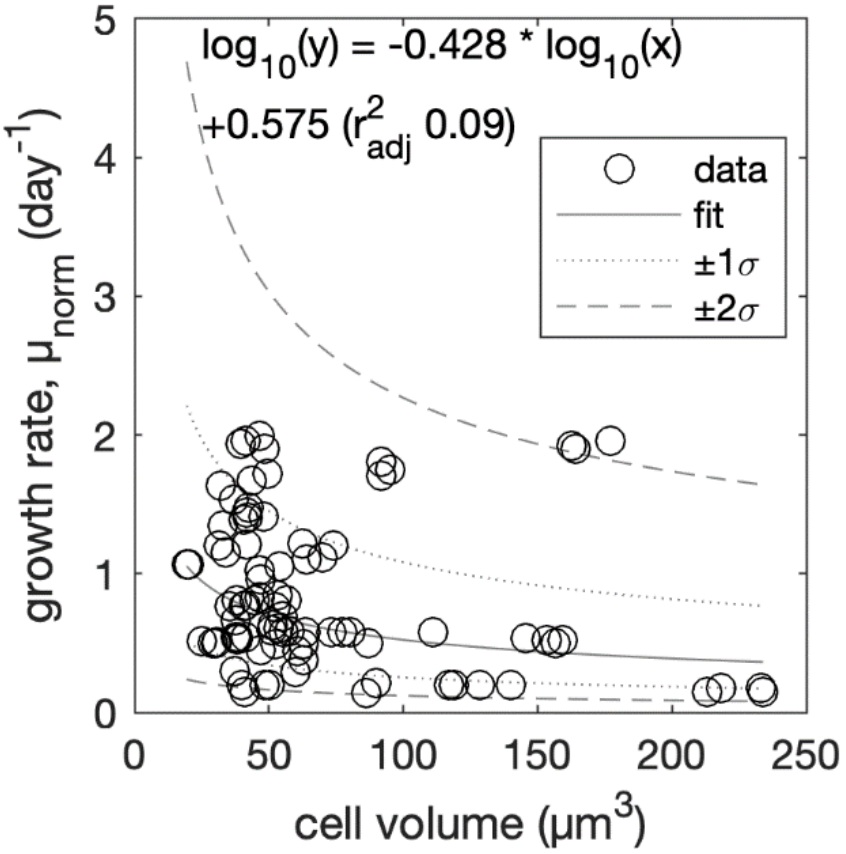

Figure S3: Relationship between cell volume and the logarithm of instantaneous (or normalized) growth rate using data from Aloisi (*157*) as described in Zhang et al. (*41*). One- and two-sigma confidence bounds are the prediction uncertainty on growth rate that includes both the parameter uncertainty and the data uncertainty in the regression.

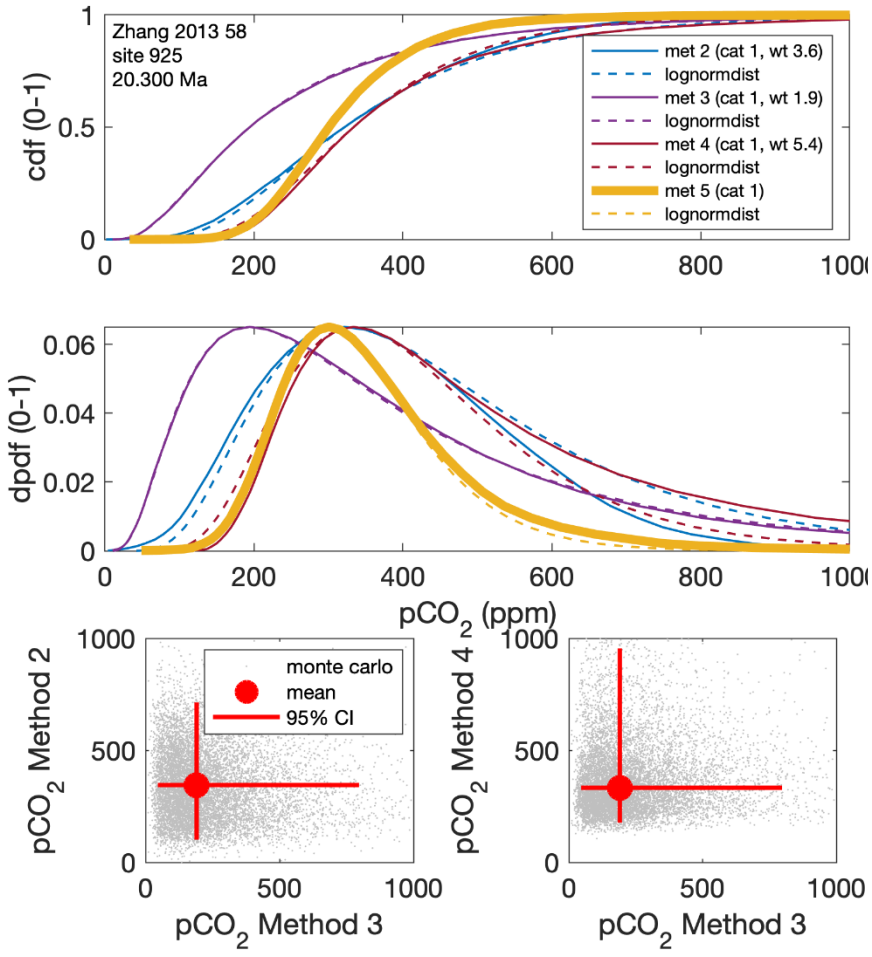

Figure S4: Monte-Carlo *P*CO_2 distributions from Methods 2 to 4 for a single sample. **Top and middle**: Cumulative and discrete probability distribution functions for a sample from ODP site 925 (*108*) illustrating the close approximation of a log-normal distribution (dashed lines) to the Monte-Carlo data (solid lines). 'Method 5' is the inverse-weighted mean as described in the text (weights stated in the legend). **Bottom, left and right:** Monte-Carlo estimates from different methods applied to the same sample (gray dots) with the mean and 95% confidence interval for each method shown in red. The scattered relationship of the Monte Carlo estimates indicates that the different methods are largely independent of each other.

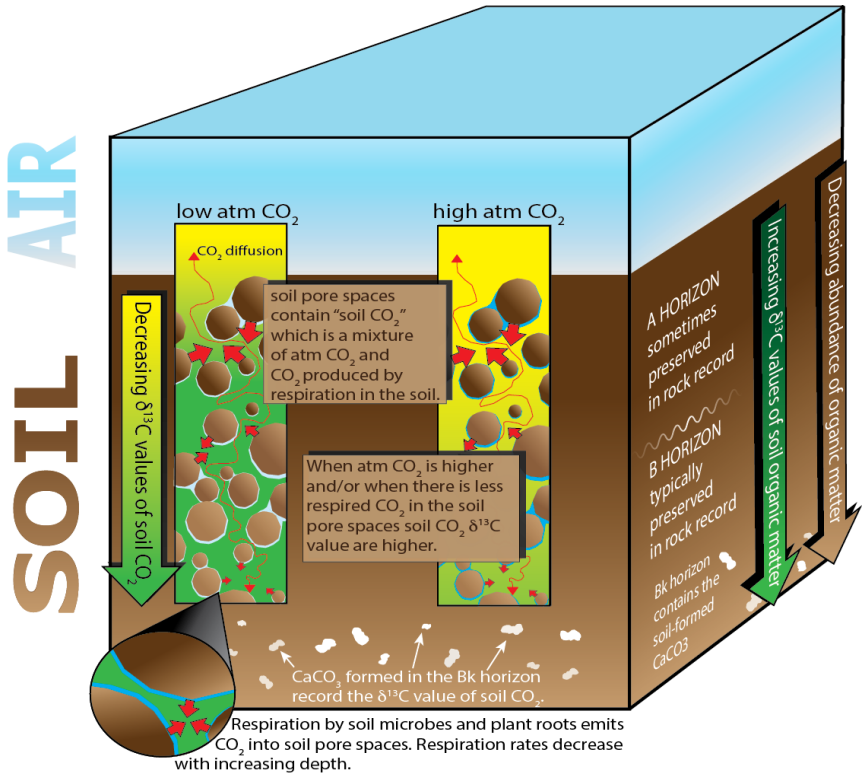

Figure S5: Schematic illustration of processes and gradients relevant to the paleosol carbonate paleo-CO_2 proxy.

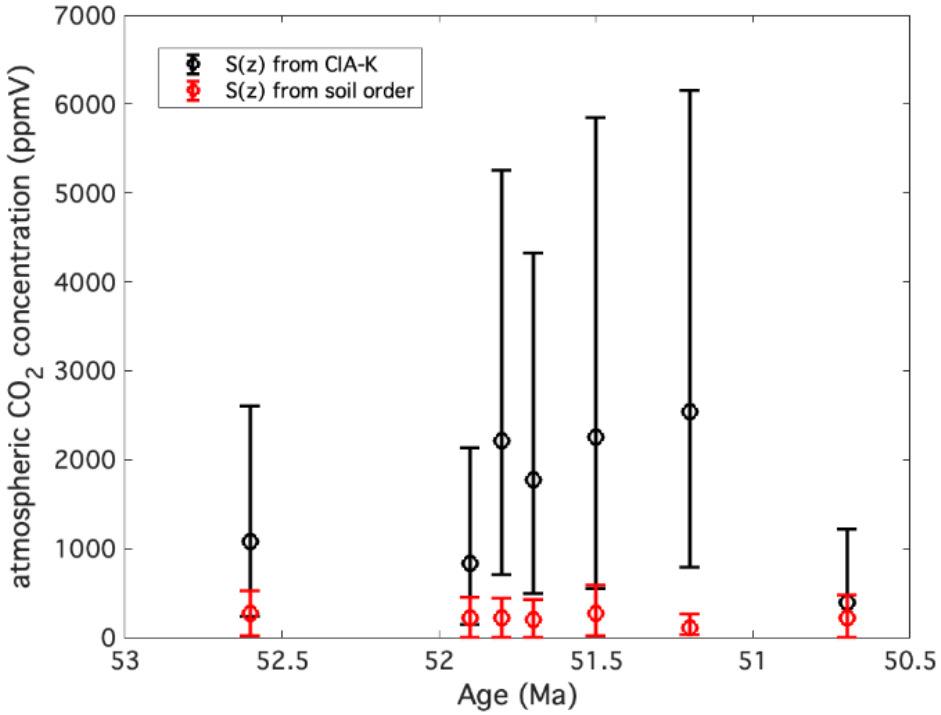

Figure S6:
Comparison of paleo-CO_2 estimates made with the paleosol proxy. The estimates use two different methods to determine S(z) from the same paleosols. The first (black symbols) determines mean annual precipitation (MAP) from CIA-K (*413*) and then infers S(z) from MAP (*398*). The second method (red symbols) estimates S(z) from soil order (*26, 397*). Error bars extend to 2.5 and 97.5 percentiles and were calculated using PBUQ (*26*). Minimal overlap between estimates from the same soil data suggests that S(z) proxies are not fully quantified, which leads us to categorize most paleosol-based CO_2 estimates as Category 2. Data used for this example are from Hyland and Sheldon (*42*) and Hyland et al. (*37*).

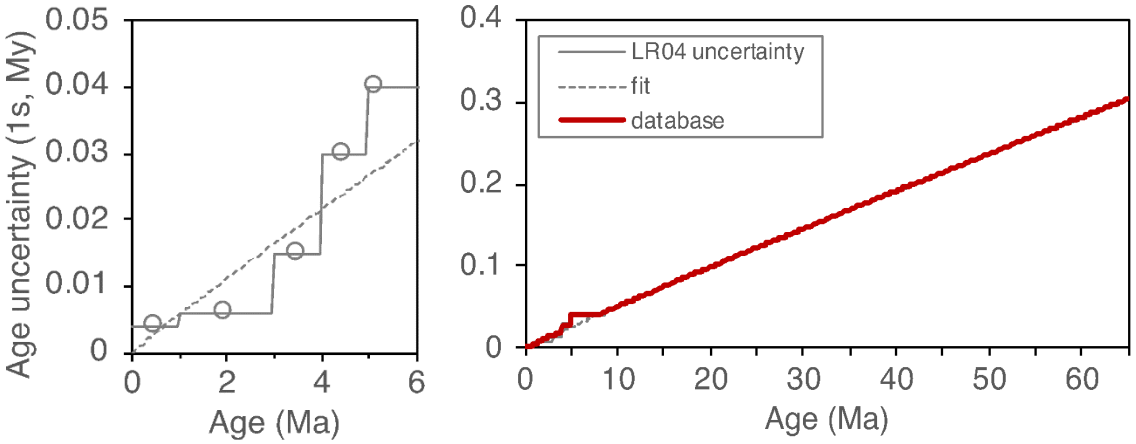

Figure S7: **Left:** The age uncertainty of the LR04 dataset fit with a power law equation ($y = 5.82E\text{-}03x^{9.48E\text{-}01}$). **Right:** The uncertainty applied to samples in the database from the larger of the LR04 uncertainty and power law fit.

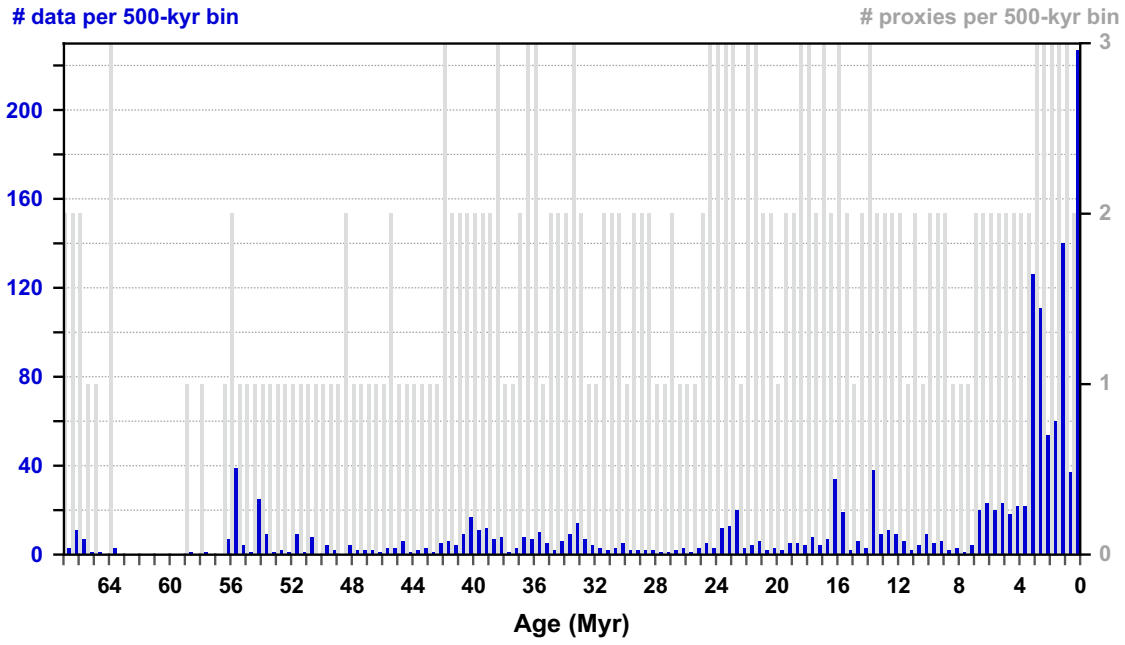

Figure S8: The number of Category-1 paleo-CO_2 estimates (blue) and proxies (grey) in each 500-kyr time step. See Fig. 1a for the proxies applied in each timestep.

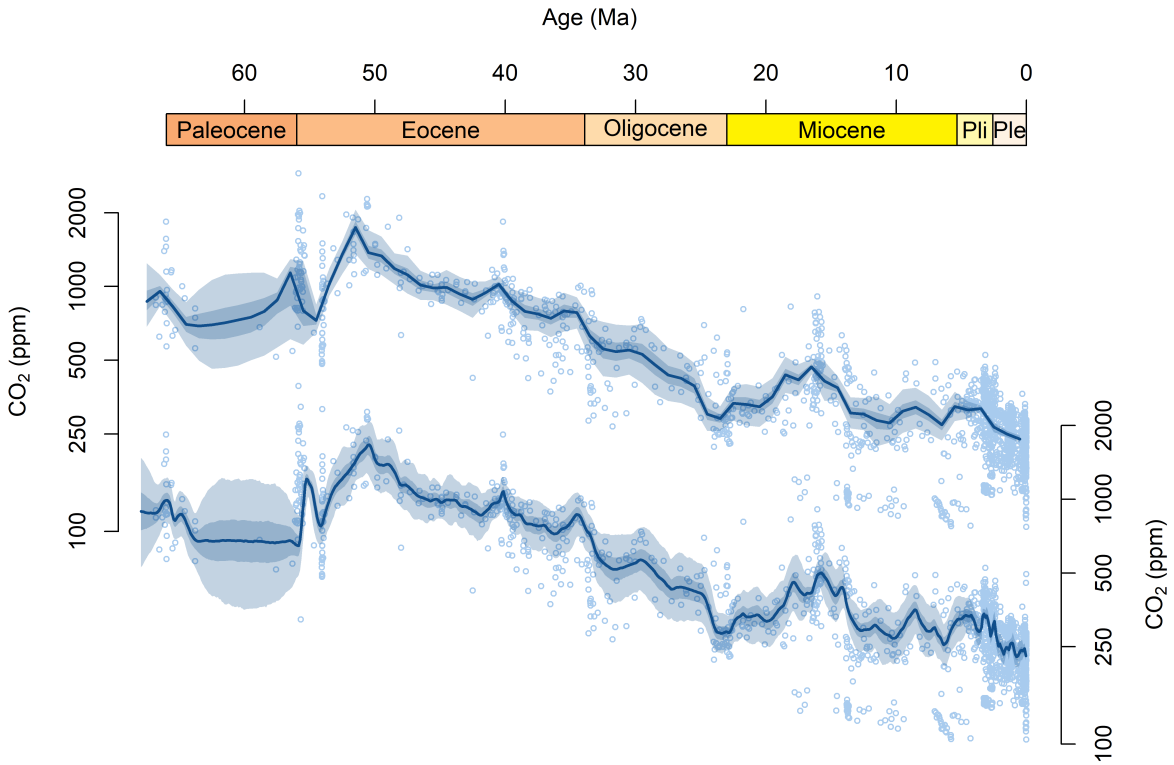

Fig. S9: Alternative Cenozoic CO_2 curves showing reconstructed mean values at 1-Myr (top) and 100-kyr (bottom) intervals.

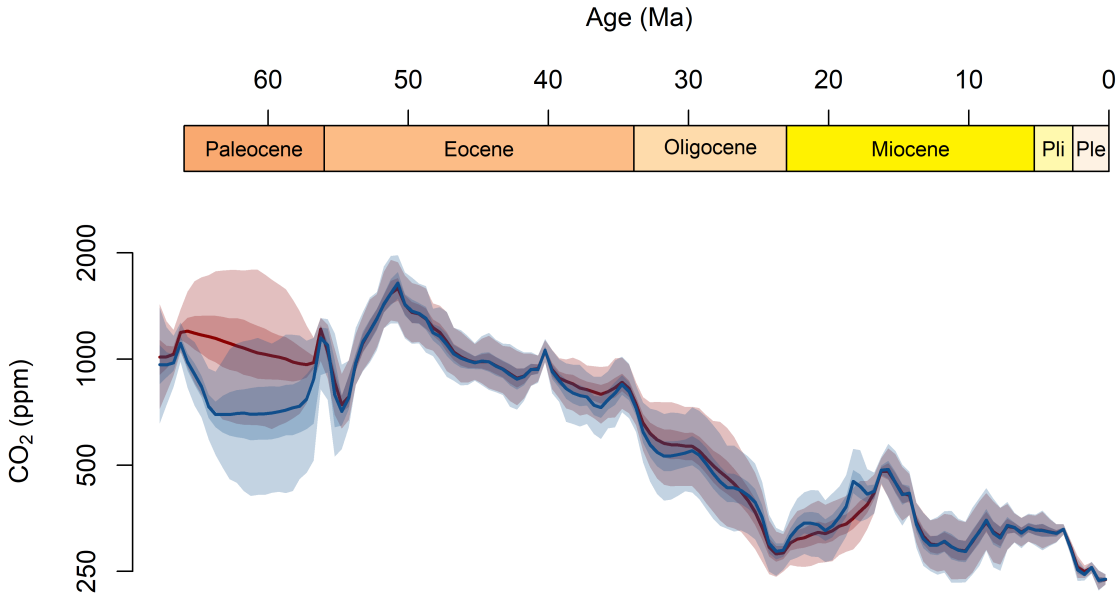

1795

1796 **Figure S10:** Comparison of 500-kyr average CO_2 reconstructions produced using all proxy data (blue) or
1797 only boron and alkenone isotope proxies (red).

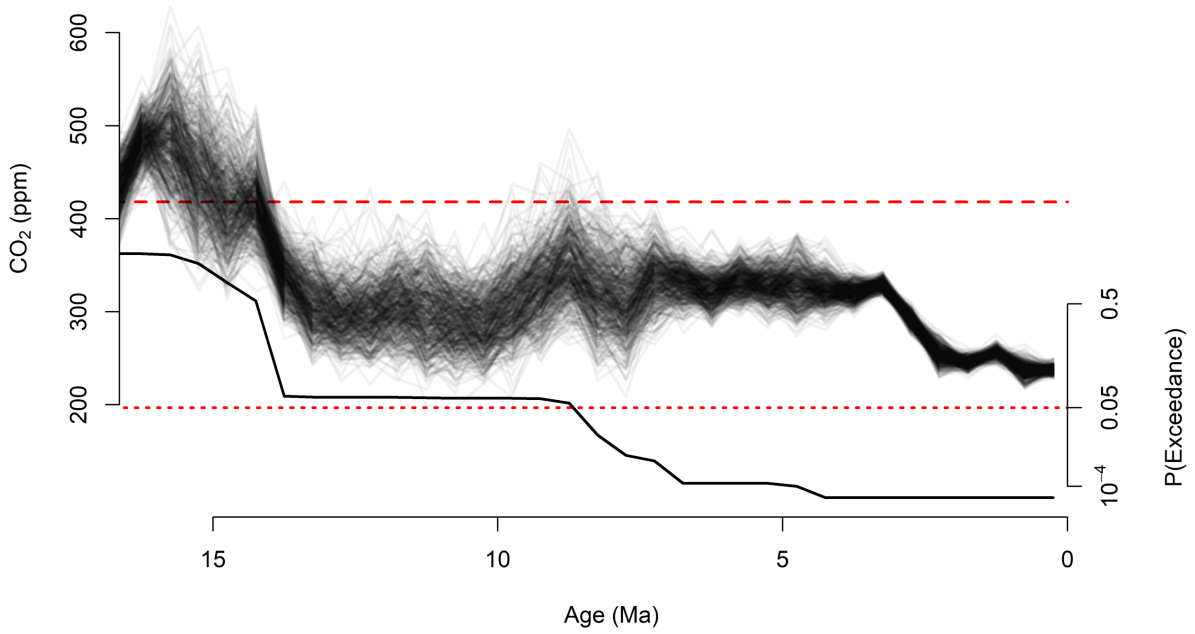

Fig. S11: Comparison of a representative sample of modeled CO_2 curves (thin black lines, top panel) with modern atmospheric CO_2 of 419 ppm (red dashed line, *3*). The bottom panel shows the probability of long-term (500-kyr mean) CO_2 having exceeded the modern value at any time between the plotted time point and the modern based on all 10,000 curves retained in the analysis; dotted red line shows a probability of 5%. The last time this probability was greater than 50% was in the 14.5-14 Ma bin. Note the nonlinear probability scale in the bottom panel.

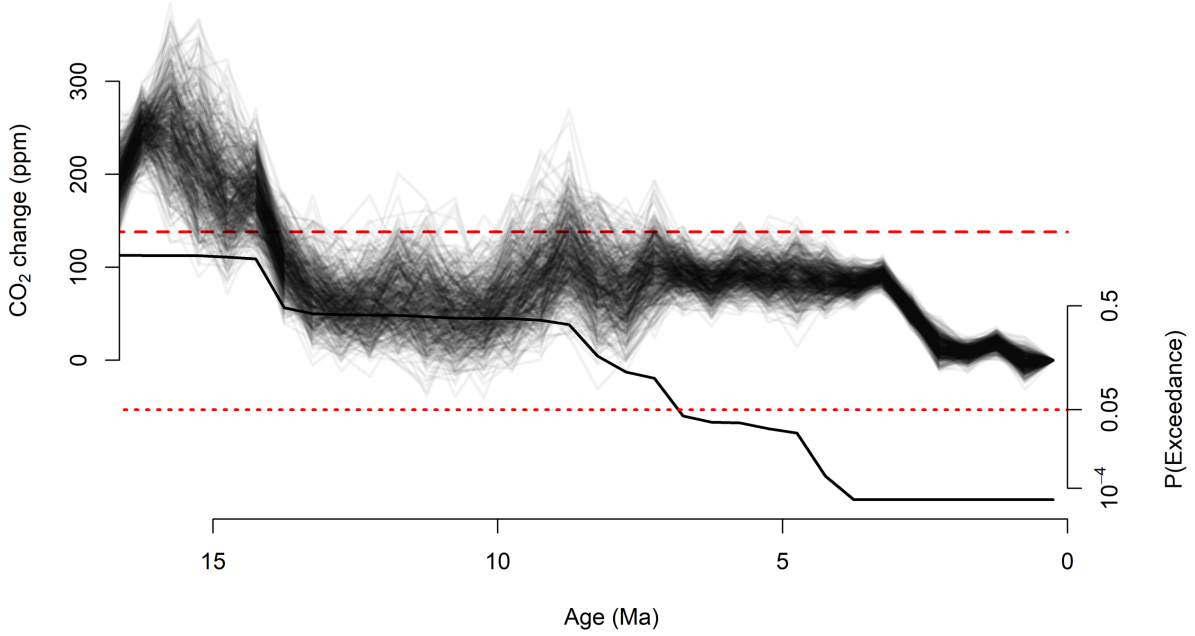

Fig. S12: Comparison of reconstructed CO_2 change relative to the 0.5-0 Ma reference period with CO_2 change between pre-industrial and current values (i.e., 419-280 =139 ppm; red dashed line). The bottom panel shows the probability of long-term (500-kyr mean) CO_2 change having exceeded the post-industrial, anthropogenic change. The thick black line (bottom panel) represents the probability that short-term CO_2 levels exceeded the current value at any time between the plotted time point and the modern, based on all 10,000 curves retained in the analysis. The dotted red line shows a probability of 5%. The last time this probability was greater than 50% was again in the 14.5-14 Ma bin. Note the nonlinear probability scale in the bottom panel.

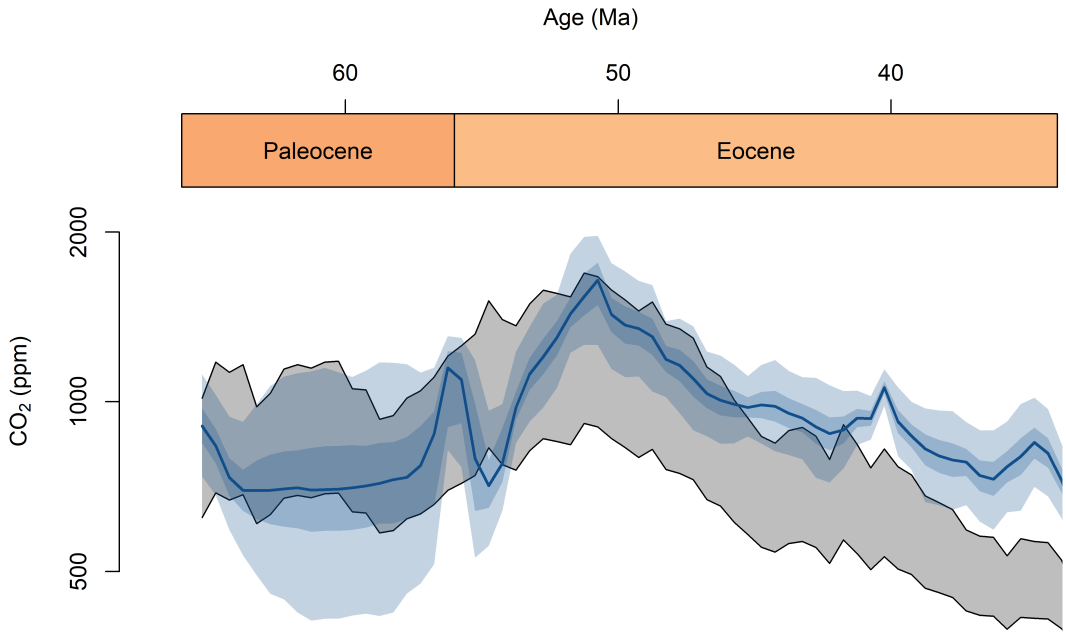

Fig. S13: Paleocene and Eocene CO_2 values from our proxy reconstruction (blue) and from the analysis of Hansen et al. (grey, *44*). The grey envelope encompasses estimates made assuming state-dependent sensitivity to CO_2 forcing (full and 2/3 of the sensitivity calculated using the Russell model) and a surface temperature of 28°C during the Early Eocene Climatic Optimum.

Table S1. Proxy-specific vetting criteria for paleo-CO_2 data categorization.

Data Category	Phytoplankton	Boron Proxies	Stomatal Frequencies, Leaf Gas Exchange Proxies, and Liverworts	Land Plant $\delta^{13}C$	Paleosols	Nahcolite/ Trona
1	All known sources of error have been quantified and/or sensitivity of the CO_2 estimate to those sources is small.					
2	(1) Samples that include all of the data needed to quantify pCO_2 but $[CO_2]_{aq}$ falls outside the calibration range. That range differs between approaches used to calculate pCO_2. In the approach where b is calculated from PO_4, the range is from the minimum and maximum $[CO_2]_{aq}$ in the b-PO_4 calibration dataset. In the approach where CO_2 is calculated from the relative change in ε_p anchored to Pleistocene glacial-interglacial samples, the range is from the minimum and maximum $[CO_2]_{aq}$ values in the laboratory culture experiment that form the calibration dataset. (2) Samples where the organisms contributing to the algal carbon $\delta^{13}C$ value are unknown (e.g., bulk marine organic carbon or biomarkers that lack taxonomic specificity, such as phytol and phytane).	A record that is fully quantified but where estimation of both pH and the second parameter of the marine carbonate system required for estimating CO_2 are not fully independent because both are based on $\delta^{11}B_c$.	(1) All single-species records based on <5 cuticle fragments, unless a statistical analysis shows that fewer than 5 is acceptable. (2) All stomatal ratio records. (3) Estimates based on extrapolation beyond the calibrated range. (4) Estimates whose fossils were also used to estimate CO_2 with leaf gas-exchange methods.	A CO_2 record that is fully quantified but where mean annual precipitation and plant species are not known. As estimates of precipitation and associated uncertainties and plant species become available, the CO_2 record can be better quantified.	CO_2 estimates that satisfy the following three criteria: (1) $\delta^{13}C$ values of paleosol organic matter (or an alternative proxy for local vegetation, e.g., tooth enamel) used to determine $\delta^{13}C_r$. (2) paleosol carbonate $\delta^{13}C$ is sensitive to atmospheric CO_2 level (i.e., $0.3 < CO_2/S(z) < 1.8$). (3) S(z) is semi-quantitative (e.g., estimated from soil order- and MAP-based proxies).	Estimates that quantify the lower limit of atmospheric CO_2, but do not suggest a best estimate or upper limit.

Table S1 continued.

Data Category	Phytoplankton	Boron Proxies	Stomatal Frequencies, Leaf Gas Exchange Proxies, and Liverworts	Land Plant $\delta^{13}C$	Paleosols	Nahcolite/ Trona
3	(1) Samples that are superseded by newer studies where additional or better information was added. For example, alkenone samples where a subsequent study added coccolith size information or improved SST estimates. (2) Samples where measurements of other input variables have subsequently been shown to be in error.	(1) Records that are superseded by improved calculations. (2) Records that applied inadequate cleaning, or used mixed species or morphotypes and/or mixed size fractions. (3) Records based on erroneous proxy theory. (4) Records with inadequate assessment of signal/noise ratio.	(1) All records based on stomatal density. (2) All records based on measurements from published plates. (3) Any record using a transfer function from an extant species that is different from the fossil species, unless broad equivalency in stomatal response can be demonstrated at the genus or family level. (4) Any record whose uncertainties could not be fully propagated in both the calibration function and the fossil measurements (note: we revised estimates using the Beerling et al. (*273*) method whenever possible). (5) Records that are superseded by newer calculations.	N/A	(1) CO_2 estimates that do not meet criteria for Category 1 and do not meet one or more of the criteria for Category 2. (2) Records that are superseded by newer calculations.	Records based on trona, because conditions to precipitate trona occur almost throughout the entire Cenozoic and the presence of this mineral therefore has little value for paleo-barometry.

Table S2. Guide to Sections 1-8. Click on hyperlinks to access respective paragraphs.

Proxy & variables[1] for calculations	Current understanding and recent advances	Data vetting criteria	Calculational methods Key structural uncertainties[2]	Future opportunities
Phytoplankton (ε_P) T, S, $\delta^{13}C_{DIC}$, $\delta^{13}C_{biomass}$, K_H, $[PO_4^{3-}]$, *b*, coccolith length (*L*)	Paragraphs 1.1.; 1.2.1-1.2.4. History of the $\varepsilon_P = \varepsilon_f - b/[CO_2]$ approach; Methods 1, 2, 3, and 4, detailing different approaches to accommodate physiological factors.	Paragraph 1.3. Details for classifying data into Category 1, 2, or 3 (criteria as described in Table S1).	Paragraph 1.4.1-1.4.5. Methods 1, 2, 3, and 4, the approaches to estimate *b*; calculation of weighted-mean pCO_2. Paragraph 1.2.5 Role of diffusion vs. CCMs in algal C budgets; variations in Rubisco ε_f; resulting impact on model structure.	Paragraph 1.5. See text for details.
Boron Isotopes ($\delta^{11}B$) T, S, P, $\delta^{11}B_{SW}$, K_B, K_0, K_1, K_2, K_{HSO4}, Alk or [DIC] or $\Omega_{calcite}$, species-specific calibration	Paragraph 2.1. Background and theory for boron isotope and B/Ca proxies.	Paragraph 2.2. Description of the few select cases where data were excluded from Category 1.	Paragraph 2.1. Equations for translating $\delta^{11}B_{CaCO3}$ to pH. Paragraph 2.1.1. Error propagation; the value of $\delta^{11}B_{sw}$; species-specific calibrations; second parameter of the carbonate system.	Paragraph 2.3. New estimates for $\delta^{11}B_{sw}$; physiological work, cross-calibration, and modeling efforts to better understand vital effects; refined approaches to estimate paleo-alkalinity or DIC.
Stomatal Frequencies T, S, leaf area, epidermal cell density	Paragraph 3.1. Background and definitions of stomatal density, index, and ratio, and their empirical calibration.	Pargraph 3.2. Details for classifying data into Category 2 or 3 (criteria as described in Table S1).	See Table 3 of Beerling and Royer (2002) for examples of the taxon-specific empirical approach. Paragraphs 3.1.1.; 3.2. Statistical simulation of errors; assumption that fossil taxa have same response as plants in the modern calibration.	Paragraph 3.3. Challenges for calibrating fossils to modern sister groups; cross-comparison with estimates of paleo-CO_2 from another proxy of the same age.
Leaf Gas Exchange A_0, g_{op}/g_{max} (or ζ or s4), g_m, g_b, other guard cell scalings (s1-s3); $\delta^{13}C$ of atmospheric CO_2; leaf T	Paragraph 4.1. Background and description of the two major models for leaf gas-exchange, the Franks model and the Konrad model.	Paragraph 4.2. A description of why all CO_2 estimates presented in Franks et al. (*312*) were placed in Category 3.	Paragraph 4.1. Diffusion model for leaf gas exchange. Paragraphs 4.1.1.; 4.3. Uncertainty in photosynthetic rate at a known CO_2 concentration (A_0); operational vs. maximum stomatal conductance to CO_2 (g_{op}/g_{max}); applicability to non-Angiosperm taxa with large stomata and passive stomate control (resulting in high c_i/c_a).	Paragraph 4.3. Calibrate photosynthetic rate using vein density, process-based ecosystem modelling, or nearest living relative or ecological equivalent; apply post-hoc phylogenetic correction factor for plant $\delta^{13}C$; use an assemblage-based approach to paleo-CO_2 estimation.

Proxy & variables[1] for calculations	Current understanding and recent advances	Data vetting criteria	Calculational methods Key structural uncertainties[2]	Future opportunities
Liverworts T, O_2, irradiance; $\delta^{13}C$ of atmospheric CO_2; RubisCO V_{max}; dark respiration (R)	Paragraph 5.1. Diffusional model for CO_2 uptake through fixed pores.	Paragraph 5.2. Explanation for the rarity of liverwort data.	A photosynthesis model (for details, see Fletcher et al., 2006) that requires inputs such as irradiance. Paragraph 5.3. Scarcity of fossils; irradiance through the canopy; accurate $\delta^{13}C$ of local atmospheric CO_2.	Paragraph 5.3. Improvements in estimating forest canopy cover (irradiance) using fossil leaves from vascular plants to determine epidermal cell size and sinuosity; focus on liverworts of unshaded habitats; apply a $\delta^{13}C$ correction based on present-day measurements.
Land Plant $\delta^{13}C$ Calibration parameters A, B, C; $\delta^{13}C_{CO2atm}$ at time t and time 0; $\delta^{13}C_{land\ plant}$ at time t and time 0	Paragraph 6.1. Summary of approaches using an independent baseline or a proxy-derived baseline; overview of calibrations.	Paragraph 6.2. Baseline dependence of calculated result justifies inclusion in Category 2.	see Cui and Schubert (*365*) Paragraph 6.1. Uncertainties in the applicable baseline CO_2 value (for deep time); different responses between evolutionary groups; very large changes in $\Delta\delta^{13}C$ can result in negative CO_2 estimates.	Paragraph 6.3. Additional work needed on moisture effect; cross-group calibrations (pteridophytes, angiosperms and gymnosperms); expanded geographical area for calibrations.
Paleosols S(z); $\delta^{13}C_r$, soil-respired CO_2; $\delta^{13}C_a$, atmospheric CO_2, in-situ T	Paragraph 7.1. Background on soil carbonate formation from mixed respiratory CO_2 and atmospheric CO_2 in soil pore environment.	Paragraph 7.2. Criteria for classification based on estimated CO_2/S(z) ratio and on which proxies were used for carbon isotope compositions of respired CO_2 and S(z); most records placed in Category 2 because common S(z) proxies deemed semiquantitative.	Paragraph 7.1. Eq. 7.1, Eq. 7.2; Sensitivity relationship between proxy response and CO_2/S(z) ratio. Paragraph Return to **Table S2**. **7.3.** Largest error is estimation of S(z), the soil respiration contribution and sensitivity of CO_2/S(z) ratio to this value; uncertainties also in $\delta^{13}C_r$ and $\delta^{13}C_a$ endmember values.	Paragraph 7.3. Opportunities to use soil organic carbon and/or leaf wax $\delta^{13}C$ to improve $\delta^{13}C_r$; develop new soil CO_2 & pH proxies based on fluid inclusions and boron in soil carbonates; need broader geographical distribution of modern measurements; need more estimates of $\delta^{13}C_a$ from benthic foraminifera (*314*) to extend back through the Mesozoic and Paleozoic; develop clumped isotope temperatures of shallow paleosol carbonates.
Nahcolite T, petrographic data	Paragraph 8.1. Explanation of trona-nahcolite-natron equilibria.	Paragraph 8.2. A presence/absence proxy.	Paragraph 8.1. No proxy equation; presence-absence only. Paragraph 8.3. Requires T to refine mineral phase equilibrium; uncertainties in air-water disequilibrium.	Paragraph 8.3. Opportunities to develop clumped isotope temperatures for precipitation of Na-carbonates; prospect for new sample locations.

1. Some or all listed variables may be required, depending on calculation approach; see sections 1-8 for details.
2. Specific to the Cenozoic.

Table S3. Values for $\varepsilon_{\text{biomass/biomarker}}$.

biomarker	*ε (‰)*	*±1σ*	*n*	*references*
$C_{37:2}$ methyl ketone (MK37:2)[(a)]	4.80	0.75	21	Popp et al. (*148*), Riebesell et al. (*438*)
$C_{37:3}$ methyl ketone (MK37:3) [(a)]	4.97	0.67	21	Popp et al. (*148*), Riebesell et al. (*438*)
MK37:3+ MK37:2[(a)]	4.68	0.78	25	Popp et al. (*148*), Riebesell et al. (*438*), Wilkes et al. (*439*)
phytol[(b)]	3.60	1.44	23	Witkowski et al. (*127*) and references therein

(a) mean and standard deviation calculated from all measurements.

(b) ε values averaged for individual species and then the mean and std deviation calculated across species.

118. J. P. Jasper, J. M. Hayes, *Nature* **347**, 462 (1990).
119. K. H. Freeman, J. M. Hayes, *Glob. Biogeochem. Cycle* **6**, 185 (1992).
120. B. N. Popp, R. Takigiku, J. M. Hayes, J. W. Louda, E. W. Baker, *American Journal of Science* **289**, 436 (1989).
121. E. A. Laws, B. N. Popp, R. R. Bidigare, M. C. Kennicutt, S. A. Macko, *Geochim. Cosmochim. Acta* **59**, 1131 (1995).
122. R. François, M. A. Altabet, R. Goericke, D. C. McCorkle, C. Brunet, A. Poisson, *Global Biogeochem. Cycles* **7**, (1993).
123. M. Pagani, K. H. Freeman, N. Ohkouchi, K. Caldeira, *Paleoceanography* **17**, doi: 10.1029/2002PA000756 (2002).
124. G. H. Rau, T. Takahashi, D. J. Des Marais, D. J. Repeta, J. H. Martin, *Geochimica et Cosmochimica Acta* **56**, 1413 (1992).
125. G. H. Rau, T. Takahashi, D. J. D. Marais, *Nature* **341**, 516 (1989/10/01, 1989).
126. M. Pagani, J. C. Zachos, K. H. Freeman, B. Tipple, S. Bohaty, *Science* **309**, 600 (July 22, 2005, 2005).
127. C. R. Witkowski, J. W. H. Weijers, B. Blais, S. Schouten, J. S. Sinninghe Damsté, *Science Advances* **4**, (2018).
128. R. Goericke, J. P. Montoya, B. Fry, in *Stable isotopes in ecology and environmental science,* K. Lajtha, Michener, R.H., Ed. (Blackwell Scientific Publications,, Oxford; Boston, 1994).
129. G. G. B. Tcherkez, G. D. Farquhar, T. J. Andrews, *Proceedings of the National Academy of Sciences* **103**, 7246 (2006).
130. P. G. Falkowski, J. A. Raven, *Aquatic photosynthesis*. (Princeton University Press, Princeton, ed. Second edition, 2007).
131. A. J. Boller, P. J. Thomas, C. M. Cavanaugh, K. M. Scott, *Geochimica et Cosmochima Acta* **75**, 7200 (2011).
132. A. J. Boller, P. J. Thomas, C. M. Cavanaugh, K. M. Scott, *Geobiology* **13**, 33 (2015).
133. S. Burkhardt, U. Riebesell, I. Zondervan, *Geochimica et Cosmochimica Acta* **63**, 3729 (1999).
134. U. Riebesell, S. Burkhardt, A. Dauelsberg, B. Kroon, *Marine Ecology Progress Series* **193**, 295 (2000).
135. B. Rost, I. Zondervan, U. Riebesell, *Limnology and Oceanography* **47**, 120 (Jan, 2002).
136. P. A. Thompson, S. E. Calvert, *Limnology and Oceanography* **40**, 673 (1995).
137. S. C. Brassell, G. Eglinton, I. T. Marlowe, U. Pflaumann, M. Sarnthein, *Nature* **320**, 129 (1986).
138. L. M. Mejía, A. Méndez-Vicente, L. Abrevaya, K. T. Lawrence, C. Ladlow, C. Bolton *et al.*, *Earth and Planetary Science Letters* **479**, 18 (2017/12/01/, 2017).
139. R. R. Bidigare, A. Fluegge, K. H. Freeman, K. L. Hanson, J. M. Hayes, D. Hollander *et al.*, *Global Biogeochem. Cycles* **11**, (1997).
140. M. Pagani, M. Huber, Z. Liu, S. M. Bohaty, J. Henderiks, W. Sijp *et al.*, *Science* **334**, 1261 (December 2, 2011, 2011).
141. M. Pagani, M. A. Arthur, K. H. Freeman, *Paleoceanography* **14**, 273 (1999).

142. B. D. A. Naafs, J. M. Castro, G. A. De Gea, M. L. Quijano, D. N. Schmidt, R. D. Pancost, *Nature Geosci* **9**, 135 (02//print, 2016).
143. R. F. Weiss, *Marine Chemistry* **2**, 203 (1974).
144. I. Hernández-Almeida, K. M. Krumhardt, H. Zhang, H. M. Stoll, *Geochemistry, Geophysics, Geosystems* **21**, e2020GC009272 (2020/11/01, 2020).
145. G. H. Rau, U. Riebesell, D. Wolf-Gladrow, *Marine Ecology Progress Series* **133**, 275 (1996).
146. H. L. O. McClelland, J. Bruggeman, M. Hermoso, R. E. M. Rickaby, *Nature Communications* **8**, 14511 (2017/03/06, 2017).
147. M. H. O'Leary, *The Journal of Physical Chemistry* **88**, 823 (1984).
148. B. N. Popp, E. A. Laws, R. R. Bidigare, J. E. Dore, K. L. Hanson, S. G. Wakeham, *Geochimica et Cosmochimica Acta* **62**, 69 (1998).
149. C. T. Bolton, M. T. Hernandez-Sanchez, M.-A. Fuertes, S. Gonzalez-Lemos, L. Abrevaya, A. Mendez-Vicente *et al.*, *Nat. Commun.* **7**, (01/14/online, 2016).
150. M. P. S. Badger, T. B. Chalk, G. L. Foster, P. R. Bown, S. J. Gibbs, P. F. Sexton *et al.*, *Clim. Past* **15**, 539 (2019).
151. Y. G. Zhang, A. Pearson, A. Benthien, L. Dong, P. Huybers, X. Liu *et al.*, *Geochimica et Cosmochimica Acta* **260**, 177 (2019/09/01/, 2019).
152. S. R. Phelps, H. M. Stoll, C. T. Bolton, L. Beaufort, P. J. Polissar, *Geochemistry, Geophysics, Geosystems* **22**, e2021GC009658 (2021/12/01, 2021).
153. J. Henderiks, M. Pagani, *Earth and Planetary Science Letters* **269**, 575 (2008).
154. Y. G. Zhang, M. Pagani, J. Henderiks, H. Ren, *Earth and Planetary Science Letters* **467**, 1 (6/1/, 2017).
155. P. K. Bijl, A. J. P. Houben, S. Schouten, S. M. Bohaty, A. Sluijs, G.-J. Reichart *et al.*, *Science* **330**, 819 (2010).
156. O. Seki, G. L. Foster, D. N. Schmidt, A. Mackensen, K. Kawamura, R. D. Pancost, *Earth and Planetary Science Letters* **292**, 201 (2010).
157. G. Aloisi, *Biogeosciences* **12**, 4665 (2015).
158. S. Blanco-Ameijeiras, H. M. Stoll, H. Zhang, B. M. Hopkinson, *Journal of Phycology* **56**, 1283 (2020/10/01, 2020).
159. G. D. Farquhar, T. D. Sharkey, *Annual Review of Plant Physiology* **33**, 317 (1982).
160. C. Roeske, M. H. O'Leary, *Biochemistry* **23**, 6275 (1984).
161. E. B. Wilkes, A. Pearson, *Geochimica et Cosmochimica Acta* **265**, 163 (2019/11/15/, 2019).
162. E. A. Laws, R. R. Bidigare, B. N. Popp, *Limnology and Oceanography* **47**, 1552 (1997).
163. N. Andersen, in *Use of Proxies in Paleoceanography - Examples from the South Atlantic,* G. Fischer, G. Wefer, Eds. (Springer, Berlin, Heidelberg, 1999), pp. 469-488.
164. M. P. S. Badger, C. H. Lear, R. D. Pancost, G. L. Foster, T. R. Bailey, M. J. Leng *et al.*, *Paleoceanography* **28**, 42 (2013).
165. M. P. S. Badger, D. N. Schmidt, A. Mackensen, R. D. Pancost, *Philosophical Transactions of the Royal Society A: Mathematical, Physical and Engineering Sciences* **371**, (October 28, 2013, 2013).
166. S. W. Bae, K. E. Lee, K. Kim, *Continental Shelf Research* **107**, 24 (2015/09/15/, 2015).

167. J. P. Jasper, J. M. Hayes, A. C. Mix, F. G. Prahl, *Paleoceanography* **9**, 781 (1994/12/01, 1994).
168. M. Pagani, K. H. Freeman, M. A. Arthur, *Science* **285**, 876 (August 6, 1999, 1999).
169. M. Pagani, Z. Liu, J. LaRiviere, A. C. Ravelo, *Nature Geosci* **3**, 27 (2010).
170. M. Pagani, M. A. Arthur, K. H. Freeman, *Paleoceanography* **15**, 486 (2000/10/01, 2000).
171. M. R. Palmer, G. J. Brummer, M. J. Cooper, H. Elderfield, M. J. Greaves, G. J. Reichart *et al.*, *Earth and Planetary Science Letters* **295**, 49 (2010).
172. J. R. Super, E. Thomas, M. Pagani, M. Huber, C. L. O'Brien, P. M. Hull, *Geology* **46**, 519 (2018).
173. P. J. Müller, G. Kirst, G. Ruhland, I. von Storch, A. Rosell-Mele, *Geochimica et Cosmochimica Acta* **62**, 1757 (May, 1998).
174. J. E. Tierney, M. P. Tingley, *Scientific Data* **2**, 150029 (2015/06/23, 2015).
175. Y. Rosenthal, S. Bova, X. Zhou, *Paleoceanography and Paleoclimatology* **37**, e2022PA004413 (2022/06/01, 2022).
176. W. G. Mook, J. C. Bommerson, W. H. Staverman, *Earth and Planetary Science Letters* **51**, 64 (1974).
177. C. S. Romanek, E. L. Grossman, J. W. Mors, *Geochimica et Cosmochimica Acta* **56**, 419 (1992).
178. L. Beaufort, N. Barbarin, Y. Gally, *Nature Protocols* **9**, 633 (2014/03/01, 2014).
179. L. Beaufort, M. Couapel, N. Buchet, H. Claustre, C. Goyet, *Biogeosciences* **5**, 1101 (2008).
180. E. B. Wilkes, S. J. Carter, A. Pearson, *Geochimica et Cosmochimica Acta* **212**, 48 (2017/09/01/, 2017).
181. B. Rost, U. Riebesell, S. Burkhardt, D. Sültemeyer, *Limnology and Oceanography* **48**, 55 (2003/01/01, 2003).
182. L. T. Bach, L. C. M. Mackinder, K. G. Schulz, G. Wheeler, D. C. Schroeder, C. Brownlee *et al.*, *New Phytologist* **199**, 121 (2013/07/01, 2013).
183. K. Isensee, J. Erez, H. M. Stoll, *Physiologia Plantarum* **150**, 321 (2014/02/01, 2014).
184. H. M. Stoll, P. Ziveri, N. Shimizu, M. Conte, S. Theroux, *Deep Sea Research Part II: Topical Studies in Oceanography* **54**, 581 (2007/03/01/, 2007).
185. M. Hermoso, Y. Candelier, T. J. Browning, F. Minoletti, *GeoResJ* **7**, 35 (2015/09/01/, 2015).
186. A. G. Dickson, *Deep-Sea Res.* **37**, 755 (1990).
187. A. Vengosh, Y. Kolodny, A. Starinsky, A. R. Chivas, M. T. McCulloch, *Geochimica et Cosmochimica Acta* **55**, 2901 (1991).
188. N. G. Hemming, G. N. Hanson, *Geochimica et Cosmochimica Acta* **56**, 537 (1992).
189. K. A. Allen, B. Hönisch, S. M. Eggins, Y. Rosenthal, *Earth and Planetary Science Letters* **351-352**, 270 (2012).
190. K. A. Allen, B. Hönisch, S. M. Eggins, J. M. Yu, H. J. Spero, H. Elderfield, *Earth and Planetary Science Letters* **309**, 291 (Sep, 2011).
191. M. J. Henehan, J. W. B. Rae, G. L. Foster, J. Erez, K. C. Prentice, M. Kucera *et al.*, *Earth and Planetary Science Letters* **364**, 111 (2013).
192. L. L. Haynes, B. Hönisch, K. A. Dyez, K. Holland, Y. Rosenthal, C. R. Fish *et al.*, *Paleoceanography* **32**, 580 (2017).

193. E. L. Howes, K. Kaczmarek, M. Raitzsch, A. Mewes, N. Bijma, I. Horn *et al.*, *Biogeosciences* **14**, 415 (2017).
194. L. L. Haynes, B. Hönisch, K. Holland, Y. Rosenthal, S. M. Eggins, *Earth and Planetary Science Letters* **528**, 115824 (2019/12/15/, 2019).
195. M. J. Henehan, G. L. Foster, J. W. B. Rae, K. C. Prentice, J. Erez, H. C. Bostock *et al.*, *Geochemistry, Geophysics, Geosystems* **16**, 1 (2015).
196. T. L. Babila, Y. Rosenthal, M. H. Conte, *Earth and Planetary Science Letters* **404**, 67 (2014).
197. N. B. Quintana Krupinski, A. D. Russell, D. K. Pak, A. Paytan, *Earth and Planetary Science Letters* **466**, 139 (5/15/, 2017).
198. K. H. Salmon, P. Anand, P. F. Sexton, M. Conte, *Earth and Planetary Science Letters* **449**, 372 (9/1/, 2016).
199. L. L. Haynes, B. Hönisch, *Proceedings of the National Academy of Sciences*, 202003197 (2020).
200. S. M. Sosdian, T. L. Babila, R. Greenop, G. L. Foster, C. H. Lear, *Nature Communications* **11**, 134 (2020/01/09, 2020).
201. T. L. Babila, D. E. Penman, B. Hönisch, D. C. Kelly, T. J. Bralower, Y. Rosenthal *et al.*, *Philosophical Transactions of the Royal Society A: Mathematical, Physical and Engineering Sciences* **376**, (2018).
202. D. T. Harper, B. Hönisch, R. E. Zeebe, G. Shaffer, L. L. Haynes, E. Thomas *et al.*, *Paleoceanography and Paleoclimatology* **35**, e2019PA003699 (2020/02/01, 2020).
203. D. E. Penman, B. Hönisch, R. E. Zeebe, E. Thomas, J. C. Zachos, *Paleoceanography* **29**, 2014PA002621 (2014).
204. A. Sanyal, N. G. Hemming, G. N. Hanson, W. S. Broecker, *Nature* **373**, 234 (1995).
205. P. N. Pearson, M. R. Palmer, *Nature* **406**, 695 (2000).
206. F. J. Millero, *Geochimica Cosmochimica Acta* **59**, 661 (1995).
207. K. Klochko, A. J. Kaufman, W. Yao, R. H. Byrne, J. A. Tossell, *Earth and Planetary Science Letters* **248**, 261 (2006).
208. O. Nir, A. Vengosh, J. S. Harkness, G. S. Dwyer, O. Lahav, *Earth and Planetary Science Letters* **414**, 1 (2015).
209. M. P. Hain, G. L. Foster, T. Chalk, *Paleoceanography and Paleoclimatology* **33**, 1099 (2018).
210. M. P. Hain, D. M. Sigman, J. A. Higgins, G. H. Haug, *Glob. Biogeochem. Cycle* **29**, 517 (2015).
211. R. E. Zeebe, T. Tyrrell, *Geochimica et Cosmochimica Acta* **257**, 373 (2019/07/15/, 2019).
212. E. Anagnostou, E. H. John, K. M. Edgar, G. L. Foster, A. Ridgwell, G. N. Inglis *et al.*, *Nature* **533**, 380 (05/19/print, 2016).
213. B. Hönisch, N. G. Hemming, *Paleoceanography* **19**, doi:10.1029/2004PA001026 (2004).
214. A. Sanyal, J. Bijma, H. J. Spero, D. W. Lea, *Paleoceanography* **16**, 515 (2001).
215. G. L. Foster, *Earth and Planetary Science Letters* **271**, 254 (2008).
216. M. Guillermic, S. Misra, R. Eagle, A. Villa, F. Chang, A. Tripati, *Biogeosciences* **17**, 3487 (2020).
217. M. J. Henehan, G. L. Foster, H. C. Bostock, R. Greenop, B. J. Marshall, P. A. Wilson, *Earth and Planetary Science Letters* **454**, 282 (11/15/, 2016).

218. B. Hönisch, J. Bijma, A. D. Russell, H. J. Spero, M. R. Palmer, R. E. Zeebe *et al.*, *Mar. Micropaleontol.* **49**, 87 (2003).
219. M. A. Martínez-Botí, G. Marino, G. L. Foster, P. Ziveri, M. J. Henehan, J. W. B. Rae *et al.*, *Nature* **518**, 219 (2015).
220. M. Raitzsch, J. Bijma, A. Benthien, K.-U. Richter, G. Steinhoefel, M. Kučera, *Earth and Planetary Science Letters* **487**, 138 (4/1/, 2018).
221. J. Yu, D. J. R. Thornalley, J. W. B. Rae, N. I. McCave, *Paleoceanography*, n/a (2013).
222. R. E. Zeebe, D. A. Wolf-Gladrow, J. Bijma, B. Hönisch, *Paleoceanography* **18**, 1 (2003).
223. B. Hönisch, C. R. Fish, S. R. Phelps, L. L. Haynes, K. Dyez, K. Holland *et al.*, *Paleoceanography and Paleoclimatology* **36**, e2020PA004022 (2021/10/01, 2021).
224. B. Hönisch, N. G. Hemming, *Earth and Planetary Science Letters* **236**, 305 (2005/7/30, 2005).
225. K. A. Dyez, B. Hönisch, G. A. Schmidt, *Paleoceanography and Paleoclimatology* **33**, (2018).
226. R. Greenop, S. M. Sosdian, M. J. Henehan, P. A. Wilson, C. H. Lear, G. L. Foster, *Paleoceanography and Paleoclimatology* **0**, (2019/01/18, 2019).
227. T. B. Chalk, G. L. Foster, P. A. Wilson, *Earth and Planetary Science Letters* **510**, 1 (2019/03/15/, 2019).
228. A. K. Tripati, C. D. Roberts, R. A. Eagle, *Science*, 1178296 (October 8, 2009, 2009).
229. G. Bartoli, B. Hönisch, R. E. Zeebe, *Paleoceanography* **26**, PA4213 (2011).
230. T. B. Chalk, M. P. Hain, G. L. Foster, E. J. Rohling, P. F. Sexton, M. P. S. Badger *et al.*, *Proceedings of the National Academy of Sciences*, (November 27, 2017, 2017).
231. E. de la Vega, T. B. Chalk, P. A. Wilson, R. P. Bysani, G. L. Foster, *Scientific Reports* **10**, 11002 (2020/07/09, 2020).
232. G. L. Foster, C. H. Lear, J. W. B. Rae, *Earth and Planetary Science Letters* **341-344**, 243 (2012).
233. R. Greenop, G. L. Foster, P. A. Wilson, C. H. Lear, *Paleoceanography* **29**, 2014PA002653 (2014).
234. M. J. Henehan, A. Ridgwell, E. Thomas, S. Zhang, L. Alegret, D. N. Schmidt *et al.*, *Proceedings of the National Academy of Sciences*, 201905989 (2019).
235. B. Hönisch, N. G. Hemming, D. Archer, M. Siddall, J. F. McManus, *Science* **324**, 1551 (Jun 19, 2009).
236. M. A. Martínez-Botí, G. L. Foster, T. B. Chalk, E. J. Rohling, P. F. Sexton, D. J. Lunt *et al.*, *Nature* **518**, 49 (2015).
237. P. N. Pearson, G. L. Foster, B. S. Wade, *Nature* **461**, 1110 (Oct, 2009).
238. M. Raitzsch, J. Bijma, T. Bickert, M. Schulz, A. Holbourn, M. Kučera, *Clim. Past* **17**, 703 (2021).
239. S. M. Sosdian, R. Greenop, M. P. Hain, G. L. Foster, P. N. Pearson, C. H. Lear, *Earth and Planetary Science Letters* **498**, 362 (2018/09/15/, 2018).
240. L. B. Stap, B. de Boer, M. Ziegler, R. Bintanja, L. J. Lourens, R. S. W. van de Wal, *Earth and Planetary Science Letters* **439**, 1 (2016/04/01/, 2016).
241. K. A. Allen, B. Hönisch, *Earth and Planetary Science Letters* **345-348**, 203 (2012).
242. M. Guillermic, S. Misra, R. Eagle, A. Tripati, *Clim. Past* **18**, 183 (2022).

243. S. T. Brennan, T. K. Lowenstein, D. I. Cendón, *American Journal of Science* **313**, 713 (October 1, 2013, 2013).
244. J. Horita, H. Zimmermann, H. D. Holland, *Geochim. Cosmochim. Acta* **66**, 3733 (2002).
245. H. Pälike, M. W. Lyle, H. Nishi, I. Raffi, A. Ridgwell, K. Gamage *et al.*, *Nature* **488**, 609 (08/30/print, 2012).
246. R. Greenop, M. P. Hain, S. M. Sosdian, K. I. C. Oliver, P. Goodwin, T. B. Chalk *et al.*, *Clim. Past* **13**, 149 (2017).
247. S. O. R. K. H. C. Spezzaferri, *Cushman Foundation for Foraminiferal Research Special Publication* **46**, 269 (2018).
248. D. E. Gaskell, P. M. Hull, *Geology* **47**, 1156 (2019).
249. H. Takagi, K. Kimoto, T. Fujiki, A. Kurasawa, K. Moriya, H. Hirano, *Marine Micropaleontology* **122**, 44 (1//, 2016).
250. H. Takagi, K. Kimoto, T. Fujiki, H. Saito, C. Schmidt, M. Kucera *et al.*, *Biogeosciences* **16**, 3377 (2019).
251. J. E. Burke, W. Renema, M. J. Henehan, L. E. Elder, C. V. Davis, A. E. Maas *et al.*, *Biogeosciences* **15**, 6607 (2018).
252. P. N. Pearson, M. R. Palmer, *Science* **284**, 1824 (1999).
253. M. Raitzsch, B. Hönisch, *Geology* **41**, 591 (May 1, 2013, 2013).
254. G. Paris, J. Gaillardet, P. Louvat, *Geology* **38**, 1035 (November 1, 2010, 2010).
255. D. Lemarchand, J. Gaillardet, É. Lewin, C. J. Allègre, *Nature* **408**, 951 (2000).
256. D. Lemarchand, J. Gaillardet, E. Lewin, C. J. Allegre, *Chem. Geol.* **190**, 123 (2002/10/30, 2002).
257. L. Simon, C. Lécuyer, C. Maréchal, N. Coltice, *Chem. Geol.* **225**, 61 (2006).
258. T. K. Lowenstein, B. Kendall, A. D. Anbar, in *Treatise on Geochemistry (Second Edition),* H. D. Holland, K. K. Turekian, Eds. (Elsevier, Oxford, 2014), pp. 569-622.
259. A. Ridgwell, R. E. Zeebe, *Earth and Planetary Science Letters* **234**, 299 (2005/6/15, 2005).
260. R. E. Zeebe, P. Westbroek, *Geochem. Geophys. Geosyst.* **4**, (Dec, 2003).
261. N. S. Lloyd, A. Y. Sadekov, S. Misra, *Rapid Communications in Mass Spectrometry* **32**, 9 (2018/01/15, 2018).
262. A. Sadekov, N. S. Lloyd, S. Misra, J. Trotter, J. D'Olivo, M. McCulloch, *Journal of Analytical Atomic Spectrometry*, (2019).
263. C. D. Standish, T. B. Chalk, T. L. Babila, J. A. Milton, M. R. Palmer, G. L. Foster, *Rapid Communications in Mass Spectrometry* **33**, 959 (2019/05/30, 2019).
264. D. Evans, A. Gerdes, D. Coenen, H. R. Marschall, W. Müller, *Journal of Analytical Atomic Spectrometry* **36**, 1607 (2021).
265. A. S. Porter, C. E. Gerald, C. Yiotis, I. P. Montanez, J. C. McElwain, *Geochimica et Cosmochimica Acta* **259**, 69 (2019).
266. R. S. Barclay, J. C. McElwain, B. B. Sageman, *Nat. Geosci.* **3**, 205 (2010).
267. M. Steinthorsdottir, A. J. Jeram, J. C. McElwain, *Palaeogeography, Palaeoclimatology, Palaeoecology* **308**, 418 (2011).
268. J. C. McElwain, F. E. Mayle, D. J. Beerling, *Journal of Quaternary Science* **17**, 21 (2002/01/01, 2002).
269. M. Steinthorsdottir, H. K. Coxall, A. M. de Boer, M. Huber, N. Barbolini, C. D. Bradshaw *et al.*, *Paleoceanography and Paleoclimatology* **36**, e2020PA004037 (2020/12/23, 2021).

270. M. Haworth, C. Elliott-Kingston, J. C. McElwain, *Journal of Experimental Botany* **62**, 2419 (2011).
271. M. Haworth, J. Heath, J. C. McElwain, *Annals of Botany* **105**, 411 (2010).
272. M. Haworth, D. Killi, A. Materassi, A. Raschi, *American Journal of Botany* **102**, 677 (2015).
273. D. J. Beerling, A. Fox, C. W. Anderson, *American Journal of Science* **309**, 775 (2009).
274. J.-Q. Liang, Q. Leng, D. F. Höfig, G. Niu, L. Wang, D. L. Royer *et al.*, *Glob. Planet. Change* **209**, 103737 (2022/02/01/, 2022).
275. J.-q. Liang, Q. Leng, L. Xiao, D. F. Höfig, D. L. Royer, Y. G. Zhang *et al.*, *Review of Palaeobotany and Palynology* **305**, 104743 (2022/10/01/, 2022).
276. D. Stults, F. Wagner-Cremer, B. Axsmith, *Atmospheric paleo-CO 2 estimates based on Taxodium distichum (Cupressaceae) fossils from the Miocene and Pliocene of Eastern North America*. (2011), vol. 309.
277. R. S. Barclay, S. L. Wing, *Earth and Planetary Science Letters* **439**, 158 (2016/04/01/, 2016).
278. D. J. Beerling, B. H. Lomax, D. L. Royer, G. R. Upchurch, L. R. Kump, *Proc. Natl. Acad. Sci. U. S. A.* **99**, 7836 (Jun, 2002).
279. D. J. Beerling, *Proceedings of the National Academy of Sciences USA* **99**, 12567 (2002).
280. G. Doria, D. L. Royer, A. P. Wolfe, A. Fox, J. A. Westgate, D. J. Beerling, *American Journal of Science* **311**, 63 (2011).
281. D. R. Greenwood, M. J. Scarr, D. C. Christophel, *Palaeogeography, Palaeoclimatology, Palaeoecology* **196**, 375 (2003).
282. J. B. Kowalczyk, D. L. Royer, I. M. Miller, C. W. Anderson, D. J. Beerling, P. J. Franks *et al.*, *Paleoceanography and Paleoclimatology* **33**, 1427 (2018/12/01, 2018).
283. W. M. Kürschner, F. Wagner, D. L. Dilcher, H. Visscher, in *Geological Perspectives of Global Climate Change,* L. C. Gerhard, W. E. Harrison, B. M. Hanson, Eds. (The American Association of Petroleum Geologists, Tulsa, 2001), vol. APPG Studies in Geology 47, pp. 169-189.
284. D. P. Maxbauer, D. L. Royer, B. A. LePage, *Geology* **42**, 1027 (2014).
285. G. J. Retallack, *Geological Society of America Bulletin* **121**, 1441 (2009).
286. D. L. Royer, R. A. Berner, D. J. Beerling, *Earth-Sci. Rev.* **54**, 349 (2001).
287. D. L. Royer, in *Causes and Consequences of Globally Warm Climates in the Early Paleogene,* S. L. Wing, P. D. Gingerich, B. Schmitz, E. Thomas, Eds. (Geological Society of America Special Paper 369, Boulder, 2003), vol. 369, pp. 79-93.
288. R. Y. Smith, D. R. Greenwood, J. F. Basinger, *Palaeogeography, Palaeoclimatology, Palaeoecology* **293**, 120 (2010).
289. M. Steinthorsdottir, A. S. Porter, A. Holohan, L. Kunzmann, M. Collinson, J. C. McElwain, *Clim. Past* **12**, 439 (2016).
290. M. Steinthorsdottir, V. Vajda, M. Pole, *Palaeogeography, Palaeoclimatology, Palaeoecology* **464**, 143 (12/15/, 2016).
291. M. Steinthorsdottir, V. Vajda, M. Pole, *Palaeogeography, Palaeoclimatology, Palaeoecology* **515**, 152 (2019/02/01/, 2019).
292. M. Steinthorsdottir, V. Vajda, M. Pole, G. Holdgate, *Geology* **47**, 914 (2019).

293. M. Steinthorsdottir, P. E. Jardine, W. C. Rember, *Paleoceanography and Paleoclimatology* **36**, e2020PA003900 (2021/01/01, 2021).
294. J. van der Burgh, H. Visscher, D. L. Dilcher, W. M. Kürschner, *Science* **260**, 1788 (1993).
295. Y. Wang, A. Momohara, L. Wang, J. Lebreton-Anberrée, Z. Zhou, *PLoS ONE* **10**, (2015).
296. Y. Wang, L. Wang, A. Momohara, Q. Leng, Y.-J. Huang, *Palaeoworld* **29**, 744 (2020/12/01/, 2020).
297. X. Y. Liu, Q. Gao, M. Han, J. H. Jin, *Clim. Past* **12**, 241 (2016).
298. J. C. McElwain, *Philosophical Transactions of the Royal Society London B* **353**, 83 (1998).
299. B.-N. Sun, S.-T. Ding, J.-Y. Wu, C. Dong, S. Xie, Z.-C. Lin, *Turkish Journal of Earth Sciences* **21**, 237 (2012).
300. D. L. Royer, *Review of Palaeobotany and Palynology* **114**, 1 (2001).
301. D. J. Beerling, in *A History of Atmospheric CO2 and Its Effects on Plants, Animals, and Ecosystems,* J. R. Ehleringer, T. E. Cerling, M. D. Dearing, Eds. (Springer, New York, 2005), pp. 114-132.
302. F. Wagner, L. L. R. Kouwenberg, T. B. van Hoof, H. Visscher, *Quaternary Science Reviews* **23**, 1947 (2004).
303. M. Rundgren, S. Björck, *Earth and Planetary Science Letters* **213**, 191 (2003).
304. W. M. Kürschner, J. van der Burgh, H. Visscher, D. L. Dilcher, *Marine Micropaleontology* **27**, 299 (1996).
305. D. L. Royer, K. M. Moynihan, M. L. McKee, L. Londoño, P. J. Franks, *Clim. Past* **15**, 795 (2019).
306. W. G. Chaloner, J. McElwain, *Review of Palaeobotany and Palynology* **95**, 73 (1997/01/01/, 1997).
307. D. J. Beerling, D. L. Royer, *Annual Review of Earth and Planetary Sciences* **30**, 527 (2002).
308. M. Slodownik, V. Vajda, M. Steinthorsdottir, *Palaeogeography, Palaeoclimatology, Palaeoecology* **564**, 110157 (2021/02/15/, 2021).
309. I. P. Montanez, J. C. McElwain, C. J. Poulsen, J. D. White, W. A. DiMichele, J. P. Wilson *et al.*, *Nature Geosci* **9**, 824 (11//print, 2016).
310. M. Huber, R. Caballero, *Climate of the Past* **7**, 603 (2011).
311. C. Elliott-Kingston, M. Haworth, J. M. Yearsley, S. P. Batke, T. Lawson, J. C. McElwain, *Frontiers in Plant Science* **7**, (2016).
312. P. J. Franks, D. L. Royer, D. J. Beerling, P. K. Van de Water, D. J. Cantrill, M. M. Barbour *et al.*, *Geophysical Research Letters* **41**, 4685 (2014).
313. W. Konrad, A. Roth-Nebelsick, M. Grein, *Journal of Theoretical Biology* **253**, 638 (2008/08/21/, 2008).
314. B. J. Tipple, S. R. Meyers, M. Pagani, *Paleoceanography* **25**, PA3202 (2010).
315. P. J. Franks, M. A. Adams, J. S. Amthor, M. M. Barbour, J. A. Berry, D. S. Ellsworth *et al.*, *New Phytologist* **197**, 1077 (2013/03/01, 2013).
316. W. Konrad, G. Katul, A. Roth-Nebelsick, M. Grein, *Advances in Water Resources* **104**, 145 (2017).
317. J. N. Milligan, D. L. Royer, P. J. Franks, G. R. Upchurch, M. L. McKee, *Geophysical Research Letters* **46**, 3462 (2019/03/28, 2019).
318. J. N. Milligan, A. G. Flynn, J. B. Kowalczyk, R. S. Barclay, J. Geng, D. L. Royer *et al.*, *Paleoceanography and Paleoclimatology* **37**, e2021PA004408 (2022/04/01, 2022).

319. T. Reichgelt, W. J. D'Andrea, B. Fox, *Earth and Planetary Science Letters* **455**, 115 (2016).
320. T. Reichgelt, W. J. D'Andrea, A. C. Valdivia-McCarthy, B. R. S. Fox, J. M. Bannister, J. G. Conran *et al.*, *Clim. Past* **16**, 1509 (2020).
321. T. Tesfamichael, B. Jacobs, N. Tabor, L. Michel, E. Currano, M. Feseha *et al.*, *Geology* **45**, 999 (2017).
322. B. Erdei, T. Utescher, L. Hably, J. Tamás, A. Roth-Nebelsick, M. Grein, *Turkish Journal of Earth Sciences* **21**, 153 (2012).
323. M. Grein, W. Konrad, V. Wilde, T. Utescher, A. Roth-Nebelsick, *Palaeogeography, Palaeoclimatology, Palaeoecology* **309**, 383 (2011/09/01/, 2011).
324. K. Moraweck, M. Grein, W. Konrad, J. Kovar-Eder, J. Kvacek, C. Neinhuis *et al.*, *Palaeontographica B* **298**, 93 (2019).
325. A. Roth-Nebelsick, C. Oehm, M. Grein, T. Utescher, L. Kunzmann, J.-P. Friedrich *et al.*, *Review of Palaeobotany and Palynology* **206,**, 1 (2014).
326. B.-N. Sun, Q.-J. Wang, W. Konrad, F.-J. Ma, J.-L. Dong, Z.-X. Wang, *Palaeogeography, Palaeoclimatology, Palaeoecology* **467**, 5 (2017/02/01/, 2017).
327. A. P. Wolfe, A. V. Reyes, D. L. Royer, D. R. Greenwood, G. Doria, M. H. Gagen *et al.*, *Geology* **45**, 619 (July 1, 2017, 2017).
328. L. Londoño, D. L. Royer, C. Jaramillo, J. Escobar, D. A. Foster, A. L. Cárdenas-Rozo *et al.*, *American Journal of Botany* **105**, 1929 (2018/11/01, 2018).
329. J. C. McElwain, I. Montañez, J. D. White, J. P. Wilson, C. Yiotis, *Palaeogeography, Palaeoclimatology, Palaeoecology* **441**, 653 (2016/01/01/, 2016).
330. M. Murray, W. K. Soh, C. Yiotis, R. A. Spicer, T. Lawson, J. C. McElwain, *International Journal of Plant Sciences* **181**, 142 (2020).
331. T. Reichgelt, W. J. D'Andrea, *New Phytologist* **223**, 1844 (2019/09/01, 2019).
332. B. J. Fletcher, S. J. Brentnall, W. P. Quick, D. J. Beerling, *Geochimica et Cosmochimica Acta* **70**, 5676 (2006).
333. B. J. Fletcher, S. J. Brentnall, C. W. Anderson, R. A. Berner, D. J. Beerling, *Nat. Geosci.* **1**, 43 (2008).
334. P. K. van de Water, S. W. Leavitt, J. L. Betancourt, *Science* **264**, 239 (1994).
335. X. Feng, S. Epstein, *Geochimica et Cosmochimica Acta* **59**, 2599 (1995/06/01/, 1995).
336. R. F. Keeling, H. D. Graven, L. R. Welp, L. Resplandy, J. Bi, S. C. Piper *et al.*, *Proceedings of the National Academy of Sciences* **114**, 10361 (2017).
337. B. A. Schubert, A. H. Jahren, *Earth-Sci. Rev.* **177**, 637 (2018/02/01/, 2018).
338. A. Wingler, P. J. Lea, W. P. Quick, R. C. Leegood, *Philosophical Transactions of the Royal Society of London Series B: Biological Sciences* **355**, 1517 (2000).
339. S. Rachmilevitch, A. B. Cousins, A. J. Bloom, *Proceedings of the National Academy of Sciences* **101**, 11506 (2004).
340. J. Jiao, B. Grodzinski, *Plant Physiology* **111**, 169 (1996).
341. B. A. Schubert, A. H. Jahren, *Geology* **43**, 435 (2015).
342. A. F. Diefendorf, K. H. Freeman, S. L. Wing, E. D. Currano, K. E. Mueller, *Earth and Planetary Science Letters* **429**, 33 (2015/11/01/, 2015).
343. V. J. Hare, E. Loftus, A. Jeffrey, C. B. Ramsey, *Nature Communications* **9**, 252 (2018/01/17, 2018).

344. K. Schlanser, A. F. Diefendorf, D. R. Greenwood, K. E. Mueller, C. K. West, A. J. Lowe *et al.*, *Geochimica et Cosmochimica Acta* **270**, 264 (2020/02/01/, 2020).
345. M. J. Kohn, *Geochemical Perspectives Letters* **2**, 35 (2016).
346. Y. Cui, B. A. Schubert, A. H. Jahren, *Geology* **48**, 888 (2020).
347. V. J. Hare, A. Lavergne, *Geochimica et Cosmochimica Acta* **300**, 215 (2021/05/01/, 2021).
348. Y. Cui, B. A. Schubert, *Glob. Planet. Change* **170**, 120 (2018/11/01/, 2018).
349. P. L. Koch, J. C. Zachos, P. D. Gingerich, *Nature* **358**, 319 (1992).
350. A. Sinha, L. D. Stott, *Glob. Planet. Change* **9**, 297 (1994).
351. Y. Cui, B. A. Schubert, *Earth and Planetary Science Letters* **478**, 225 (2017/11/15/, 2017).
352. B. H. Lomax, J. A. Lake, M. J. Leng, P. E. Jardine, *Geochimica et Cosmochimica Acta* **247**, 162 (2019/02/15/, 2019).
353. A. S. Porter, C. Yiotis, I. P. Montañez, J. C. McElwain, *Geochimica et Cosmochimica Acta* **213**, 517 (2017/09/15/, 2017).
354. M. A. Scher, R. S. Barclay, A. A. Baczynski, B. A. Smith, J. Sappington, L. A. Bennett *et al.*, *Geochimica et Cosmochimica Acta* **337**, 82 (2022/11/15/, 2022).
355. A. F. Diefendorf, K. E. Mueller, S. L. Wing, P. L. Koch, K. H. Freeman, *Proceedings of the National Academy of Sciences* **107**, 5738 (2010).
356. V. Galy, L. François, C. France-Lanord, P. Faure, H. Kudrass, F. Palhol *et al.*, *Quaternary Science Reviews* **27**, 1396 (2008/07/01/, 2008).
357. D. A. Stolper, M. L. Bender, G. B. Dreyfus, Y. Yan, J. A. Higgins, *Science* **353**, 1427 (2016).
358. D. C. Wade, N. L. Abraham, A. Farnsworth, P. J. Valdes, F. Bragg, A. T. Archibald, *Clim. Past* **15**, 1463 (2019).
359. D. C. Frank, B. Poulter, M. Saurer, J. Esper, C. Huntingford, G. Helle *et al.*, *Nature Climate Change* **5**, 579 (2015/06/01, 2015).
360. D. O. Breecker, *Earth and Planetary Science Letters* **458**, 58 (1/15/, 2017).
361. R. A. Stein, N. D. Sheldon, S. Y. Smith, *New Phytologist* **229**, 2576 (2021).
362. G. Mora, A. M. Carmo, W. Elliott, *Geology* **49**, 703 (2021).
363. H.-Y. Zhang, H. Hartmann, G. Gleixner, M. Thoma, V. F. Schwab, *Geochimica et Cosmochimica Acta* **245**, 1 (2019).
364. C. J. Hollis, T. Dunkley Jones, E. Anagnostou, P. K. Bijl, M. J. Cramwinckel, Y. Cui *et al.*, *Geosci. Model Dev.* **12**, 3149 (2019).
365. Y. Cui, B. A. Schubert, *Geochimica et Cosmochimica Acta* **172**, 127 (2016).
366. M. J. Kohn, *Proceedings of the National Academy of Sciences* **107**, 19691 (2010).
367. R. J. Brienen, G. Helle, T. L. Pons, J.-L. Guyot, M. Gloor, *Proceedings of the National Academy of Sciences* **109**, 16957 (2012).
368. J. Franke, D. Frank, C. C. Raible, J. Esper, S. Brönnimann, *Nature Climate Change* **3**, 3690364 (2013).
369. J. Pechtl, A. Land, *PloS one* **14**, e0210438 (2019).
370. P. Wilf, S. L. Wing, D. R. Greenwood, C. L. Greenwood, *Geology* **26**, 203 (1998).
371. I. S. Castañeda, S. Schouten, *Quaternary Science Reviews* **30**, 2851 (2011).
372. G. E. Stinchcomb, L. C. Nordt, S. G. Driese, W. E. Lukens, F. C. Williamson, J. D. Tubbs, *American Journal of Science* **316**, 746 (2016).
373. S. A. Blumenthal, N. E. Levin, F. H. Brown, J. P. Brugal, K. L. Chritz, J. M. Harris *et al.*, *Proc Natl Acad Sci* **114**, 7331 (2017).

374. N. E. Levin, T. E. Cerling, B. H. Passey, J. M. Harris, J. R. Ehleringer, *Proceedings of the National Academy of Sciences* **103**, 11201 (2006).
375. B. H. Passey, N. E. Levin, *Reviews in Mineralogy and Geochemistry* **86**, (2020).
376. B. H. Passey, H. Ji, *Earth and Planetary Science Letters* **518**, 1 (2019).
377. T. E. Cerling, *Special Publications of the International Association of Sedimentologists* **27**, 43 (1999).
378. W. Jost, *Diffusion in Solids, Liquids, and Gases*. (Academic Press, New York, N.Y., 1960).
379. H. Craig, *Geochim. Cosmochim. Acta* **3**, 53 (1954).
380. N. C. Arens, A. H. Jahren, R. Amundson, *Paleobiology*, 137 (2000).
381. J. Balesdent, C. Girardin, A. Mariotti, *Ecology* **74**, 1713 (1993).
382. M. Brunn, S. Spielvogel, T. Sauer, Y. Oelmann, *Geoderma* **235**, 146 (2014).
383. C. D. Keeling, *Environment International* **2**, 229 (1979).
384. M. S. Torn, A. G. Lapenis, A. Timofeev, M. L. Fischer, B. V. Babikov, J. W. Harden, *Glob. Change Biol.* **8**, 941 (2002).
385. M. A. Poage, X. Feng, *Glob. Biogeochem. Cycle* **18**, (2004).
386. J. G. Wynn, *Palaeogeography, Palaeoclimatology, Palaeoecology,* **251**, 437 (2007).
387. D. O. Breecker, S. Bergel, M. Nadel, M. M. Tremblay, R. Osuna-Orozco, T. E. Larson *et al.*, *Biogeochemistry* **123**, 83 (2015).
388. B. H. Passey, N. E. Levin, T. E. Cerling, F. H. Brown, J. M. Eiler, *Proceedings of the National Academy of Sciences USA* **107**, 11245 (June 22, 2010, 2010).
389. J. Quade, J. Eiler, M. Daëron, H. Achyuthan, *Geochimica et Cosmochimica Acta* **105**, 92 (2013).
390. J. R. Kelson, K. W. Huntington, D. O. Breecker, L. K. Burgener, T. M. Gallagher, G. D. Hoke *et al.*, *Quaternary Science Reviews* **234**, 106259 (2020/04/15/, 2020).
391. E. O. Heitmann, S. Ji, J. Nie, D. O. Breecker, *Earth and Planetary Science Letters* **474**, 272 (2017).
392. L. Zhang, C. Wang, P. B. Wignall, T. Kluge, X. Wan, Q. Wang *et al.*, *Geology* **46**, 271 (2018).
393. C. Huang, G. J. Retallack, C. Wang, Q. Huang, *Palaeogeography, Palaeoclimatology, Palaeoecology* **385**, 95 (2013).
394. G. A. Brook, M. E. Folkoff, E. O. Box, *Earth Surface Processes and Landforms* **8**, 79 (1983).
395. A. Indermühle, T. F. Stocker, F. Joos, H. Fischer, H. J. Smith, M. Wahlen *et al.*, *Nature* **398**, 121 (Mar, 1999).
396. D. O. Breecker, Z. D. Sharp, L. D. McFadden, *Proceedings of the National Academy of Sciences USA* **107**, 576 (2010).
397. I. P. Montanez, *Geochimica et Cosmochimica Acta* **101**, 57 (2013).
398. J. M. Cotton, N. D. Sheldon, *Geological Soecity of America Bulletin* **124**, 1411 (2012).
399. D. O. Breecker, G. J. Retallack, *Paleogeogr. Paleoclimatol. Paleoecol.* **406**, 1 (2014).
400. B. A. Maher, R. Thompson, *Quat. Res.* **44**, 383 (1995).
401. T. E. Huth, T. E. Cerling, D. W. Marchetti, D. R. Bowling, A. L. Ellwein, B. H. Passey, *Journal of Geophysical Research: Biogeosciences* **124**, 616 (2019).
402. D. O. Breecker, *Geochemical News* **144**, (2010).
403. Y. Gao, D. E. Ibarra, J. K. Caves Rugenstein, J. Chen, T. Kukla, K. Methner *et al.*, *Earth-Sci. Rev.* **216**, 103572 (2021/05/01/, 2021).

404. T. E. Cerling, *Glob. Biogeochem. Cycle* **6**, 307 (1992).
405. J. Da, Y. G. Zhang, H. Wang, W. Balsam, J. Ji, *Earth and Planetary Science Letters* **426**, 69 (2015).
406. D. D. Ekart, T. E. Cerling, I. P. Montañez, N. J. Tabor, *American Journal of Science* **299**, 805 (1999).
407. L. Nordt, S. Atchley, S. Dworkin, *Geology* **30**, 703 (2002).
408. L. Nordt, S. Atchley, S. Dworkin, *GSA Today* **13(12)**, 4 (2003).
409. G. J. Retallack, *Palaeogeography, Palaeoclimatology, Palaeoecology* **281**, 57 (2009).
410. P. Srivastava, S. Patel, N. Singh, T. Jamir, N. Kumar, M. Aruche *et al.*, *Sedimentary Geology* **294**, 142 (2013/08/15/, 2013).
411. L. Nordt, J. Tubbs, S. Dworkin, *Earth-Sci. Rev.* **159**, 103 (2016).
412. M. J. Kohn, C. A. E. Strömberg, R. H. Madden, R. E. Dunn, S. Evans, A. Palacios *et al.*, *Palaeogeography, Palaeoclimatology, Palaeoecology* **435**, 24 (2015/10/01/, 2015).
413. N. D. Sheldon, G. J. Retallack, S. Tanaka, *The Journal of Geology* **110**, 687 (2002).
414. N. D. Sheldon, N. J. Tabor, *Earth-Sci. Rev.* **95**, 1 (2009/06/01/, 2009).
415. A. Licht, G. Dupont-Nivet, N. Meijer, J. Caves Rugenstein, A. Schauer, J. Fiebig *et al.*, *Palaeogeography, Palaeoclimatology, Palaeoecology* **560**, 110016 (2020/12/15/, 2020).
416. J. M. Cotton, N. D. Sheldon, M. T. Hren, T. M. Gallagher, *American Journal of Science* **315**, 337 (2015).
417. T. M. Gallagher, C. G. Cacciatore, D. O. Breecker, *Paleoceanography and Paleoclimatology* **34**, 2113 (2019).
418. T. M. Gallagher, L. Serach, N. Sekhon, H. Zhang, H. Wang, S. Ji *et al.*, *Paleoceanography and Paleoclimatology* **36**, e2021PA004344 (2021/12/01, 2021).
419. A. Barral, B. Gomez, S. Legendre, C. Lécuyer, *Palaeogeography, Palaeoclimatology, Palaeoecology* **471**, 40 (4/1/, 2017).
420. H. P. Eugster, *Journal of Geophysical Research (1896-1977)* **71**, 3369 (1966/07/15, 1966).
421. R. V. Demicco, T. K. Lowenstein, *GSA Bulletin* **132**, 1365 (2019).
422. E. Guillerm, V. Gardien, D. Ariztegui, F. Caupin, *Geostandards and Geoanalytical Research* **44**, 243 (2020/06/01, 2020).
423. C. M. Duarte, Y. T. Prairie, C. Montes, J. J. Cole, R. Striegl, J. Melack *et al.*, *Journal of Geophysical Research: Biogeosciences* **113**, (2008/12/01, 2008).
424. R. Golan, I. Gavrieli, J. Ganor, B. Lazar, *Earth and Planetary Science Letters* **434**, 289 (2016/01/15/, 2016).
425. L. E. Lisiecki, M. E. Raymo, *Paleoceanography* **20**, 10.1029/2004PA001071 (2005).
426. G. J. Bowen. (Zenodo, 2023), vol. v0.1.
427. R. A. Berner, A. C. Lasaga, R. M. Garrels, *American Journal of Science* **283**, 641 (1983).
428. J. K. Caves, A. B. Jost, K. V. Lau, K. Maher, *Earth and Planetary Science Letters* **450**, 152 (9/15/, 2016).
429. N. Komar, R. E. Zeebe, G. R. Dickens, *Paleoceanography* **28**, 650 (2013).
430. M. Plummer. (2003).
431. R-Core-Team. (R Foundation for Statistical Computing, Vienna, Austria, 2022).
432. Y.-S. Su, M. Yajima. (2021).
433. M. Plummer. (2021).
434. A. Gelman, D. B. Rubin, *Statistical Science* **7**, 457 (11/1, 1992).

435. T. M. Marchitto, W. B. Curry, J. Lynch-Stieglitz, S. P. Bryan, K. M. Cobb, D. C. Lund, *Geochimica et Cosmochimica Acta* **130**, 1 (2014).
436. J. Ahn, E. J. Brook, L. Mitchell, J. Rosen, J. R. McConnell, K. Taylor *et al.*, *Global Biogeochem. Cycles* **26**, GB2027 (2012).
437. M. E. Raymo, L. E. Lisiecki, K. H. Nisancioglu, *Science* **313**, 492 (July 28, 2006, 2006).
438. U. Riebesell, A. T. Revill, D. G. Holdsworth, J. K. Volkman, *Geochimica et Cosmochimica Acta* **64**, 4179 (2000/12/15/, 2000).
439. E. B. Wilkes, R. B. Y. Lee, H. L. O. McClelland, R. E. M. Rickaby, A. Pearson, *Organic Geochemistry* **119**, 1 (2018/05/01/, 2018).